Euglenoid Movement and Novel Mechanisms for Soft Robots

By

Krishna Manaswi Digumarti

Department of Aerospace Engineering
University of Bristol
Department of Engineering Design and Mathematics
University of the West of England

A dissertation submitted to the University of Bristol in accordance with the requirements for award of the degree of Doctor of Philosophy in the Faculty of Engineering.
March 2019.

Word count: Fifty Thousand Two Hundred and Fifteen

BBC Click showing off the robot (EuMoBot) from this thesis.
Episode: 50 Shapes of Goo. Date: 10.06.2017.
Estimated viewers: 380 million.

Abstract

Organisms in nature utilise giant changes in body shape to perform everyday functions such as locomotion, object manipulation and feeding. These changes are observed across diverse scales and enable organisms to overcome challenges in their environment. This thesis focuses on the *Euglena* family of micro-organisms that display a unique manner of locomotion called euglenoid movement in which the cell undergoes a large change in shape. Novel mechanisms for highly deformable soft robots, inspired by this interesting behaviour are presented.

To numerically describe the shapes observed in euglenoids and the key features that change during locomotion, a mathematical method based on elliptic Fourier transforms is presented. This is a boundary-based, model free approach to quantify dynamic shapes of soft-bodied organisms and robots. In addition, it allows the comparison of shapes between two entities by providing a measure of similarity.

Two approaches to replicating the shape changing behaviour of the euglenoids were explored and are presented in this thesis. In the first approach, a novel soft pneumatic actuator called the hyper-elastic bellows (HEB) actuator is presented, which achieves 450% axial expansion, 80% radial expansion and up to 300 times change in volume. This actuator is then used in the design of soft robots capable of swimming autonomously in a manner that is hydrodynamically similar to that of the euglenoids. A similarity in shape of 85% is demonstrated.

In the second approach, the microscopic mechanism of pellicular sliding seen in euglenoids was replicated at a macro scale. The surface of the cell is covered in strips of protein, the relative sliding of which enables the organism to drastically alter its shape. Mimicking this structure, the design, fabrication and characterisation of morphing surfaces is presented which consist of flexible polymeric strips. These are used in the construction of a soft robotic module with an actively deforming surface.

This thesis demonstrates that behaviours seen in microscopic organisms can be replicated at larger scales in a robotic system to achieve functional advantages.

Acknowledgement

I would like to thank Professor Jonathan Rossiter and Dr. Andrew Conn for their valuable guidance, support, encouragement and supervision. While one inspired me to dream, the other made sure that I kept my feet firmly on the ground. The many insightful discussions between us have been useful on both an academic and a personal level.

I extend my gratitude to all the technicians and support staff at the Bristol Robotics Lab who have helped in various ways. Thanks in particular to Gareth Griffiths, Andrew Stinchcombe and Julian Potter for making sure that my work proceeded smoothly. A special thanks to Gordon Darling for encouraging me to stay motivated every day.

A warm thanks to colleagues from the SoftLab and FARSCOPE for the wonderful and lively atmosphere. Extra thanks to all those whom I shared a project with. The very efficient staff of FARSCOPE will always be remembered. Thanks also to Professor Barry Trimmer for his suggestions related to the Mathematical tools presented in this work.

I would like to acknowledge the Engineering and Physical Sciences Research Council for their support with the FARSCOPE program.

Finally, I would like to thank my parents, grandparents and my brother for their continued encouragement and support.

Author's Declaration

I declare that the work in this dissertation was carried out in accordance with the requirements of the University's *Regulations and Code of Practice for Research Degree Programmes* and that it has not been submitted for any other academic award. Except where indicated by specific reference in the text, the work is the candidate's own work. Work done in collaboration with, or with the assistance of, others, is indicated as such. Any views expressed in the dissertation are those of the author.

SIGNED:  DATE: 11 / 7 / 2019

Contents

List of Figures **xiii**

List of Tables **xvii**

List of Symbols **xix**

List of Abbreviations **xxi**

1 Introduction **1**

1.1 Motivation 1

1.2 Research Questions 3

1.3 Contributions 3

1.4 Publications 4

1.5 Outline of the Thesis 5

2 Background **7**

2.1 Bio-inspired Robotics 7

2.2 Locomotion in Soft Robots 8

2.3 Euglenoids 9

2.3.1 Cell Structure 9

2.3.2 Euglenoid Movement 10

2.3.3 Mechanism of Euglenoid Movement 11

2.3.4 Hydrodynamics of Euglenoid Movement 13

2.3.5 Lessons Learnt 15

2.4 Soft Materials 15

2.5 Soft Meta-materials 16

2.6 Soft Actuators 19

2.7 Muscle-like Actuation for a Soft Robot 21

2.8 Discussion 22

3 Quantifying Shape Change in Soft Morphologies **23**

3.1 Elliptic Fourier Descriptors 24

3.2 Eigenshape Analysis 27

3.3 Case Studies . . . 28
3.3.1 Euglenoid Movement . . . 28
3.3.2 Crawling Motion of Caterpillars . . . 31
3.3.3 Soft Tentacle . . . 35
3.4 Extension to Three Dimensions . . . 39
3.5 Limitations . . . 40
3.6 Discussion . . . 41

4 Giant Shape Change for Highly Deformable Soft Robots 43
4.1 Bio-inspiration from Euglenoid Movement . . . 43
4.2 Biomimetic Soft Actuation . . . 44
4.3 Hyper-Elastic Bellows . . . 46
4.3.1 Principle of Operation . . . 46
4.3.2 Fabrication . . . 48
4.3.3 Finite Element Analysis . . . 50
4.4 Characterisation of HEBs . . . 52
4.4.1 Inflation Phase . . . 52
4.4.2 Deflation Phase . . . 53
4.4.3 Comparison with Other Classes of Actuators . . . 57
4.5 EuMoBot - Euglenoid Inspired Soft Robot . . . 58
4.5.1 Fabrication . . . 58
4.5.2 Autonomous Control . . . 59
4.5.3 Experimental Set-up . . . 60
4.5.4 Locomotion Experiments . . . 61
4.5.5 Analysis and Comparison of Shapes . . . 63
4.5.6 Multi-modal Locomotion . . . 71
4.6 Discussion . . . 71

5 Pellicular morphing for soft robots 73
5.1 Pellicle Structure in Euglenoids . . . 73
5.2 Kinematic Model of Pellicular Sliding . . . 74
5.3 Design Tool for Artificial Pellicles . . . 77
5.4 Review of Actuator Technologies . . . 78
5.5 Bio-inspired Polymer Strips . . . 79
5.6 Principle of Operation . . . 84
5.7 Characterisation - Measurement of Separating Force . . . 84
5.8 FEA of Peeling . . . 87
5.9 Shape Exploration . . . 88
5.10 Deformation of a Pellicular Sheet . . . 89
5.11 Discussion . . . 91

6 Conclusion and Future Work **95**

6.1 Conclusions 95

6.2 Future Work 98

Bibliography **100**

Appendix **117**

List of Figures

1.1 Euglenoid movement in *Eutreptiella spirogyra*. 2

2.1 Illustration and micrograph of the euglenoid cell. 10
2.2 Snapshots from euglenoid movement of *Eutreptiella spirogyra*. 10
2.3 A paper model illustrating the change in shape due to sliding of strips. . . . 12
2.4 Illustration of pellicular strips and the mechanism of shape change. 13
2.5 Microstructure of the euglenoid pellicle. 13
2.6 Approximate Youngs modulus of biological and engineering materials. . . . 16
2.7 Youngs modulus vs. strength for different materials 17
2.8 Configuration of TAC before and after elongation. 18
2.9 Relation between normalised change in diameter and normalised change in length for the four TAC designs. 19
2.10 Performance limits for various actuators. 21
2.11 Concept of a muscle-like actuator. 21

3.1 Process of computing elliptic Fourier descriptors. 25
3.2 Estimated shape and error in reconstruction as a function of harmonics. . . 26
3.3 Pictorial representation of eigenshape analysis. 27
3.4 Normalised eigenvalues of the first five eigenvectors - euglenoid shapes. . . . 29
3.5 Scores on principal components - euglenoid. 30
3.6 Effect of principal component scores on shape - euglenoid. 30
3.7 Segments of the body in *Manduca sexta*. 31
3.8 Effect of principal component scores on shape - *Manduca sexta* and *Sphacelodes sp.* 32
3.9 Analysis of segment shapes in *Manduca sexta*. 33
3.10 Principal component scores as a function of time - *Manduca sexta*. 34
3.11 Experimental set-up of the passive tentacle. 35
3.12 Estimated shapes of the tentacle when moving in water. 36
3.13 Estimated shapes of the tentacle when moving in air. 37
3.14 Shapes of the tentacle in component space. 38
3.15 Estimated shapes of the tentacle when moving in air for a non-periodic signal. 39

3.16 Estimated shapes of the active tentacle when captured from two perpendicular viewpoints. 39

4.1 Four states of actuation in the hyperelastic bellows. 47
4.2 Illustration of the mould used to fabricate the HEB actuator. 49
4.3 Comparison of fabrication methods. 49
4.4 Design and dimensions of the HEB actuator. 50
4.5 Finite element model of the HEB actuator beofre and after inflation. 51
4.6 Axial strain as a function of internal pressure in HEB, obtained from finite element analysis. 51
4.7 The experimental set-up to measure axial and radial change of the HEB actuator. 52
4.8 Mean change in length and diameter of the HEB chamber as a function of time - inflation. 53
4.9 Mean internal pressure of HEB (above atmospheric pressure) as a function of time - inflation. 54
4.10 Mean change in length and diameter as a function of internal pressure - inflation. 54
4.11 Mean contraction of HEB as a function of time - deflation. 55
4.12 Internal pressure of HEB (below atmospheric pressure) as a function of time - deflation. 55
4.13 Mean compression of HEB as a function of internal pressure - deflation . . . 56
4.14 Comparison of HEB with different classes of actuators. 57
4.15 Relation between diameter and length for HEB. 58
4.16 Steps in the fabrication of EuMoBot. 59
4.17 Schematic view of the control architecture of EuMoBot. 60
4.18 One cycle of locomotion in the smaller robot. 62
4.19 A sequence of three cycles of locomotion of EuMoBots 62
4.20 Displacement of the centroid of the smaller robot during three cycles of motion. 64
4.21 Displacement of the centroid of the larger robot during three cycles of motion. 65
4.22 Qualitative comparison of shapes between EuMoBot and euglenoid. 66
4.23 Normalised eigenvalues of the first five eigenvectors describing the shape. . 67
4.24 Principal component scores - smaller robot. 68
4.25 Effect of principal component scores on estimated shape - smaller robot. . . 68
4.26 Principal component scores - larger robot. 69
4.27 Effect of principal component scores on estimated shape - larger robot. . . . 69
4.28 Comparison of shapes between euglenoid and the smaller robot. 70
4.29 Comparison of shapes between euglenoid and the larger robot 70
4.30 Demonstration of multi-modular ability of EuMoBot. 71

5.1 Illustration showing the four main structural components of a pellicular strip. 73
5.2 Definition of variables in the kinematic model of the pellicle. 74
5.3 MATLAB based design tool using a kinematic model of the pellicle. 77
5.4 Shear between strips for various input shapes. 78
5.5 Comparison of natural and artificial pellicle strips. 80
5.6 Set-up used to manufacture pellicular strips. 81
5.7 Common defects in the manufacture of the pellicle strips. 81
5.8 Bending and twisting of a sheet of pellice strips. 82
5.9 A sheet of pellicle strips with a pre-induced twist. 83
5.10 Actuator placement on interlocked strips. 83
5.11 Three distinct behaviours observed in pellicle strips based on end constraints. 84
5.12 Set-up used to measure the force of separation in the pellicle strips. 85
5.13 The three types of peeling tests performed on a pair of interlocked strips. . 85
5.14 Force to separate interlocked strips when peeled from the end and middle. . 86
5.15 Force to separate interlocked strips in the T-peel test. 86
5.16 Equivalent (von-Mises) stress in the strips from a finite element analysis of separation. 88
5.17 Various instances during the separation of interlocked strips. 88
5.18 Location of extrema of curvature for different end constraints and different actuator lengths. 89
5.19 Sliding of strips during change in shape. 90
5.20 Active deformation in a cylindrical configuration of strips. 91
5.21 Posterior end of *Euglena mutablis* showing strip reduction. 93

A1 Illustration of simple shear. 118
B1 The four TAC desigs studied. 121
B2 Illustration of two different families tiling patterns. 121
B3 Set-up used to determine the relationship between force and elongation in length of TAC. 122
B4 Configuration of TAC before and after elongation. 123
B5 Relation between force and elongation for the four TAC designs. 124
B6 Relation between normalised change in diameter and normalised change in length for the four TAC designs. 126
B7 Comparison of TACs with various classes of structures. 127
B8 A version of the TAC with multiple auxetic patterns within the same structure. 128
C1 A prototype of the EA-DEA crawling robot. 130
C2 Actuation principle of the four sector disk DEA. 130
C3 Stages of fabrication of electro-adhesive pad. 131
C4 A sectional view of the robot showing its different parts. 132
C5 Stages of actuation of the robot. 132

C6 Schematic diagram of the controller of the crawling robot. 133
C7 Three steps in the motion of the crawling robot. 134
C8 Tracked motion of the robot moving in an L-shape. 135
C9 Speed of the robot at different actuation frequencies. 135
C10 Illustration of the actuation principle in terms of circular coordinates. . . . 136
C11 Blocking force of a single DEA at different stroke lengths. 137
C12 Shear force due to EA as a function of charging voltage on different surfaces.139

List of Tables

4.1 Variance in shape captured by principal components 66

B1 Equivalent Poisson's ratio for auxetic structures. 126

List of Symbols

a_i, b_i, c_i, d_i	Fourier coefficients
C	set of 2D points forming the contour of a shape
$\mathbf{C}$	Cauchy-Green deformation tensor
C_D	covariance matrix
γ	strain in pellicle strips
D	matrix of Fourier coefficients
E	matrix of eigenvectors of covariance matrix
e_f	error in approximation using Fourier descriptors
$\hat{\mathbf{e_1}}, \hat{\mathbf{e_2}}, \hat{\mathbf{e_3}}$	basis vectors
$\mathbf{F}$	deformation gradient tensor
$\mathbf{g}$	metric tensor
η	kinematic viscosity
I	identity matrix
K	number of points on the contour
l	step index along the contour of a shape
L	length of an entity
$\mathcal{L}$	length of the contour of a shape
λ	body coordinate
M	number of images
N	number of harmonics
N_e	number of eigenvectors
P	pressure of an entity
$\mathbf{p}$	pressure field in the fluid
p_i, q_i	coordinates of points on the approximated contour
r, z	generating curves of the euglenoid surface
R	radius of an entity
$\mathbb{R}^2$	2D real coordinate space
S	total surface area of the euglenoid
${}^i s_j$	score corresponding to j^{th} principal component from i^{th} image frame
$\mathbf{s}, \mathbf{m}$	local coordinate frame of pellicle strips
θ	generic symbol for angle unless otherwise specified

$\mathbf{u}$	fluid velocity field
X_N, Y_N	approximated coordinates up to N harmonics
x_i, y_i	coordinates of points on the original contour
$\mathbf{x}$	configuration of a deformable body
ψ	displacement in the azimuthal direction

List of Abbreviations

DEA	Dielectric Elastomer Actuator
EA	Electroadhesion
EAP	Electro-Active Polymer
EuMoBot	Eugenoid Movement Robot
HEB	Hyper-Elastic Bellows
IPMC	Ionic Polymer-Metal Composites
PIV	Particle Image Velocimetry
SMA	Shape Memory Alloy
TAC	Tiled Auxetic Cylinders
TPU	Thermoplastic Poly-Urethane

Chapter 1

Introduction

Evolutionary pressure has driven natural systems to exploit and adapt to previously inaccessible environments [1]. In doing so, they have employed diverse strategies which incorporate intricate structures, efficient actuators and varied materials. These mechanisms are found at all scales ranging from the microscopic to the macroscopic. Robotics has been taking inspiration from these to solve equally challenging engineering problems [2]. This thesis takes a similar approach in applying a biological construct to the design of soft robots, taking inspiration from microorganisms called *Euglenoids*. A major outcome is the demonstration of locomotion of a soft robot capable of giant changes in shape, which has potential applications in minimally invasive medical procedures, search and rescue, exploration of terrain and maintenance of pipelines. Towards this aim, the design of novel actuators and structural mechanisms is investigated, the results of which are presented in this thesis, and sit at the interface of biology and engineering.

1.1 Motivation

Over the course of billions of years, biological organisms have evolved complex, multifunctional mechanisms to adapt to and overcome challenges in their natural environments. The field of bio-inspired robotics seeks to take inspiration from these natural systems, discern biological design and adapt it to solutions for robotic applications. While it is debatable if the solutions found in nature are optimal [3], bio-inspiration and bio-mimicry give engineers a significant head start in tackling the complex problems that have already been solved by nature [4]. Robotics also offers the possibility to test alternative biological designs and explore non-biological forms and motions, thus exploring the space of morphologies that biology has not yet examined. Some examples of successful bio-inspired robotic systems include the Stickybot (a gecko inspired climbing robot) [5], the Robobee (an insect like flying robot) [6], the Shrewbot (a robot that emulates the whisking motion found in rodents) [7], the TacTip (a tactile sensor based on the human fingertip) [8] and the octopus inspired robotic tentacle [9]. In addition to providing solutions for the betterment of human life, these artificial systems enable researchers to study biological

processes in an isolated and controlled manner, thereby allowing the formulation of more incisive hypothesis about living systems.

Soft robotics has the great potential to capture, model and emulate the mechanisms seen in biological systems. Most organisms in nature make use of soft materials in their construction. However, conventional robotics has employed rigid materials which restricts their movement to well defined environments. Some of these robots such as the Big Dog [10], Starl*ETH* [11] and the MIT Cheetah [12] have been partially successful in natural environments but require huge actuators, are power hungry and are still limited in their capabilities. There is therefore a new trend to use soft materials in the construction of robots that exploit the concepts found in nature, while simultaneously improving our understanding of the same [13]. These robots are also safer to interact with and offer advantages when operating in close proximity to the body, both outside and inside of it. It has been suggested that soft robotics will lead the way in applications requiring the ability to change the shape and size of the robot, such as in the case of a search and rescue operation through collapsed rubble [14]. Animal-like locomotion is another field where soft robotics applications are suitable.

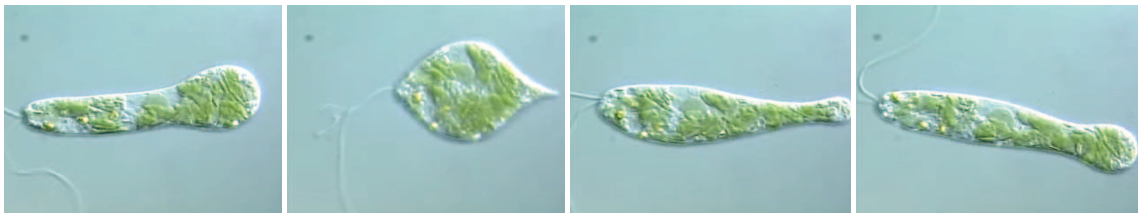

Figure 1.1: A sequence of frames showing the various shapes of the cell when performing euglenoid movement. The organism presented here is *Eutreptiella spirogyra*. Reproduced with permission from [15]

The problem of locomotion has been studied and replicated in robots to some degree [16]. However, one of the more challenging areas of research that soft robotics has the potential to address, which has been relatively less explored, is the locomotion and fluid flow at low Reynolds numbers [3]. This thesis seeks to fill this gap in knowledge through the investigation of the motion of a unique family of micro organisms called *Euglenoids*. These organisms display a characteristic type of locomotion, termed euglenoid movement, in which the cell undergoes a drastic change in shape and size [17] (fig. 1.1). It is theorised that this manner of locomotion is well suited to the constrained spaces that the organism typically finds itself in and is a strategy to overcome the viscous forces dominant in the low Reynolds number regime [18], [19]. Such an ability to locomote by changing the shape of the body is highly desirable in a robot navigating through crevices and this organism is therefore an ideal candidate to emulate.

1.2 Research Questions

The overall goal of this thesis is to investigate novel bio-inspired mechanisms of deformation in, and locomotion of, soft robots with a major focus on euglenoid movement. Several unique mechanisms exist in the euglenoid. The cell surface consists of a characteristic microscopic structure that is driven by a molecular mechanism which enables the deformation of the cell into drastic shapes. Understanding these structures and actuation mechanisms is one of many potential avenues for research. The one-of-a-kind locomotion strategy observed in these organisms is another interesting concept. The interplay between cell shapes and locomotion ability is yet another topic that can be exploited in robotics. Each of these is in itself a vast topic to study. This thesis takes a more focused approach in addressing the challenge of how euglenoid movement can be replicated in a robot by investigating the following set of research questions.

- How can large euglenoid-like changes in shape be achieved in a robot?
- Does shape change lead to euglenoid-like movement of the robot?
- Where, in the context of robotics, is euglenoid movement applicable?
- What functions other than locomotion can be based on the mechanism of euglenoid movement?

The work presented here may be described in terms of two approaches. In the first, the focus is on generating the large deformations seen in the euglenoid and as a result generate locomotion in the robot. This is done without trying to replicate the microscopic mechanism found in the organism. In the second approach, inspiration for design is taken from the microstructure of the cell surface to design a shape changing mechanism. As opposed to the other approach, focus in the second method is on achieving deformation at the local scale to bring about a change in shape at the global level. In other words, the first approach may be termed macroscopic while the second, microscopic.

1.3 Contributions

In addressing the above questions and investigating mechanisms for deformation and locomotion in a soft robot, this thesis makes the following contributions.

- A mathematical approach to quantify and compare dynamic features of shape in deforming soft bodies (chapter 3).
- The design and characterisation of a novel bellows-like pneumatic actuator that exhibits giant changes in shape (chapter 4).
- The presentation of euglenoid-like locomotion in a three-segment soft robot and a demonstration of its hydrodynamic similarity to the organisms (chapter 4).

- The design of polymer strips mimicking the strips of protein found in the cell walls of euglenoids and the presentation of the concept of actively morphing surfaces (chapter 5).

- The development of cylindrical auxetic structures with tunable mechanical behaviours as a method to design structures for soft robots (introduced as soft metamaterials in chapter 2 and continued in Appendix B).

- The conceptual design of a muscle like actuation system capable of localised and variable bidirectional strain (introduced in chapter 2 and demonstrated in the form of a multi-directional crawling robot in Appendix C).

1.4 Publications

The following peer-reviewed works have contributed to this thesis.

Journals

- **Digumarti KM**, Trimmer BA, Conn AT, Rossiter J. Quantifying Dynamic Shapes in Soft Morpohologies. *Soft Robotics*. Accepted: June 2019.

- **Digumarti KM**, Conn AT, Rossiter J. Pellicular Morphing Surfaces for Soft Robots. *IEEE Robotics and Automation Letters*. 2019 July;4(3):2304-9.

  Also presented this work at the IEEE International Conference on Robotics and Automation (ICRA 2019).

- **Digumarti KM**, Conn AT, Rossiter J. EuMoBot: Replicating Euglenoid Movement in a Soft Robot. *Journal of the Royal Society Interface*. 2018 Nov 21;15(148):20180301.

- **Digumarti KM**, Conn AT, Rossiter J. Euglenoid-Inspired Giant Shape Change for Highly Deformable Soft Robots. *IEEE Robotics and Automation Letters*. 2017 Oct;2(4):2302-7.

  Also presented this work at the IEEE International Conference on Intelligent Robots and Systems (IROS 2017).

Co-author at conferences

- Simons MF, **Digumarti KM**, Conn AT, Rossiter J. Tiled Auxetic Cylinders for Soft Robots. In 2019 *IEEE International Conference on Soft Robotics (RoboSoft)* 2019 Apr 14 (pp. 62-67). IEEE. *Simons MF and Digumarti KM contributed equally and are joint first authors.*

- **Digumarti KM**, Cao C, Guo J, Conn AT, Rossiter J. Multi-directional Crawling Robot with Soft Actuators and Electroadhesive Grippers. In 2018 *IEEE International Conference on Soft Robotics (RoboSoft)* 2018 Apr 24 (pp. 303-308). IEEE. *Digumarti KM and Cao C contributed equally and are joint first authors.*

1.5 Outline of the Thesis

The structure of the thesis is described below.

- Chapter 2 introduces soft robotics as a means to study animal locomotion and the *Euglena* family of micro-organisms. It presents a description of the cell, its key components, the characteristic euglenoid movement and the mechanism that enables this. It reviews current materials and actuator technologies used in the design of soft robots. Soft meta-materials in the form of auxetics are discussed. The concept of a muscle-like actuator is presented to motivate the need for new actuator technologies for soft robots.

- Chapter 3 presents a mathematical method to quantitatively describe the shape of soft robots. Based on the elliptic Fourier descriptors of shape, it describes a method to extract the prominent features of a shape that change with the deformation of a soft body. Implementation of the method is illustrated through case studies of soft bodied organisms and robotic prototypes, which include an analysis of cell shapes of the euglenoids.

- Based on the qualitative and quantitative observations of body shape in euglenoids, chapter 4 presents the design of a novel actuator (HEB: hyper-elastic bellows) capable of reproducing the shapes and large strains seen during euglenoid movement. Following a characterisation of its behaviour and a comparison with other classes of actuators, this actuator is used in the construction of a soft robot (EuMoBot). Experiments with robots of different scales, analysis of shapes and comparisons of locomotion with euglenoids are also presented.

- Chapter 5 focuses on replicating the micro-structure of the cell surface and the mechanism of actuation and deformation in euglenoids. The fabrication and characterisation of bio-inspired artificial pellicle strips is presented. A discussion on diverse shapes resulting from a variation in actuation and structural constraints is also included.

- Chapter 6 concludes the thesis by summarising the contributions made and presents thoughts on potential avenues for research in the future.

Chapter 2

Background

Many biological organisms make extensive use of soft materials in the construction of their bodies. This gives them capabilities to deal with complex challenges in their everyday life. Natural systems have evolved multi-functional bodies to efficiently perform many tasks essential to life such as locomotion, feeding, foraging, escaping from predators and manipulation of objects in the environment. Spurred by the recent advancements in technologies for manufacturing, actuation, sensing and processing data, the field of robotics is growing closer to reproducing these commonplace natural behaviours.

This thesis takes a bio-inspired approach to tackle the problem of locomotion in soft robots. In this chapter, a review of bio-inspired robotics is presented with emphasis on the locomotion of soft robots. This is followed by an introduction to the Euglena family of organisms and a discussion on the choice of materials and actuation technologies for soft robots.

2.1 Bio-inspired Robotics

Soft materials play a prominent role in the locomotion of animals. Their ability to dissipate and absorb forces is used by terrestrial animals that run or hop. Arboreal animals like monkeys use soft appendages to grip and support their bodies. Folding wings enable birds to manoeuvre at high speeds [20]. Soft bodies enable caterpillars to conform to the surface that they crawl on [21]. Deformable bodies are used to burrow and generate movement in granular media [22]. Cephalopods are able to squeeze into extremely small holes, manipulate objects and even open bottles and jars [23]. Smaller organisms like bacteria and algae are also able to contort their bodies to move and feed themselves. These are a few of the many examples of ways in which softness and compliance are exploited by organisms to achieve locomotion. It is believed that through the process of evolution, some animals have made their bodies soft and deformable, and as a result have gained the ability to exploit habitats that are unavailable to animals with stiff bodies [1].

The field of robotics has a lot to learn from biology. Traditional robots working in industrial settings are rigid. They are deliberately designed to be precise and accurate.

However, the natural world is filled with uncertainties and uncontrollable environments which these machines are incapable of dealing with. For robots to transition into the real world and co-habit with humans in a safe manner, these challenges will have to be overcome. One way to achieve this is to take inspiration from biology and make use of soft materials in their construction. This can be thought of as an equivalent evolution of the robots from a carefully controlled habitat into a more unpredictable one and the field of soft robotics has the potential to develop this next generation of robots.

2.2 Locomotion in Soft Robots

While the field of soft robotics has many applications ranging from haptics and medicine to human assistance and entertainment, the focus of this thesis is on locomotion and shape change. A comprehensive review of locomotion in soft robots is presented in [16]. A few examples are presented here to illustrate the breadth of research in this field. These studies allow the replication of biological phenomenon in controlled isolation and allow researchers to elicit the physics governing the expressed behaviour.

One of the first examples of the use of a soft robot to investigate animal locomotion is the imitation of the crawling motion of the caterpillar [24]. Since then, several other worm-like robots with different forms of actuation have been fabricated ([25, 26, 27, 28] to name a few). While the primary motivation was to study the movement of animals, some of these studies have resulted in applications in the medical field, in the form of robots for endoscopy [29]. This demonstrates the transferability of knowledge from one discipline into another, owing to similarity in operating conditions.

More recent studies have looked at legged locomotion using soft robots ([30, 31, 32]). These robots use multiple limbs to move the body, while keeping the centre of mass supported at all times. While dynamic walking has been achieved in relatively rigid robots through the use of elastic materials for construction and in series with actuation (eg. [11]), there are few examples of completely soft robots that demonstrate this capability. This could be attributed to the inability of soft materials to exert impulsive forces which is required for dynamic walking. Nevertheless, completely soft jumping robots have been developed [33].

Soft robots have also been used to study animal flight, both in the case of fixed wing fliers and in those with flapping wings. In the case of fixed wing flight, soft materials are used to vary the shape of the wing and study its effect on the forces experienced during flight. An example is the study inspired by the wings of a bat [34]. On the other hand, robotic platforms to study flight using flapping wings look at optimization of the forward and backward stroke by changing the stiffness and shape of the wing [35].

The final major type of locomotion replicated in soft robots is swimming. Prominent examples include the manta inspired robots [36, 37], the eel like robot that relies on undulatory movement of the body [38] and fish like robots [39, 40, 41, 42]. Several other

soft robots inspired by marine organisms are discussed in [16].

One particular form of locomotion that has received limited attention is that of locomotion in low Reynolds numbers. There are an estimated 1 million species of protists [43] and close to 10 million bacterial species on the earth [44], outnumbering the number of vertebrates by two orders of magnitude. The motion of most of these microorganisms falls under this regime. It has been pointed out that this is one area of locomotion which can be better understood through the use of soft robots [3]. However, few studies that investigate low Reynolds number robotics exist. In this thesis we take inspiration from one family of microorganisms called euglenoids whose fascinating manner of locomotion is discussed next.

2.3 Euglenoids

The term *Euglenoids* refers to a group of single-celled Eukaryotes that are commonly found in aquatic environments. These free-living micro-organisms were first observed by Antonie van Leeuwenhoek in 1674 (as cited by Dobell C. [45]) who described them as spirally-wound serpentine particles and called them 'little animalcules'. Later, in 1696, John Harris presented in his observations, 'oval creatures that would contract and dilate' [46]. Since then, thousands of euglenoid species have been identified [47]. One particular member, the species *Euglena gracilis* is considered a model organism and has been extensively studied [48], in part because euglenoids exhibit both plant-like (in the presence of light) and animal-like (when in the dark) characteristics [49]. The morphological diversity found in euglenoids offers an extraordinary opportunity to study major events in the evolution of eukaryotes [50]. Thus, they form one of many evolutionary bridges between bacteria and multi-cellular organisms.

2.3.1 Cell Structure

Euglenoids are soft bodied organisms. Depending on the species, cells from 10µm to 500µm in length and 10µm to 30µm in width have been observed [51]. A unique and unifying feature of these cells is the presence of a covering called the pellicle (see fig. 2.1b). This striking morphological feature may be described as a 'corset of proteinaceous strips' [52] with elaborate cross-sections that allows many species to dramatically alter their cell shape.

Most cells are equipped with one or more flegella (fig. 2.1a) which they use to swim. However, under certain environmental circumstances, a slower characteristic type of locomotion is observed in which the cell undergoes a drastic change in shape. This is called euglenoid movement (also referred to as metaboly and euglenoid motion) [50] and it is this second form of motion that is considered in this thesis. A third manner of movement called gliding is also observed in some species, where the cells glide over a moist surface which often is secreted mucous or a track of slime [53]. Some species such as the *Euglena*

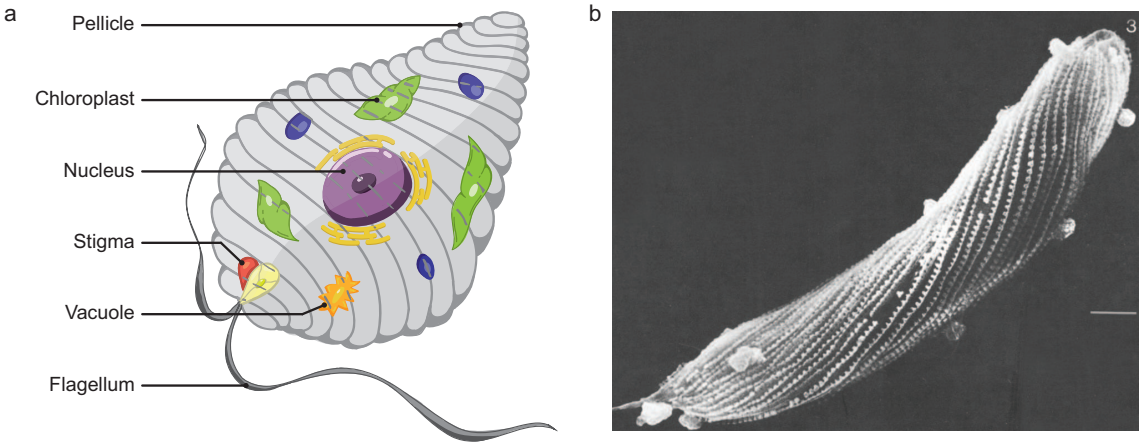

Figure 2.1: (a) An illustration of the euglenoid cell showing various organelles. (b) A scanning electron micrograph of the pellicle in *Euglena fusca*; magnification × 1,400; length bar = 10µm. Reproduced with permission from [17]

spirogyra, perform all these kinds of locomotion [54] while some like the *Euglena mutablis* [55], only exhibit euglenoid movement and others such as the *Euglena acus* only employ flagellar swimming [56].

2.3.2 Euglenoid Movement

Euglenoid movement is characterised by an extreme change in the shape of the cell. These changes range from an elongated rod-like form to a spherical ball like form, through a spindle-shaped form and a wide variety of other intermediate shapes [17]. Shown in fig. 1.1 and fig. 2.2 are shapes of the cell obtained from video recording made by *The Eulgneoid Project* [15] of the organism *Eutreptiella spirogyra* when performing euglenoid movement.

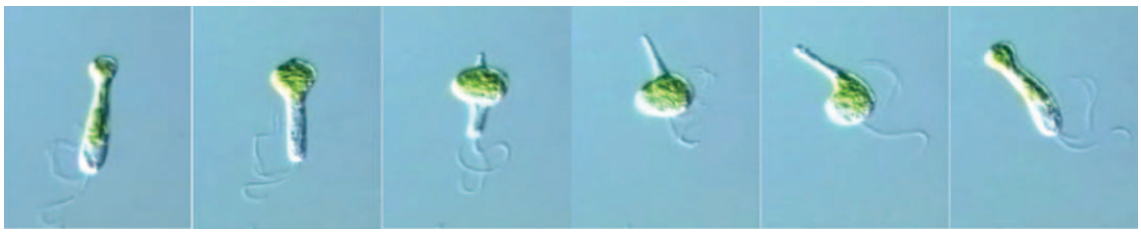

Figure 2.2: *Eutreptiella spirogyra* displaying euglenoid movement. Reproduced with permission from [15]

The reason for the existence of euglenoid movement and its evolution are not known. Euglenoids are believed to have evolved through secondary endosymbiosis of green algae [57] (when a free-living cell engulfs another free-living cell, it is called primary endosymbiosis. When the result of a primary endosymbiosis is engulfed by a cell, it is termed secondary endosymbiosis). Theories therefore suggest that the flexible pellicle evolved to engulf larger organisms and that euglenoid movement is a remnant of that evolutionary step.

It is known that deformations in the cell arise as a reaction to a strong stimulus such as light, heat, chemical shock or contact with an object [56]. The autotomy (casting off) of the flagellum in response to shock has been shown to induce contractions in the cell [58, 59, 60]. However, other forms of response have also been observed [61]. When euglenoids were placed in a fluid-filled microscopic maze that closely resembles their natural environment [18], a large portion of them demonstrated euglenoid movement. This suggests that their characteristic locomotion is well suited for movement through a constrained environment. A recent study showed that confinement does indeed induce euglenoid movement [19]. Such an ability would be particularly useful in a robot when traversing cluttered environments, squeezing through tight spaces and gaining entry into small apertures.

In addition to aiding locomotion, euglenoid movement is also used in other ways by euglenoids such as in transitioning to and from a cyst, scavenging tissues of other organisms by wiggling through their shells and generating movements in coordination with the beating of the flagellum to penetrate the eggs of small crustaceans [56]. These additional features to impinge and exert effective forces are also useful in robots, for example in a medical setting.

2.3.3 Mechanism of Euglenoid Movement

A study investigating the mechanism of euglenoid movement examined the *Euglena fusca* and showed that the change in shape is generated at the surface of the cell [17]. It has been determined to be purely a result of sliding between strips of protein within the pellicle. Remarkably, there is no stretching or contraction of the cell membrane. While it was previously believed that the strips only played a passive role and that the sliding occurred to accommodate the deformations [62], it is now agreed that active sliding occurs. Simulations of the cell surface displacement during euglenoid movement lend credit to this claim [63].

A simple illustration of shape change is shown in fig. 2.3 using a paper model. Consider a cylindrical sheet with strips painted on the surface, oriented along the axis (fig. 2.3a). The cylinder can be cut along one of the strips and laid out flat (fig. 2.3b). Now displace each strip by a small amount with respect to its neighbour. This arrangement is shown in fig. 2.3c. This collection can be rolled back into a cylinder by bringing together the two strips at the extremes (fig. 2.3d). The result of the sliding can be seen as an increase in diameter of the cylinder and a decrease in its length. The euglenoid changes its shape by employing a similar mechanism.

In euglenoids, the strips in the pellicle run either longitudinally or helically along the length of the pellicle (fig. 2.4a). The deformations in shape can be classified into two main types: symmetric and asymmetric (fig. 2.4b). Symmetric deformations occur when changes in shape are symmetric about the longitudinal axis. This results in rounding up of the body. Asymmetric deformations show asymmetric bending about the long axis.

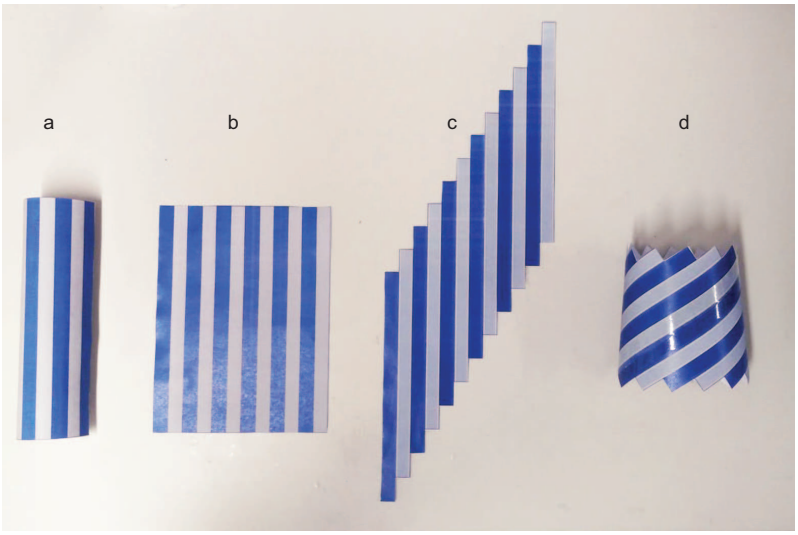

Figure 2.3: A paper model illustrating the change in shape in euglenoids due to sliding of strips. (a) A cylinder with longitudinal strips marked on it. (b) The cylinder rolled out flat. (c) Each strip is displaced by a small amount with respect to its neighbour. (d) The displaced strips are rolled back into a cylinder. The result is one with a larger diameter and shorter length compared to the initial design.

This results in bending and twisting movements which help in changing the direction of locomotion. Unlike in the model from fig. 2.3 where the amount of sliding was uniform and in the same direction at all points along the length of each strip, the euglenoid is able to control both the direction of sliding and its magnitude in localised regions. This enables it to display a diverse range of shapes, both symmetric and asymmetric.

The euglenoid pellicle as a whole consists of the proteinaceous strips, a collection of microtubules and the endoplasmic reticulum subtending the plasma membrane. Figure 2.5 shows an illustration of the ultrastructure (fine structure visible only at high magnifications) of the pellicle. The strips within the pellicle have an S-shaped cross section, predominantly consisting of a hook, a heel, an arch and an overhang [62]. The overhang of one strip interlocks with the heel of the adjacent strip and is held together by the hook. Comb-like projections found on either side of the heel interact with the corresponding projections on adjacent strips and contribute towards the sliding or in some instances, the inhibition of it [50]. A detailed study on diversity of pellicular structures and theories behind its evolution is presented in [64] and [65].

Investigations into the regulation of the cell shape in *Euglena gracilis* revealed that the microtubules play a prominent role in shape transitions [66]. It was found that changes in the patterns of microtubules cause the changes in shape of the cell. It is believed that the microtubules act as a stable cytoskeleton upon which a cytomuscular system (a muscular system at the cellular level) acts to bring about the change in shape. It is hypothesised that, and there is evidence in favour of, an actin-myocin contractile system operating in the euglenoids, leading to reorientation of the pellicle strips [67]. The exact operation of

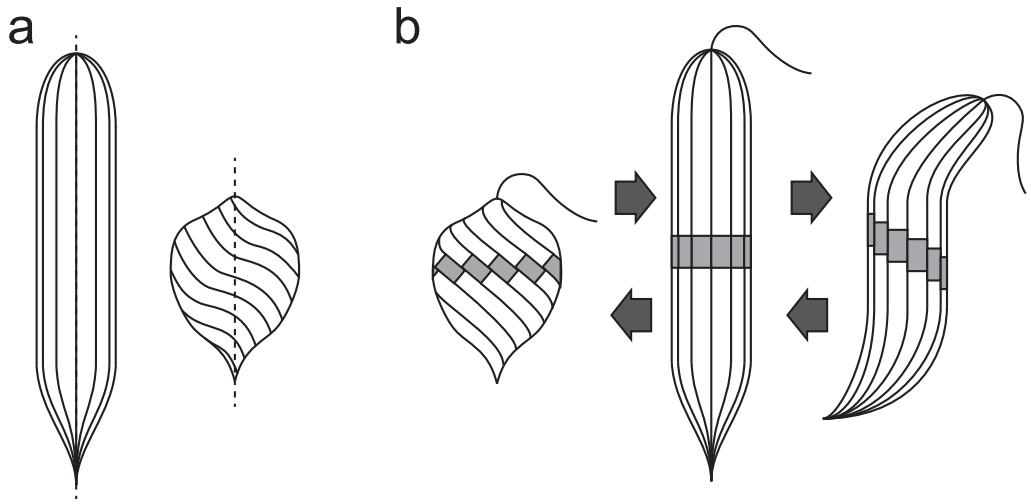

Figure 2.4: (a) Illustration of pellicular strips on the body of a euglenoid. The strips run either longitudinally or helically depending on the species and cell configuration. (b) Symmetric and asymmetric shape changes observed in euglenoids. Adapted from [17].

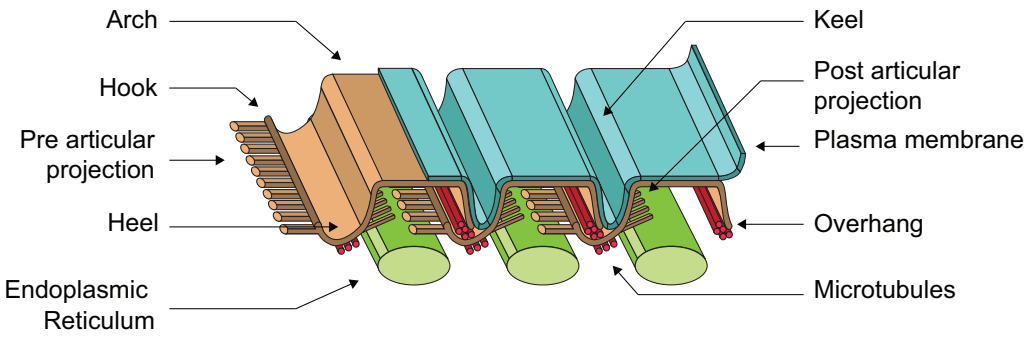

Figure 2.5: An illustration showing three pellicular strips and various microstructures of the cell. The hook, arch and teeth form the main structural elements of the pellicle. Adapted from [50]

these proteins in euglenoids is yet to be determined.

2.3.4 Hydrodynamics of Euglenoid Movement

As mentioned earlier, euglenoids live in the water. At the micrometer scale of the organisms, any kind of swimming movement (the term swimming is used henceforth in the general sense of any locomotion in a fluid environment and is not to be confused with the more specific flagellar swimming mentioned above) falls under the low Reynold's number regime. This non-dimensional number is defined to be the ratio of inertial forces to the viscous forces in the fluid. In the case of the euglenoids, it has been estimated to be in the range of 10^{-2} to 10^{-4} [68, 69]. The physics governing swimming at these small scales is dominated by viscous forces and inertia plays little role.

Traditional strategies found at larger scales such as in birds and insects where the

to and fro motion of the wings imparts a momentum to the fluid, are ineffective at the small scale, due to viscous damping. A consequence of dominant viscous forces is that the response of the fluid to the motion of the boundaries of a swimmer is instantaneous [70]. Micro-swimmers have therefore evolved novel propulsion strategies that exploit and overcome drag. One of these is to deform the surface of the body in a sequence of shapes, as is seen in the euglenoids.

The physics of motion in an incompressible Newtonian fluid at low Reynold's numbers in the absence of an external force can be described by the Stokes equations (simplification of the more general Navier-Stokes equations)

$$-\nabla \mathbf{p} + \eta \nabla^2 \mathbf{u} = 0 \quad , \quad \nabla \cdot \mathbf{u} = 0 \tag{2.1}$$

where $\mathbf{u}$ is the fluid velocity field around the swimmer and $\mathbf{p}$ is the pressure in the surrounding fluid and η is the kinematic viscosity. To obtain the force acting on the swimmer, one must solve for $\mathbf{u}$ and $\mathbf{p}$ with the appropriate boundary conditions. An important property of the Stokes equation is that it is linear, and independent of time. This has significant consequences for locomotion at small scales [71]. In the context of the current study, these may be stated as follows.

- *Rate independence*: when a swimmer is using surface deformations to swim, the distance travelled between two configurations of the surface does not depend on the rate at which the deformations occur but only on the sequence of shapes (the geometry) that the body passes through between these configurations.

- *Scallop theorem*: if the sequence of shapes used by the swimmer in a time-periodic manner is identical upon a time-reversal transform, then the swimmer cannot move on average.

An outline of the Mathematical proofs for the above two statements is presented in [70]. The scallop theorem, in particular, imposes geometric constraints on the shape transitions of micro-swimmers. A review of swimming strategies employed by microorganisms is presented in [70]. Several simple theoretical models for the design of artificial micro-swimmers have also been proposed such as Purcell's three link swimmer [71], the three sphere model [72] and the two sphere swimmer with shape change [73]. Many other models are discussed in [74, 75, 76]. All of these overcome the limitations imposed by the conditions mentioned above.

Most studies of the swimming in euglenoids focus on flagellar movement (eg. [77, 78]). The hydrodynamics of euglenoid movement in particular, have been studied in [69]. By using a kinematic model for the pellicle strip, the velocity of the cell surface for different shapes was estimated. This study identified the presence of a power and recovery phase during euglenoid movement. In the power phase, a bulge slides along the length of the body and the flow around it propels the swimmer forward (first four frames in fig. 2.2).

In the recovery phase, the bulge at the posterior disappears while a simultaneous bulge appears at the anterior. In this phase, there is a net backwards movement of the cell (last two frames in fig. 2.2). They estimate that the efficiency of swimming is in the order of 1% and comparable to that of organisms relying on cilia or flagella.

2.3.5 Lessons Learnt

This section provided a brief introduction to the fascinating organisms that Eugenoids are. It described the biological phenomenon of euglenoid movement and some of the theories surrounding its existence. Since this is thought to manifest in confined spaces, it provides an excellent opportunity for engineers to take inspiration from, when designing robots that operate in similar conditions. This strategy driven by large changes in the cell shape is the focus of chapter 4.

The mechanism of shape change due to sliding of strips in the surface of the cell was discussed. This is an interesting approach that has potential to be exploited for active morphing surfaces in soft robotics and beyond. This concept is explored in chapter 5.

Though the focus of this thesis is not on studying the hydrodynamics of euglenoid movement, a short review of relevant literature on the physics of swimming at the microscopic scale was presented. The intention is to impress upon the reader that the deformation of the surface of the body does indeed produce locomotion and that it is an efficient strategy employed by micro-swimmers. One of the aims of this thesis is to investigate if this strategy could be used at larger scales in a soft robot for locomotion.

As mentioned in the introductory chapter, the study of euglenoid movement has potential applications in several domains related to soft robotics. In this study it has inspired us to look at new soft actuators, deformable structures, robot designs and even mathematical tools to analyse our designs.

2.4 Soft Materials

In seeking to replicate the complex mechanisms observed in natural systems, the review in [79] proposes that the engineer have an insight into four key elements: a knowledge of the material properties, an awareness of stimuli that result in the unique behaviour, an understanding of the structural elements involved, and lastly, information concerning the cost in energy for actuation. While a comprehensive knowledge of all the above might be essential to make an exact replica of the observed system, it may not be necessary if the goal is to simply reproduce specific functionalities. A summary of the most commonly used materials and actuators in soft robots is presented here.

A comparison of the modulus of elasticity of various biological and engineering materials is shown in fig. 2.6. While traditional robotics has employed materials at the higher end of the scale, biological matter such as tissue, skin, muscle and tendons have moduli in the range of 10^6 to 10^9Pa. Engineering materials with similar moduli are elastomers,

polymers and foams. Materials from all three of these categories have been used in the construction of soft robots [1, 13, 16, 80].

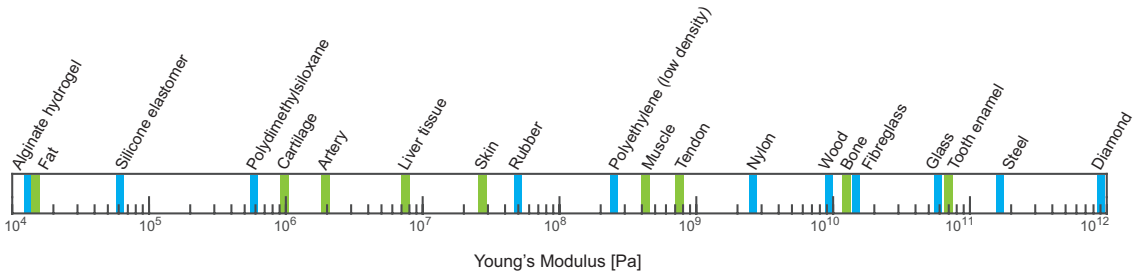

Figure 2.6: Approximate Youngs modulus of biological and engineering materials. Reproduced with permission from [80].

In this thesis we focus on two materials; silicone elastomers and thermoplastic polyurethane (TPU). Silicone elastomers often exhibit extremely large strains before rupture ($\approx$ 800-1000% elongation at break). They are therefore a good choice that can handle the large deformation required in the current study. Thermoplastic polyurethanes have a slightly larger modulus of elasticity (two orders of magnitude higher in our case, see chapter 5) and have a higher yield strength (tensile tear strength). In terms of functionality, they can thus hold a deformed configuration without yielding. A material selection chart showing a comparison of different natural and engineering materials with guidelines indicating preferential yielding or buckling is presented in fig. 2.7. This trade-off is re-visited in chapter 5 when the choice of material for the artificial pellicular strips is explained.

2.5 Soft Meta-materials

Compliant structures for soft robots have also been designed using meta-materials [82] with the goal of expanding the capacity for shape-change within existing material elastic limits. An advantage of meta-materials is that compliance can be achieved through the use of soft materials [83] or rigid materials [84] for structural strength, or a combination of both [85]. Softness is therefore not a property of the material alone but also of the geometry of construction. This offers greater freedom in the choice of materials when designing a soft robot.

Auxetic materials have become increasingly popular over the past few years due to their complex and tunable mechanical properties. These are a sub-class of meta-materials that are characterised by a negative Poisson's ratio, i.e. they increase in dimension along a direction perpendicular to that in which they are being stretched. This behaviour is exploited in the design of biomedical devices such as cardiovascular stents [86], deployable structures [87, 88], architecture [89] and energy absorbing foams [90]. This ability to change shape in two dimensions can also be exploited for locomotion.

In this section, we present our results from a preliminary study that characterised

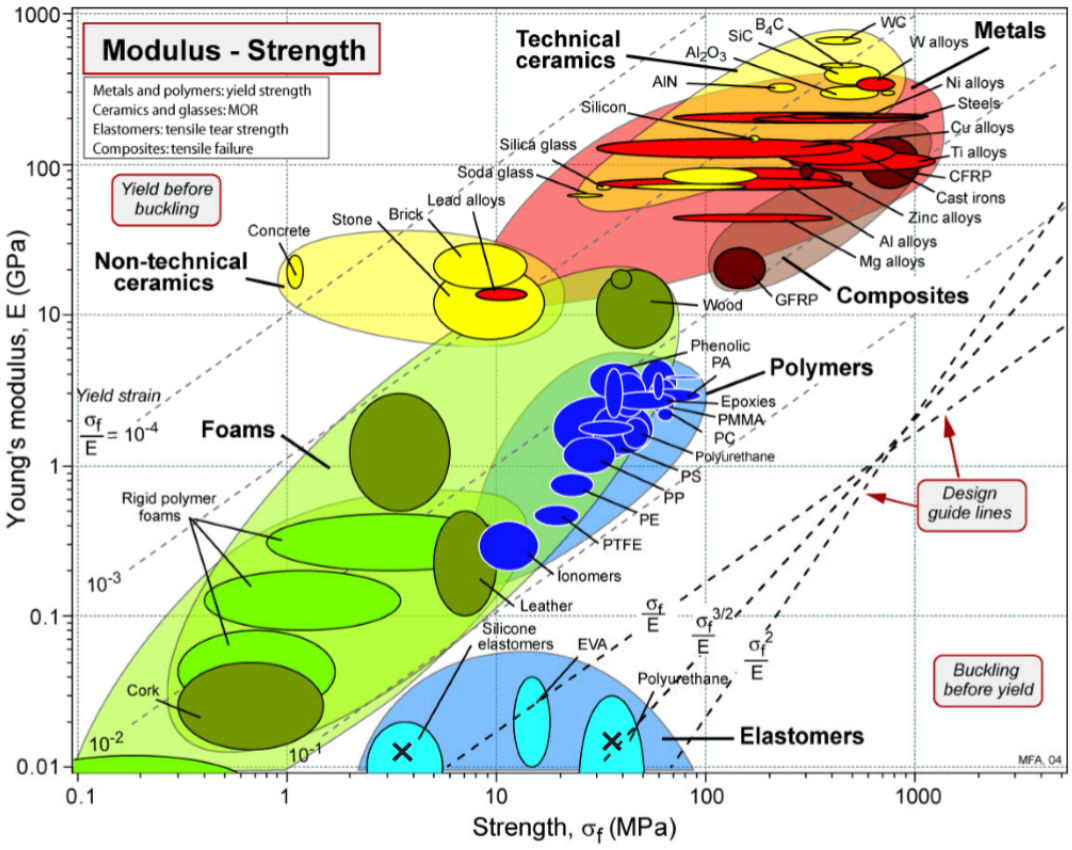

Figure 2.7: Material selection chart showing Youngs modulus vs. strength for different materials [81]. The materials used in this thesis (silicones and TPU) fall within the region of the elastomers, as indicated by 'x' marks.

auxetic structures of a cylindrical configuration termed tiled auxetic cylinders (TACs) [91]. Most studies in the literature have focused on two dimensional sheets and three dimensional lattices. A computational estimation of mechanical properties is presented in [92] and an experimental verification of properties in 2D hexagons is presented in [93]. In our work planar sheets were rolled-up into a cylindrical configuration. A purely theoretical model of cylindrical auxetic structures is presented in [94]. In other related work, a cylindrical auxetic has been 3D printed onto a tubular elastomer balloon [95], however our approach presents a simpler fabrication process. In addition, we characterised the mechanical response of the structure to elongation, which is absent in that work.

The design of the TACs is based on tiling of patterns placed next to each other. Four different re-entrant structures were considered. These are shown in fig. 2.8. These structures were characterised in terms of the relation between elongation and change in diameter. The corresponding mechanical response is shown in fig. 2.9. A key finding was that this response could be tuned by changing the pattern of tiles, the geometry of the pattern and also the orientation of the pattern. A more detailed discussion of the force-response, Poisson's ratio and the rationale behind choosing the four mentioned designs can be found in [91] and Appendix B. One possible manner in which this tunable response can be used in locomotion is by employing it in modulating friction. A combination of various auxetic designs within the same structure can be used to create a desired gradient in response. While TACs are a means of achieving a predetermined change in shape, the strong coupling between change in length and diameter is not ideal to replicate euglenoid movement, where part of the motion requires a change in length that is independent of a change in diameter (section 3.3.1).

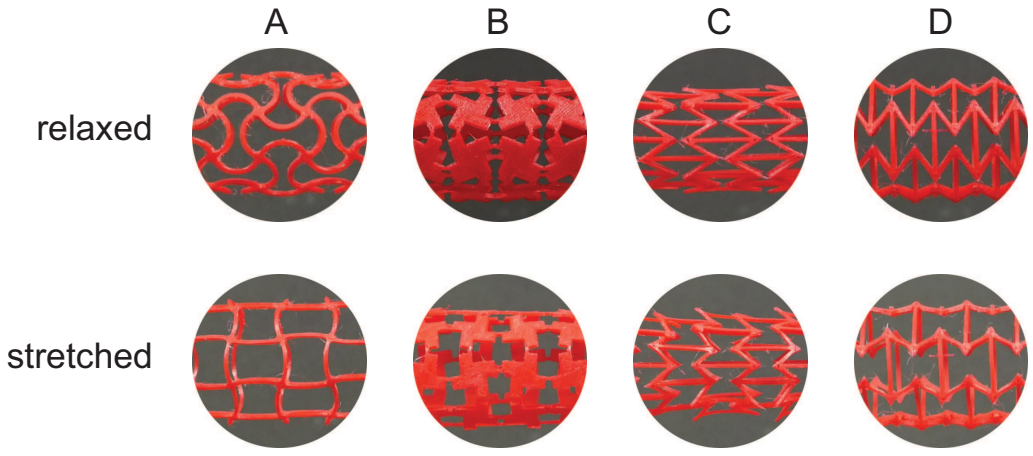

Figure 2.8: Configuration of the auxetic structure at rest (top) and after elongation (bottom) for the four designs considered: (A) re-entrant sinusoid, (B) modified re-entrant sinusoid, (C) re-entrant hexagon oriented along the axis and (D) re-entrant hexagon oriented perpendicular to the axis.

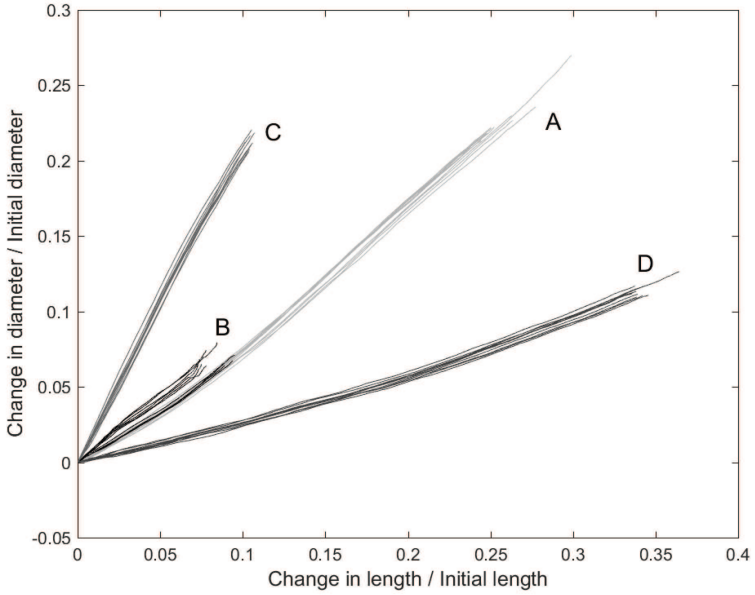

Figure 2.9: Relation between normalised change in diameter and normalised change in length for the four auxetic designs considered: (A) re-entrant sinusoid, (B) modified re-entrant sinusoid, (C) re-entrant hexagon oriented along the axis and (D) re-entrant hexagon oriented perpendicular to the axis. [91] © 2019 IEEE

2.6 Soft Actuators

In addition to choosing materials that behave similar to those found in biological systems, it is essential to choose actuators that work in synergy with these materials. Unlike the muscles found in animals, which can generate forces of large magnitude at high rates while being flexible, actuation for soft robots remains a challenge and is still a work in progress [1]. To offset the lack of a robust muscle-like actuator, engineers often design clever mechanisms to achieve predictable forces and movement in soft robots.

The most common actuation technologies used in soft robotics are electro-active polymers (EAP), shape memory alloy materials (SMA), pneumatics, hydraulics and cables driven by motors or solenoids [96]. A summary of their characteristics, advantages, disadvantages, modes of operation, actuation frequencies and representative mathematical models is presented in [97, 98, 99, 100, 101, 102].

Pneumatic and hydraulic actuators are frequently used in soft robot prototypes because they are lightweight, easy to implement, produce large strokes and deliver a lot of force [1]. In addition to pneumatic artificial muscles (or McKibben actuators) [103], other designs that incorporate carefully crafted chambers have been used to realise complex movements including bending and twisting [30, 104, 105]. Pleated bubble-like actuators with high strength and ability to exert forces several hundreds of times their mass have also been demonstrated [106]. A common drawback with these is the requirement for

external infrastructure and slow actuation rates in case of applications with high strains.

Electro-active polymers are increasingly being used in the design of soft robots. Dielectric elastomers in particular, are a preferred choice because they are closest in behaviour to natural muscle in terms of maximum strain and stress [98, 101] (fig. 2.10b). They also exhibit a high energy density, are easy to fabricate and can be manufactured at a low cost. By combining multiple actuators in various configurations, the force and stroke output can be amplified [97]. Some drawbacks include the need for high activation voltages and lack of reliability. Hydrogels and ionic polymer-metal composites (IPMCs) have also been used in soft robots. These however, are most suitable in applications requiring small forces (IPMCs) or slow actuation (hydrogels).

Actuators made of shape memory alloy (SMA) materials are the other major type used in soft robotic devices. Several of the prototype robots listed out in [16] make use of these actuators. A major advantage is their high energy density. Relatively low strains are produced but can be amplified when the actuators are used in a coiled configuration [107]. They have two major drawbacks. One is that a large amount of energy is lost in heating the actuator to cause the transition in phase required for actuation. Their efficiency is approximately 1% [1]. The other is that they have a slow actuation relaxation cycle. This is usually countered by employing a pair of actuators in an antagonistic configuration.

Coiled polymer actuators are another popular choice owing to their low cost, ease of manufacture and light weight [108]. They are flexible and can be used as individual actuators or in woven and braided configurations [109]. These actuators demonstrate up to 50% contraction strain and are capable of handling loads in excess of 100 times that of natural muscle of the same weight [108]. The contraction and expansion of the actuator is driven by a thermo-mechanical response of the material and can either be achieved directly through Joule heating of electrical conductors embedded within the structure or remotely by shining light on photo-active surface coatings. They have been characterised as having lower hysteresis compared to SMA actuators [110]. Other configurations that produce bending in multiple directions by exploiting anisotropic thermal expansion of the material have also been proposed [111].

The performance limits of the above mentioned actuators are charted in fig. 2.10. These limits are governed by both material properties and geometry of construction of the actuator. For example, in the case of McKibben air muscles, the elastic limits of the material of construction determine the maximum contraction of the actuator. An example of the influence of geometry on the performance of pneumatic actuators can be clearly seen in the case of PneuNets [113] where the configuration of internal chambers in the elastic structure determines the behaviour of the actuator upon inflation. Similarly, in the case of EAP, the dielectric constant of the material determines the amount of energy that can be stored. The same actuator used in different geometrical configurations results in varied stroke and force output [25, 114, 115, 116, 117]. Geometry also determines the extent of contraction in SMA actuators. Coiled configurations have been shown to produce larger

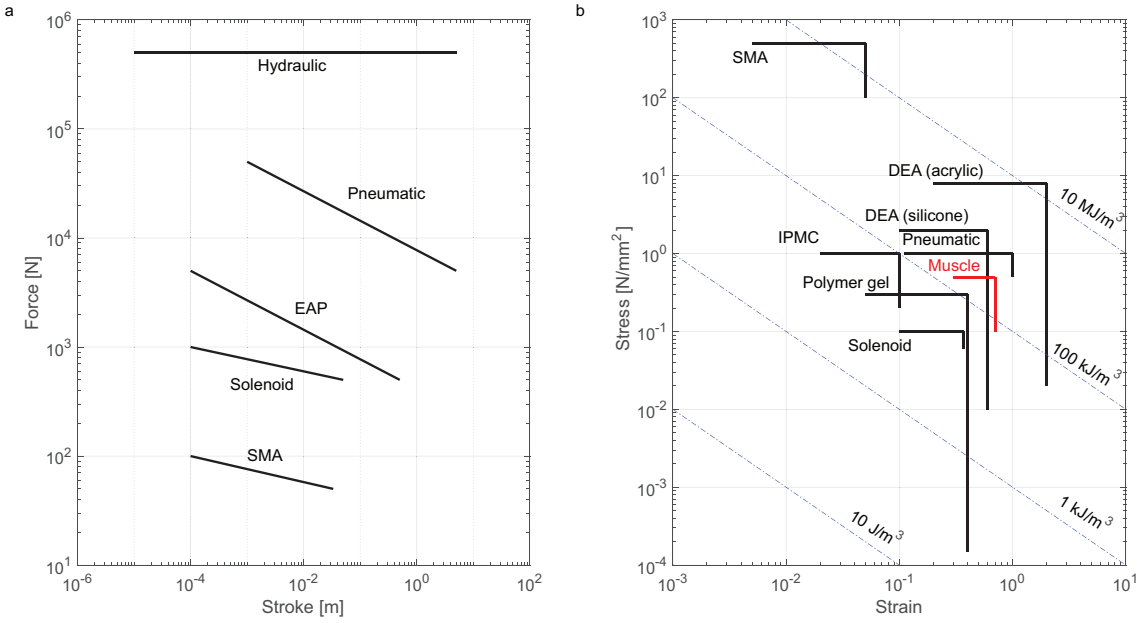

Figure 2.10: (a) Force vs stroke characteristics for commonly used soft robotics actuators. Adapted from [97]. (b) Maximum stress-strain performance limits for the same actuators. Limits for natural muscle are shown in red. Adapted from [102] and [112].

strains compared to uncoiled ones [107]. It is important to be aware of these limitations when choosing an appropriate actuation technology.

2.7 Muscle-like Actuation for a Soft Robot

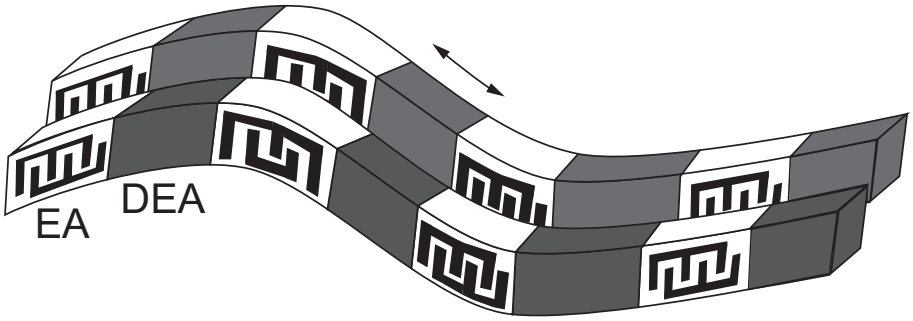

Figure 2.11: Illustration of a muscle-like actuator consisting of segments that can extend (DEA) and segments that can provide anchoring (EA).

As mentioned earlier, the change in the shape of the euglenoid cell is driven by sliding of strips on the surface. This sliding is bi-directional and the cell is able to control the amount of sliding taking place in a localised region. To achieve this in a robotic system, there is a need for a suitable muscle-like actuator-mechanism that is capable of producing relative motion between two surfaces. It must also be able to generate a variable magnitude of strain along its length. In the absence of an existing solution, a conceptual illustration

of such an actuator is shown in fig. 2.11 which combines existing technologies to achieve the desired motion between two adjacent strips.

In this illustration, each strip consists of multiple segments of dielectric elastomer actuators (DEA) alternating with electroadhesive (EA) sections. The core idea is that the DEA segments generate motion through elongation upon actuation, while the EA segments provide points of anchoring. The motion may therefore be described as 'two-anchor inching'. Since the actuators may be controlled independently, localised strain can be generated. In addition, strains can be generated in both directions along the strip. Moreover, the amount of strain generated in an intermediate region is limited only by the anchoring force of the EA and the length of the strip. The compliant nature of both the actuator technologies is expected to enable the mechanism to function even when the structure is bent or twisted.

A limitation to readily evaluating this concept is one of size. Fabricating DEA and EA actuators at small scales is challenging. Therefore, this problem was studied at the centimetre scale through the development of a multi-directional crawling robot [118] which works on the same principle of 'two-anchor' crawling mentioned above. The process of fabrication and experimental characterisation of this actuator is presented in Appendix C. This actuator was not used in the thesis because of the above mentioned limitation. It will be revisited in chapter 5 to present the context in which such a muscle-like actuator would be extremely useful.

2.8 Discussion

This chapter reviewed some of the prominent forms of locomotion in animals that have been studied using soft robotic platforms. It identified a gap in research related to locomotion at low Reynolds number flows, which this thesis will address through the study of euglenoid movement. The characteristic type of movement seen in the euglenoids was discussed along with a presentation of the mechanism at the cellular level that enables them to drastically alter their cell shapes.

A short summary of materials and actuators commonly used in the construction of soft robotic prototypes was presented with a discussion on their similarity to biological materials. In the next three chapters, these concepts and selection strategies shall be revisited when discussing the tools to analysis deformations of the cells, selection of materials for the design of the robots and the choice of actuators for each design.

The next chapter will lay the foundations for studying euglenoids through the development of methods to quantify shape change in soft organisms and soft robots.

Chapter 3

Quantifying Shape Change in Soft Morphologies

The work described in this chapter is based on work presented at the following peer-reviewed venues.

- **Digumarti KM**, Trimmer BA, Conn AT, Rossiter J. Quantifying Dynamic Shapes in Soft Morpohologies. *Soft Robotics*. Accepted: June 2019.
- **Digumarti KM**, Conn AT, Rossiter J. EuMoBot: Replicating Euglenoid Movement in a Soft Robot. *Journal of the Royal Society Interface*. 2018 Nov 21;15(148):20180301.

The previous chapter introduced euglenoid movement and showed that the cell bodies of euglenoids undergo large deformations, displaying a range of varied shapes. Since movement at the scale of the organism is generated by the changing shape of the body, understanding the progression of shapes helps understand the locomotion of the organism. This chapter presents a method to numerically describe these shapes. As will be demonstrated through case studies, the method is suitable to a multitude of organisms and robots with deforming bodies.

In the context of robotics, a quantitative method to describe the shape of a deformable body is extremely useful in the design and analysis of soft robots. Abstraction is a key step in bio-inspired design [119], and identifying the key features of a shape could influence design choices such as the material of construction or the actuation technology. The mechanical behaviour may be hyper-elastic or non-linear and therefore, unlike the case of rigid bodies, it is not trivial to describe the shape of a soft deformable body. A numerical representation of the shape facilitates the construction of a model of a compliant body. This model could then be used to optimize its locomotion [120], actively deform it through visual inspection [121], or in the case of morphological computation, be used to represent the intelligence inherent in the body [122].

Several approaches have been proposed to quantitatively describe shape. The difference between them is in the features they use to describe a form. Examples of these include measures of distances, details of texture, positions of key-points and descriptions of the boundary. The approaches may be classified into two broad types, landmark-based and boundary-based. Landmark-based approaches consider relative pose of an identified set of points while excluding higher order information such as that about the curvature between them. It has been argued in [123] that landmark based metrics are incomplete representations of the form and that much of the information of potential significance is not captured, particularly in the case of biological systems. The choice of landmarks is also subjective. On the other hand, methods that rely on the description of boundaries focus on the outline of the form. In this work, we consider one such method that uses elliptic Fourier descriptors [124].

The elliptic Fourier descriptor has been used to describe biological shapes such as those of nuclei [125], shells [126], leaflets [127] and roots [128]. In these studies, the descriptor was used to study static shapes. The novelty of the approach presented in this chapter is in applying the descriptor to dynamic shapes of soft-bodied organisms and robots. This is achieved by using the descriptors in combination with principal component analysis. This model-free method is appropriate to describe the shape of non-linear, dynamic, soft-bodied systems where the complexity of high dimensions restricts the use of model based approaches.

A mathematical introduction to the elliptic Fourier descriptors is presented first. This is followed by the details of its implementation in combination with eigenshape analysis. The giant changes in shape seen during euglenoid movement in *Eutreptiella sp.* are then analysed using this framework. The locomotion of other model organisms (*Manduca sexta* and *Sphacelodes sp.*) and movement of a soft tentacle [122] are also studied. In addition to facilitating the characterisation of shapes, the descriptor can also be used to compare the shapes between two entities, for example, a robot and an organism. A boundary based approach is advantageous in this case as there is no need to define equivalent landmarks between the systems, which may not be always possible.

3.1 Elliptic Fourier Descriptors

The elliptic Fourier descriptor of shape for closed contours [124] belongs to a class of descriptors that use a Fourier series to approximate the boundary of a shape. It is a procedure that fits a closed curve to a set of two dimensional points with arbitrary precision. The advantage of these descriptors over other boundary methods is that they preserve information of the contour such that it can be reconstructed in the absence of the original specimen [123]. Additionally, both global and localised aspects of the contour (i.e. the overall shape as well as particular regions of it) are amenable to analysis. The descriptor can also be made invariant to translation, rotation and scale. In this work, the descrip-

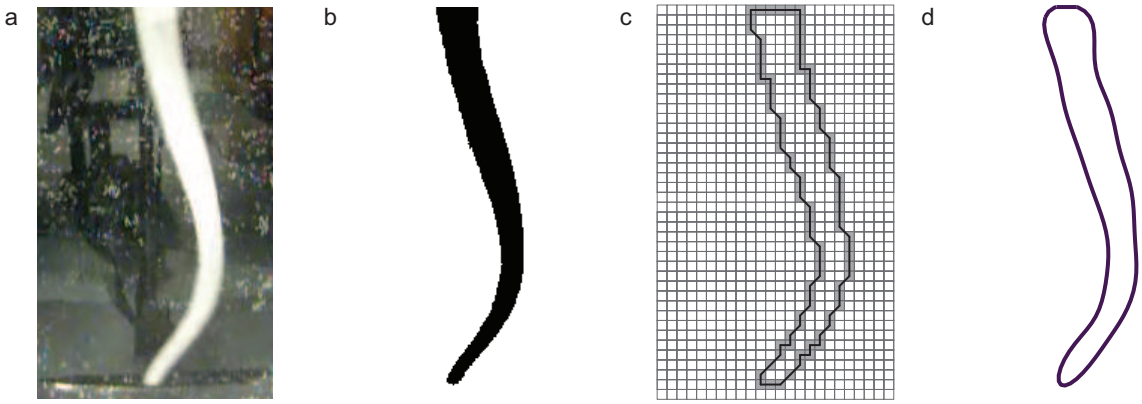

Figure 3.1: From the input image (a), the region of interest (b) is extracted. Next, the contour (c) is identified, which is a finite set of points in two-dimensional space. From this, the Fourier coefficients are determined. The shape can then be reconstructed (d) from the coefficients.

tor has been implemented in 2D. Line contours can be processed in 3D [129, 130] and extensions to the current method are discussed in section 3.4.

The first step in the process of computing the elliptic Fourier descriptors is to extract the contour of the specimen being studied. Given a two dimensional shape (fig. 3.1b), its contour ($C \subset \mathbb{R}^2$) is a discrete representation of the boundary and consists of a finite set of points (fig. 3.1c). A piecewise linear approximation of the contour that preserves information of the local orientation of the curve can be obtained by employing the Freeman chain encoding [131]. This encoding represents the contour as a chain of directed line segments. While not essential in computing the Fourier descriptors, this encoding helps in describing contours with self intersections, as shall be shown in section **??**. The projections of the chain segments on to the coordinate axes (eg. x and y axes) can be represented as an independent Fourier series [124]. The corresponding approximations up to N harmonics (X_N and Y_N) are given as

$$X_N(l) = a_0 + \sum_{n=1}^{N} \left(a_n \cos \frac{2n\pi l}{\mathcal{L}} + b_n \sin \frac{2n\pi l}{\mathcal{L}} \right), \tag{3.1}$$

$$Y_N(l) = c_0 + \sum_{n=1}^{N} \left(c_n \cos \frac{2n\pi l}{\mathcal{L}} + d_n \sin \frac{2n\pi l}{\mathcal{L}} \right) \tag{3.2}$$

Here, l is one step along the contour, i.e. traversal of one line segment that makes up the contour. This is periodic with period $\mathcal{L}$, the total length of the contour. a_0 and c_0 are the bias components of the Fourier series corresponding to a frequency of 0, and a_n, b_n, c_n and d_n are coefficients of the nth harmonic with the first two describing the projections on to the x axis and the last two describing those on to the y axis. These coefficients are

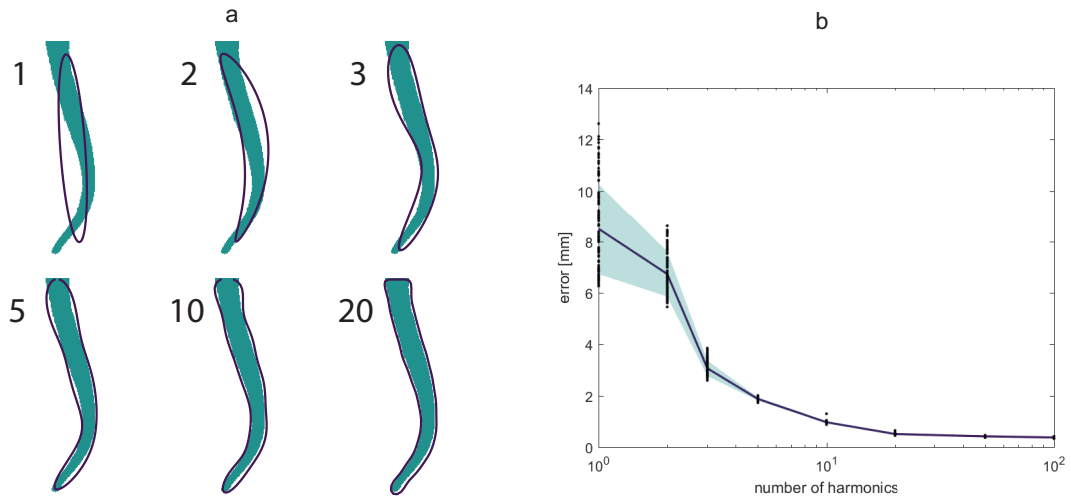

Figure 3.2: (a) Estimate of the shape of the tentacle as the number of harmonics increases from 1 to 20. (b) Mean error in the estimate of 98 distinct shapes of the tentacle during its movement. The shaded region indicates one standard deviation away from the mean.

given by the following expressions and constitute the description of the shape. Here, K is the number of points on the contour.

$$a_n = \frac{L}{2n^2\pi^2}\sum_{p=1}^{K}\frac{\Delta x_p}{\Delta l_p}\left[\cos\frac{2n\pi l_p}{\mathcal{L}} - \cos\frac{2n\pi l_{p-1}}{\mathcal{L}}\right] \tag{3.3}$$

$$b_n = \frac{L}{2n^2\pi^2}\sum_{p=1}^{K}\frac{\Delta x_p}{\Delta l_p}\left[\sin\frac{2n\pi l_p}{\mathcal{L}} - \sin\frac{2n\pi l_{p-1}}{\mathcal{L}}\right] \tag{3.4}$$

$$c_n = \frac{L}{2n^2\pi^2}\sum_{p=1}^{K}\frac{\Delta y_p}{\Delta l_p}\left[\cos\frac{2n\pi l_p}{\mathcal{L}} - \cos\frac{2n\pi l_{p-1}}{\mathcal{L}}\right] \tag{3.5}$$

$$d_n = \frac{L}{2n^2\pi^2}\sum_{p=1}^{K}\frac{\Delta y_p}{\Delta l_p}\left[\sin\frac{2n\pi l_p}{\mathcal{L}} - \sin\frac{2n\pi l_{p-1}}{\mathcal{L}}\right] \tag{3.6}$$

Once the set of Fourier coefficients has been computed, the curve can be reconstructed using the same equations as those for the approximation. The number of harmonics dictates the accuracy of the approximation. This is shown visually in fig. 3.2a where the shape of a soft tentacle was reconstructed. The case studies presented here use the same number of harmonics to approximate both the x and y projections of the contour. A different number for each may also be used. To quantify the closeness of fit, an error function (e_f) in terms of the mean distance between points on the original contour and the approximated contour can be used.

$$e_f = \frac{1}{K}\sum_{i=1}^{K}\sqrt{(x_i - p_i)^2 + (y_i - q_i)^2} \tag{3.7}$$

Here, x_i and y_i are points on the original contour and p_i and q_i are points on the approximated contour that are closest in Euclidean distance from x_i and y_i respectively.

The average e_f across 98 distinct shapes of the tentacle during its movement was computed for increasing number of harmonics (fig. 3.2b). As can be observed, the residual drops significantly with increasing harmonics up to a certain point. In this case, at 20 harmonics, the mean error across shapes is less than 0.5mm (for an object of length 400mm and mean diameter of 25mm) and can be considered to be a sufficiently detailed approximation.

3.2 Eigenshape Analysis

The goal of the study is to not only describe a single shape but to understand how the shape changes over time. To do this, multiple shapes are collected, for example, through video recording of motion. Descriptors from these shapes are then analysed using principal component analysis, followed by dimensionality reduction.

The representation of a shape in terms of elliptic Fourier descriptors produces four coefficients per harmonic which constitute its mathematical description. An approximation using N harmonics results in a set of $4N-3$ normalised coefficients. For a video containing a sequence of M frames with one shape in each frame, the complete description of all shapes is a matrix of coefficients $D \subset \mathbb{R}^{M\times(4N-3)}$. These coefficients have little physical meaning in their raw form. To extract key features that describe the shape in a physical sense, principal component analysis was used [132]. The aim is to describe independent trends in shape, for which the principal components are an ideal choice by virtue of being mutually orthogonal. In addition, we seek to reduce the dimensionality of data by describing it in terms of a smaller number of components.

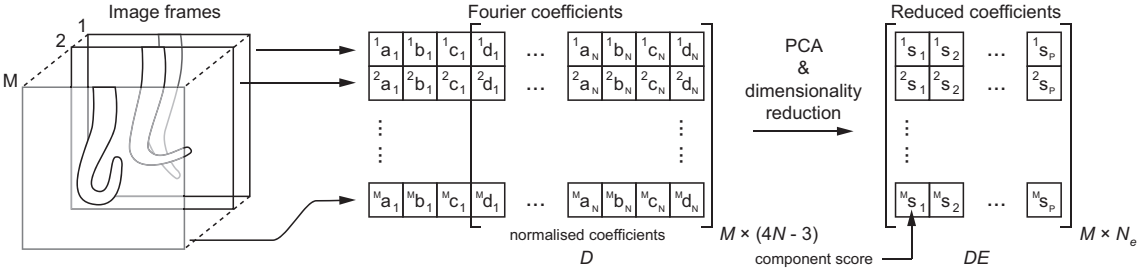

Figure 3.3: The matrix $D \subset \mathbb{R}^{M\times(4N-3)}$ consists of normalised Fourier coefficients (${}^{i}a_j$, superscript indicating the frame number and subscript indicating the harmonic that it corresponds to). Using principal component analysis followed by dimensionality reduction, a reduced matrix DE is obtained, where E is the matrix of N_e eigenvectors. Elements of DE, ${}^{i}s_j$ represent component scores with superscripts indicating the frame number and subscripts indicating the principal component that the coefficient corresponds to.

Each row of D represents one shape. First, the covariance matrix of D, $C_D \subset \mathbb{R}^{(4N-3)\times(4N-3)}$ is computed. Next, the eigenvectors of the covariance matrix are evaluated. By choosing an appropriate number of eigenvectors, the original data D can be represented as a reduced set of numbers without losing information and while gaining

physical meaning. Let $E \subset \mathbb{R}^{(4N-3)\times N_e}$ be the matrix whole columns contain the first N_e eigenvectors of the covariance matrix C_D. The rows in the product matrix $DE \subset \mathbb{R}^{M\times N_e}$ represent the coefficients (also referred to as component scores) in terms of the eigenvectors and convey a more meaningful description of the shape. Variance of columns in DE are the corresponding eigenvalues. These represent the amount of variance in shape captured by each eigenvector.

The mean shape amongst all shapes can be constructed using the mean of the coefficients. The effect of each eigenvector can be independently studied to understand which features of the shape change during deformation. To compare shapes of two entities such as a robot and an organism, variances of columns in the product matrices D_rE_o and D_oE_r (subscripts indicate robot or organism as an example) are considered. The resulting eigenvalues, computed between two sets of data, are thus a quantitative measure of similarity.

3.3 Case Studies

The method of describing shapes will now be applied to different organisms and robots. To capture shapes of the entities being studied, their movement was first recorded on video. Movement of the specimen can be described as a progression of shapes, each of which is captured in a single frame of the video. Individual frames were extracted as images and processed to extract the elliptic Fourier descriptors of shape (fig. 3.1).

Wherever required, these images were pre-processed to highlight the regions of interest. In cases where the image had poor contrast, such as in the recording of organisms in their natural environments with no artificial light, desired regions were marked by hand. This was not required for the case of the robots since experiments were carried out in a well lit area against a contrasting background. An automated computer vision method was used to extract the desired region in such cases. A median filter with a 3x3 kernel was used to remove noise in the images. The resolution of the camera used for capture resulted in a jagged contour (fig. 3.1b), which is likely to produce erroneous high frequency coefficients when performing Fourier analysis [123]. To avoid this, the image was dilated using a disk-shaped structuring element with a radius of 3 pixels. The contour of this smoothed region was then determined, encoded as a Freeman chain and the Fourier coefficients were computed.

3.3.1 Euglenoid Movement

The first specimen in this study is the euglenoid *Eutreptiella spyrogyra*, which is the main focus of the thesis. Biologists have found it difficult to describe the many shapes observed during euglenoid movement and have often used subjective terms such as 'ameboid' [133], 'peristaltic' [134] and 'deforming in all sorts of fashions' [135]. They have also been described as being 'complex and assuming manifold forms' [61]. By employing a mathematical description, we seek to present the shapes of the cell in a more tractable form.

Video of the euglenoid from [15] was analysed and the outline of the cell was extracted from each frame. Though the motion of the organism is in three dimensional space, a projection onto 2D and the evaluation of the contour is appropriate because the organism is predominantly symmetric with respect to the long axis of the cell. Movements that involve bending and twisting of the cell body can also be analysed, given an appropriate viewpoint. These are not considered in this study since the focus is on euglenoid movement.

The Fourier coefficients were estimated for each shape as described above. They were then reduced to a set of five principal components. Figure 3.4 presents the eigenvalues corresponding to these components. In this case, it is clear that the first three eigenvectors capture most of the variation in shape, with a cumulative variance computed to be 99.3%. The change in scores on these components during one cycle of motion is shown in fig. 3.5. The shape of the cell is also shown at multiple instances.

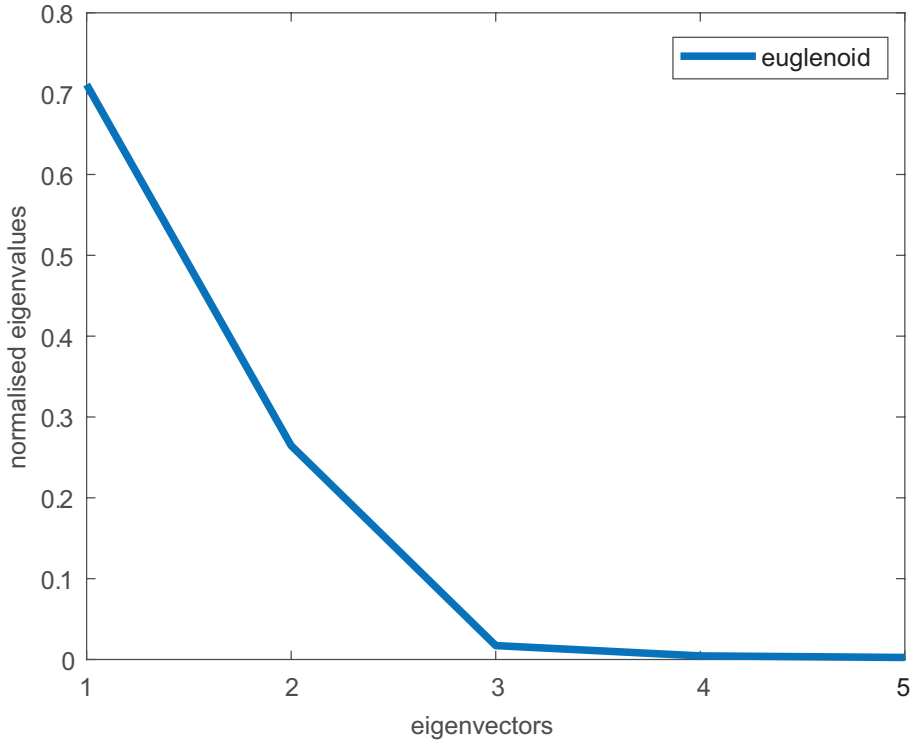

Figure 3.4: Normalised eigenvalues of the first five eigenvectors describing the shape.

To illustrate the effect that each principal component has on the shape, the scores on each component were independently varied up to two standard deviations away from the mean while those on the other components were fixed at their means. The recomputed shapes are shown in fig. 3.6. The central column shows the mean shape. Each row shows the effect of change in scores on one principle component. Each column away from the centre represents a change of one standard deviation.

The first principal component has a major contribution towards the width of the cell, thereby affecting the rounding up of the cell. The score on this component determines if the cell is slender and elongated or rounded up. As mentioned earlier, this is the most

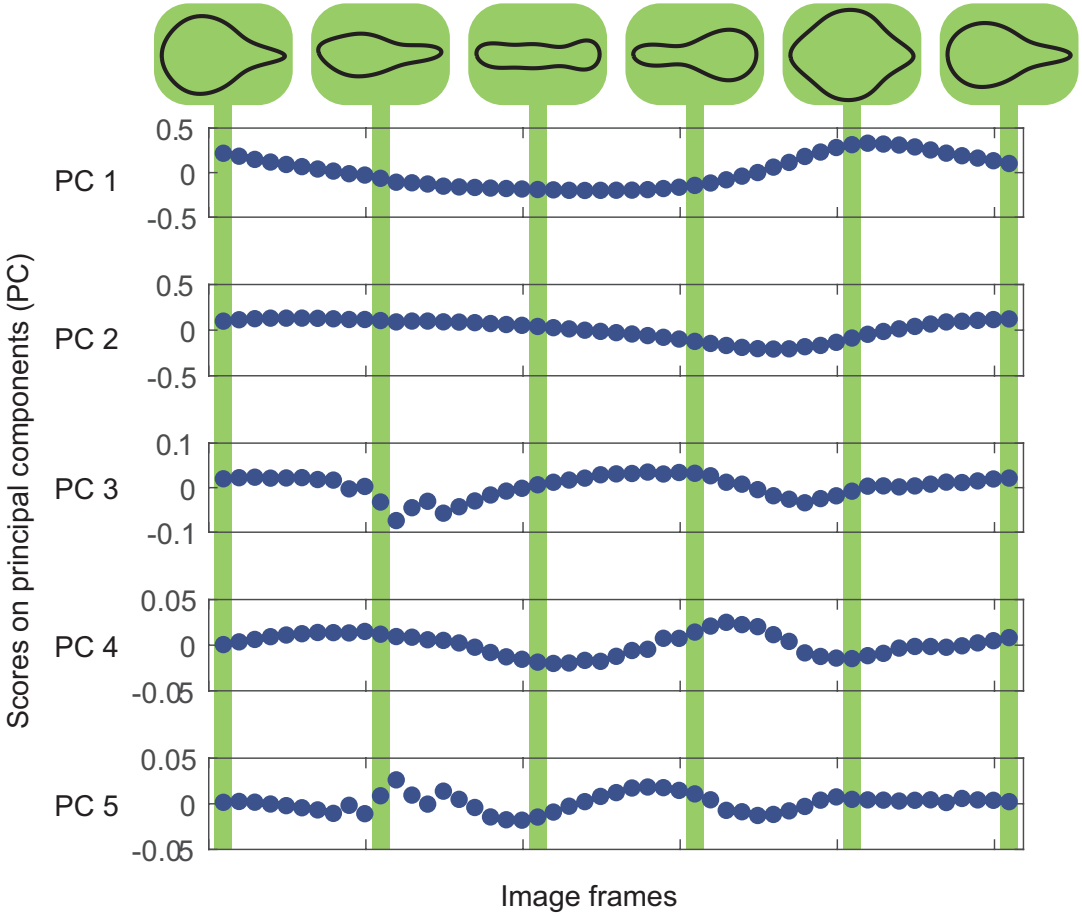

Figure 3.5: Change in scores on principal components describing the shape of the organism during one cycle of euglenoid movement. Reconstructed shapes are shown above for the scores indicated in the plots.

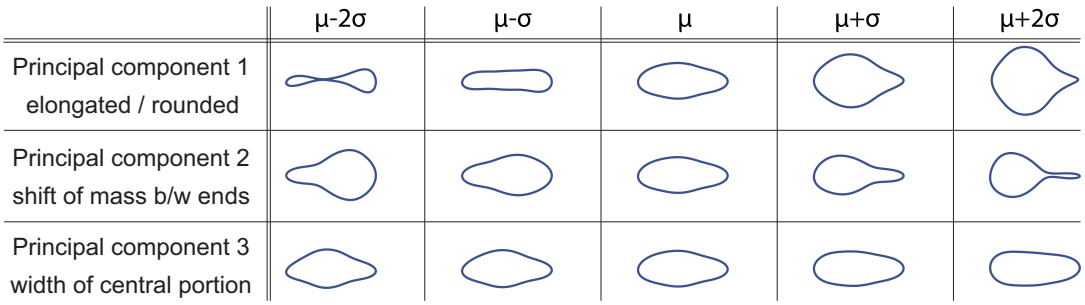

Figure 3.6: Effect of change in scores of each principal component on the estimated shape of the euglenoid. Each row corresponds to change in score of one principal component. The central column represents the mean shape. On either side, are one and two units of standard deviation away from the mean.

prominent feature of euglenoid movement and the score on this component is a way to quantify it. The second component captures the shifting of mass between the anterior and posterior of the organism. This anterio-posterior transport of mass generates the thrust required to generate movement [69]. The third component captures the width of the central portion of the cell. This analysis informs the design of the soft robot (discussed in the next chapter) in terms of the changes in shape that are required to achieve locomotion.

This study looked at cell shapes during euglenoid movement. A future study could look at shapes of the cell as it interacts with its environment such as when it is in close proximity to an obstacle, changes direction during photo-taxis or when it reacts to a change in the viscosity of the medium. The order of the principal components in these studies would indicate the physical significance of the above mentioned changes in shape. Results from those studies could potentially be used to infer about the open or closed loop nature of the controller governing the movement of the cell, about which little is known. A possible hypothesis to test is that the shifting or mass occurs in an open manner whereas the more subtle features of shape change with feedback that the cell receives from interacting with its surroundings.

3.3.2 Crawling Motion of Caterpillars

The crawling motion of two different species of caterpillar was studied next. The first organism, the *Manduca sexta* (tobacco hornworm) has been described as an ideal organism to study soft-bodied locomotion [136]. This caterpillar shifts the segments of its body as a succession of steps, delayed in phase, from the posterior to the anterior. In the second species, *Sphacelodes sp.*, there is a more pronounced change in the body shape termed "inching" locomotion, with the organism curling up into a circle similar to the Greek letter Ω (fig. 3.7c). Videos analysed in this section were provided by Professor Barry Trimmer, Tufts University (personal communication, Dec, 2017).

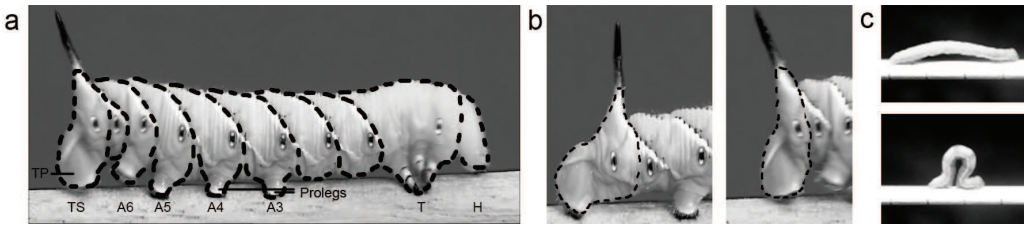

Figure 3.7: (a) Segments on the body of the *Manduca sexta* as identified in [136], marked using dotted lines: (TS) terminal segment, (TP), terminal proleg, (A3-A6) abdominal segments, (T) thoracic segments and (H) head. (b) Close up views showing the extension and contraction of the terminal proleg. (c) Two frames from the motion of the *Sphacelodes sp.* showing the neutral from and characteristic curled up Ω form.

Movement of both the caterpillars was recorded in their natural environment. Indivi-

dual frames from the video (recorded at 30 fps) were processed manually to highlight the body of the caterpillar. This was necessary because the creatures were camouflaged and it was not possible to isolate the creature from its background using an automated computer vision technique. In both cases, 6 harmonics were sufficient to capture the details of shape.

Deformations of the body during locomotion of the caterpillars, *Manduca sexta* and *Sphacelodes sp.* are shown in fig. 3.8. Again, scores on the first two principal components were varied to illustrate the effect of their change on specific features of the shape. The difference in gaits of the two species is immediately evident. The first principal component in the case of the *Manduca sexta* captures the convexity in the shape of the body. In other words, it gives information on whether the body is raised or lying flat on the ground. The location along the length of the body where the body is raised from the ground is captured by the second component. In the case of the *Sphacelodes sp.*, the first principal component again describes the convexity of the body. It is more pronounced in this case, capturing the curling up of the body. The second component represents the leaning of the body in the curled up configuration, either towards the anterior or the posterior.

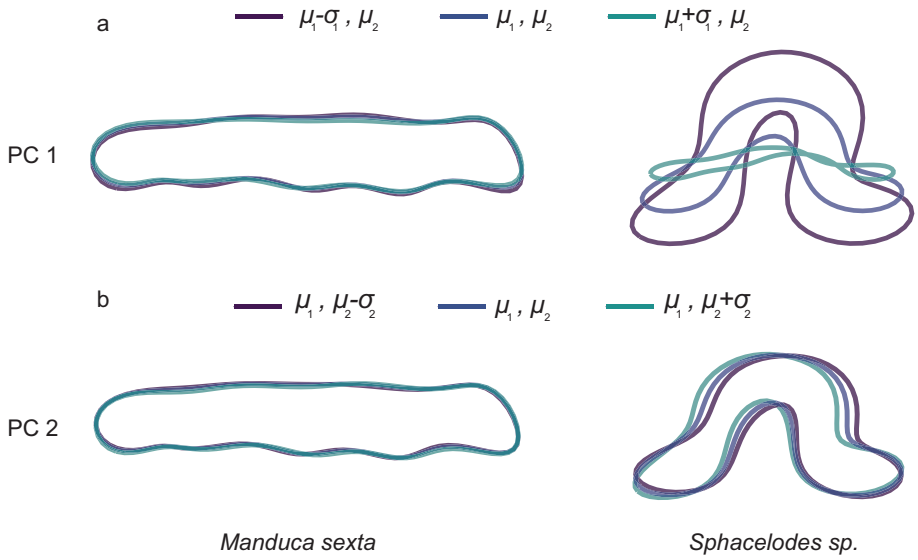

Figure 3.8: Effect of changes in the first two principal components (a and b) on the estimated shapes of *Manduca sexta* (left) and *Sphacelodes sp.* (right)

In addition to looking at the deformation of the whole body of the caterpillar, changes in shapes of individual segments of the body in the case of the *Manduca sexta* were also analysed. Individual segments of the body were identified [136] (fig. 3.7) and marked by hand on each frame of a high resolution video showing the creature in motion. In particular, abdominal segments A3 to A6 and the terminal segment, TS were analysed. Movement of the thoracic segments was not considered as it has been found that they are not necessary to achieve locomotion [136].

Changes in shape of individual segments of the *Manduca sexta* are shown in fig. 3.9.

The first principal component was varied while keeping the second component fixed at the mean. To understand the phase difference between movement of segments, the scores on these components are plotted as function of time (fig. 3.10).

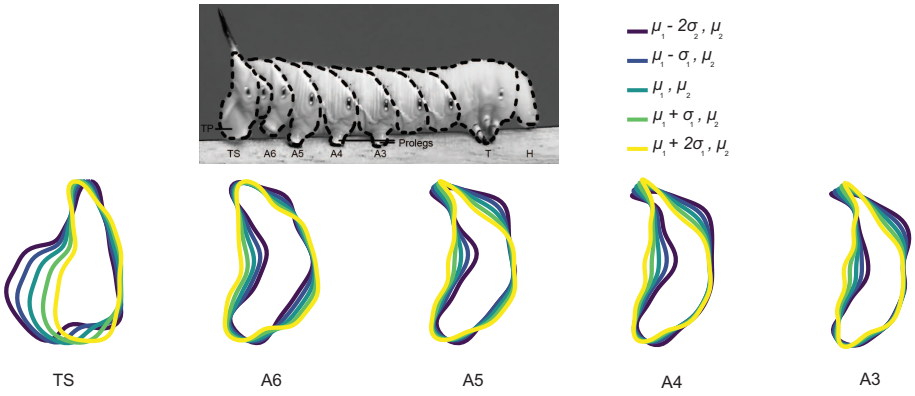

Figure 3.9: Effect of changes in the first principal component on the estimated shapes of segments in the *Manduca sexta*. (TS) terminal segment, (A3 to A6) abdominal segments (defined in fig. 3.7).

Since the principal components capture the most significant changes in shape, analysis of individual body segments revealed interesting insights regarding the nature of movement of each segment. The most prominent change is seen in case of the terminal segment, where the shape changes are due to the extension of the terminal proleg (TP). The extension of TP (fig. 3.7b) proceeds the swing phase of the segment at the start of each crawl cycle and has been described as being a distinctive feature of caterpillar locomotion [136]. This extension represents the drag force component of the stance phase which is a characteristic of the tension-based crawling strategy used by *Manduca* [137]. This key feature is captured by the first principal component (fig. 3.9). In addition, the kinematic analysis of movement of the abdominal segments [136] revealed that segments A3 to A6 see little extension of the prolegs. This is seen in fig. 3.9 where there is no significant change in the shape towards the bottom of the segments A3 to A6. On the other hand, the segments bulge out towards the top and curve inwards near the middle. More analysis is required to understand what these changes represent and if they are purely a result of the rotation of segments or if they are caused due to movement of internal organs which has been observed in the *Manduca Sexta* [138].

The principal component scores plotted against time for the various segments (fig. 3.10) show the progression of movement from the posterior to the anterior through the abdominal segments. There is about 2.5s of phase delay between the motion of the segments which agrees with the results from the kinematic analysis [136]. This demonstrates potential for the use of the shape descriptors in combination with eigenanalysis to discern dynamic properties of locomotion.

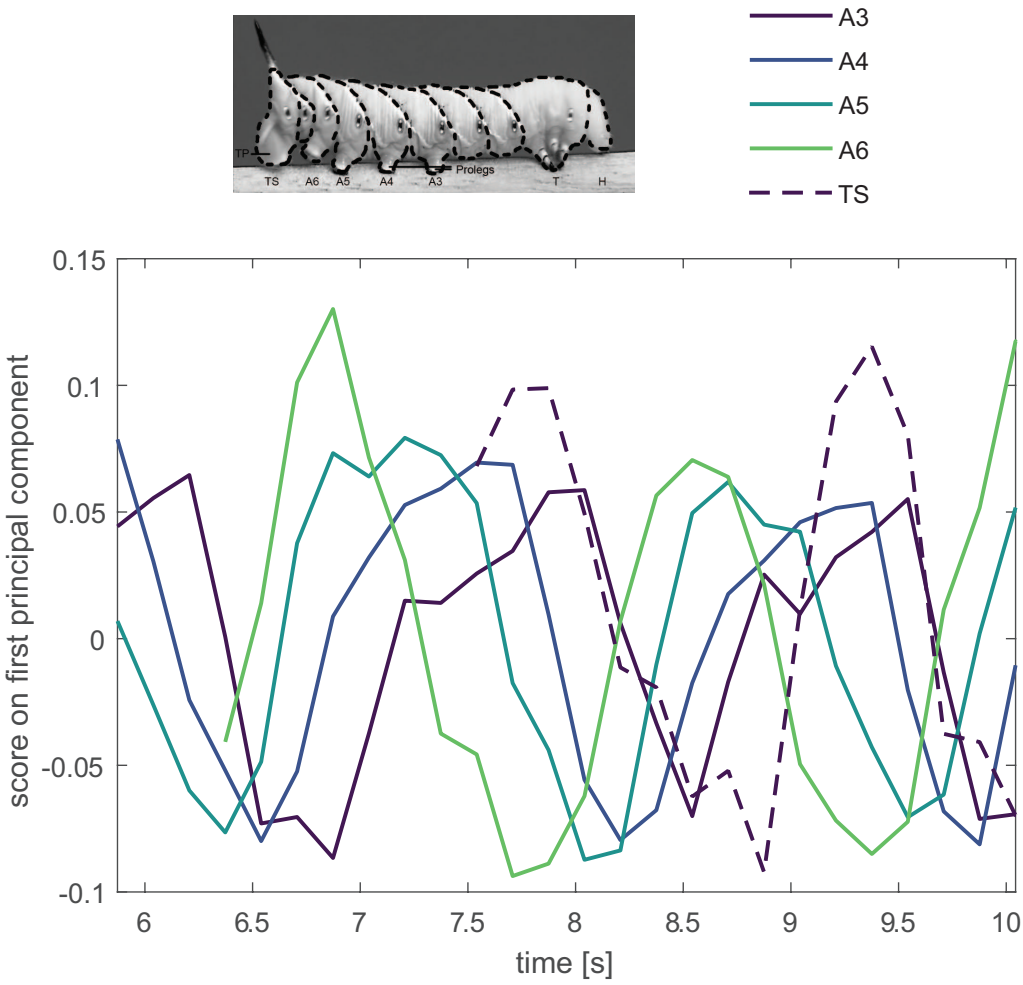

Figure 3.10: Scores on the first principal component for five segments (A3-A6, TS) in the *Manduca sexta* as a function of time.

3.3.3 Soft Tentacle

In the next case study, the movement of a soft tentacle [122] was analysed. This is an entirely passive structure with no sensors or actuators present along its length. In the presence of an oscillatory actuation at one extremity, the shape of the body is purely a result of its interaction with the environment. The behaviour of the material of construction (Ecoflex 30, Smooth-On) is non-linear [139]. The deformation of the structure and shape of the body are difficult to predict. This makes it a suitable candidate to apply the model-free approach.

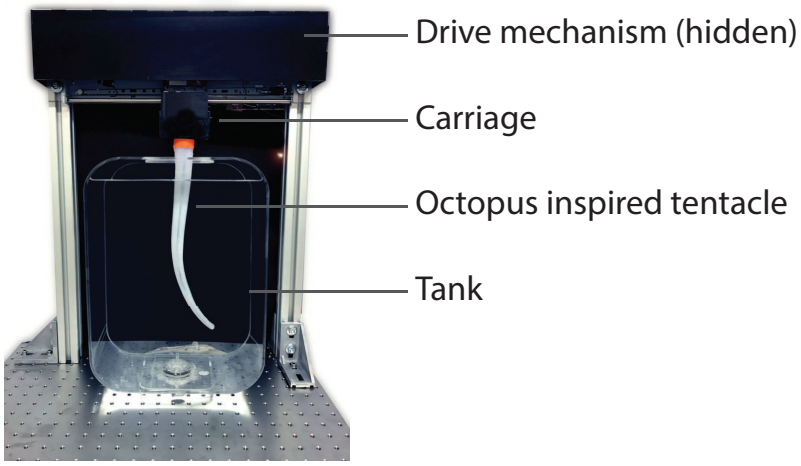

Figure 3.11: Experimental set-up of the passive tentacle. The tank was filled with either water or air. An oscillatory input was provided at one end by moving the carriage. Adapted from [122].

The tentacle was suspended from a movable platform and enclosed in a tank filled with either water or air (fig. 3.11). The platform was oscillated along a horizontal rail at a frequency of 3Hz and an amplitude of 12.5mm. The choice of this input is arbitrary and was primarily motivated by the mechanical constraints of the linear stage. Other frequencies and amplitudes were experimented with and resulted in similar motion. They are omitted here to avoid repetition. The experiment was performed twice, once with water in the tank and the other with air. The deformation of the tentacle in the plane of motion was recorded at 30fps using a camera (Fujifilm S2100HD). Descriptors of shape were extracted from each frame using an approximation of up to 20 harmonics.

The data from the shapes was then reduced to three principal components. The first two components are shown for each frame of the swinging tentacle in fig. 3.12 and 3.13 (a,b). Horizontal lines in the plot indicate one standard deviation (σ) from the mean (μ). To illustrate the effect of principal components on the shape representation of the robot tentacle, weights on the components were independently varied up to two standard deviations on either side of the mean and the reconstructed shapes have been plotted. Figure 3.12c, 3.12d correspond to the case when the tentacle is moving in water and fig.

3.13c, 3.13d correspond to that in air. The third principal component is not shown here and was fixed at its mean in all the reconstructed shapes.

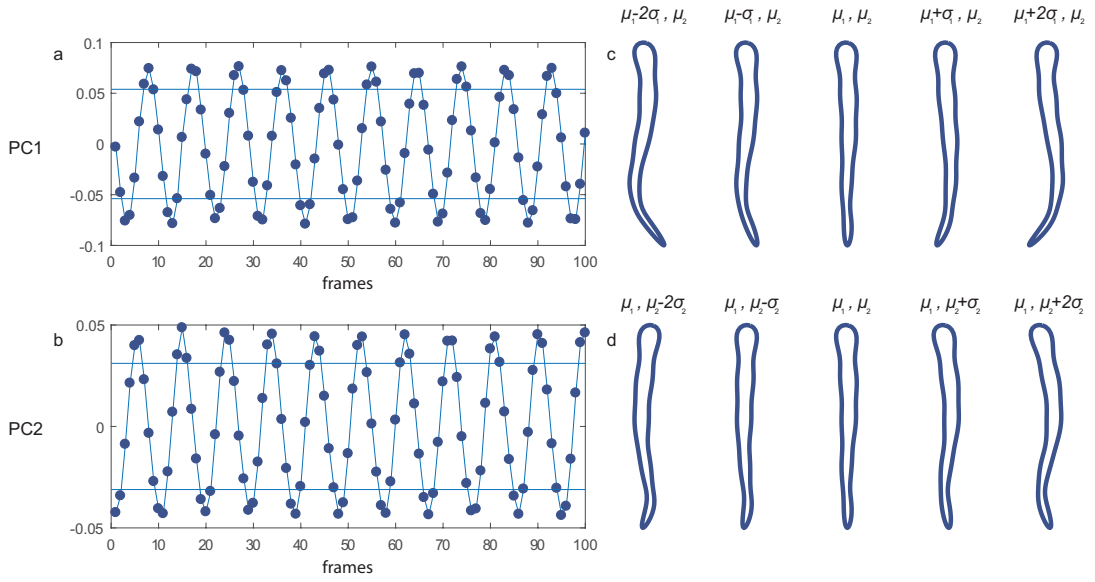

Figure 3.12: Estimated shapes of the tentacle when moving in water. Change in scores on the (a) first and (b) second principal components. (c) and (d) show the effect on shape due to changes in weights on these principal components. μ and σ indicate mean and standard deviation respectively. The subscripts indicate the component over which these were computed.

These results demonstrate the ability of the elliptic Fourier descriptors to describe the shape of deformable soft robot to an arbitrary degree of precision. The principal components describe different aspects of the shape. In case of the experiment in water, the first principal component captures the curvature of a larger portion of the structure (fig. 3.12c) while the second component has a more local influence and describes subtle changes in shape near the tip (fig. 3.12d). This implies that there is a more prominent global change in shape as opposed to the curving of the tip.

As expected, the shapes exhibited by the tentacle are different in various media. The shape has a higher order of curvature when the medium is water (S shaped, fig. 3.12) compared to that in air (C shape, fig. 3.13). Curving of the tip is not predominant when the medium is air. This is immediately evident when the shapes are plotted as points in the space of the components (fig. 3.14) The points have less span along the second principal component in the case of air. In terms of modes of vibration, movement in air can be described as being composed of fewer prominent modes than that in water, as shown by the principal components.

The case studies looked at motions that were periodic for the most part. This resulted in shapes that repeat periodically and hence the weights on principal components were also periodic (eg. fig. 3.12, 3.13). However, the analysis may also be applied to non-

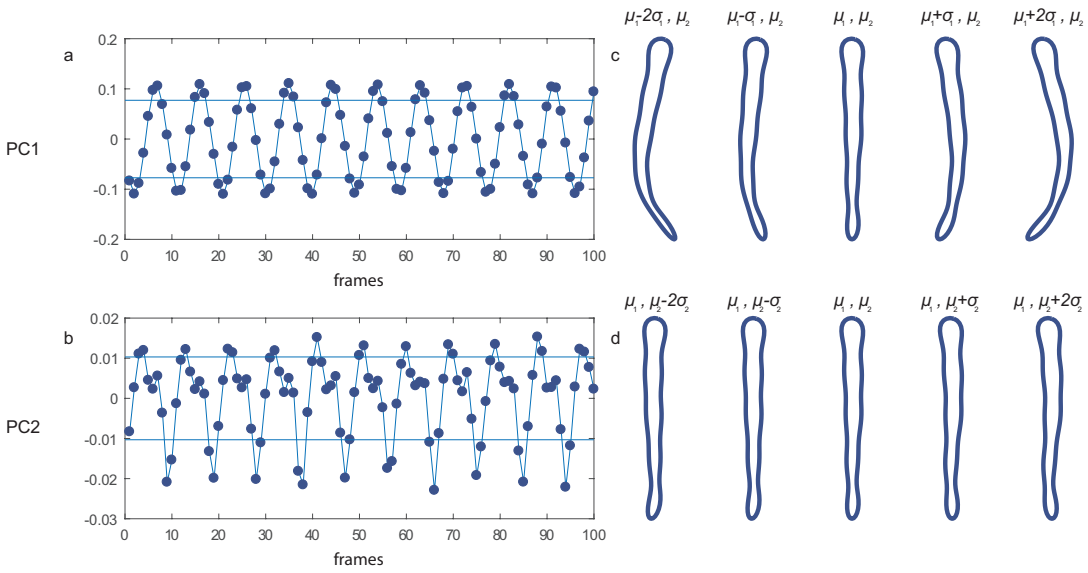

Figure 3.13: Estimated shapes of the tentacle when moving in air. Change in scores on the (a) first and (b) second principal components. (c) and (d) show the effect on shape due to changes in weights on these principal components. μ and σ indicate mean and standard deviation respectively. The subscripts indicate the component over which these were computed.

periodic movements. The same tentacle was made to oscillate in air with a randomised amplitude and frequency. The resulting shapes were analysed as before (fig. 3.15). The component scores are not periodic since a fixed frequency was not used. They also do not reach the same peak value at each extreme position of the swing. This is expected since the amplitude was not constant. However, conclusions about the key features can still be drawn and a similarity with that of the periodic motion in air is observed.

In this case, the observations vary depending on the duration over which they are made. Conclusions regarding the trends in shape captured by the principal components can still be drawn and are distinguishable in the figure even when the change in component weights is not periodic.

It is to be noted that the shapes of the tentacle in both the media have been analysed after a steady state of oscillation has been established. An interesting extension to the study would be to look at transient shapes during the onset of swinging within a given medium and those that arise due to a change in medium. This would help identify regions that interact the most with the medium. This insight could be used to either improve the design or place sensors on the body in manner that facilitates capturing the most amount of information regarding movement.

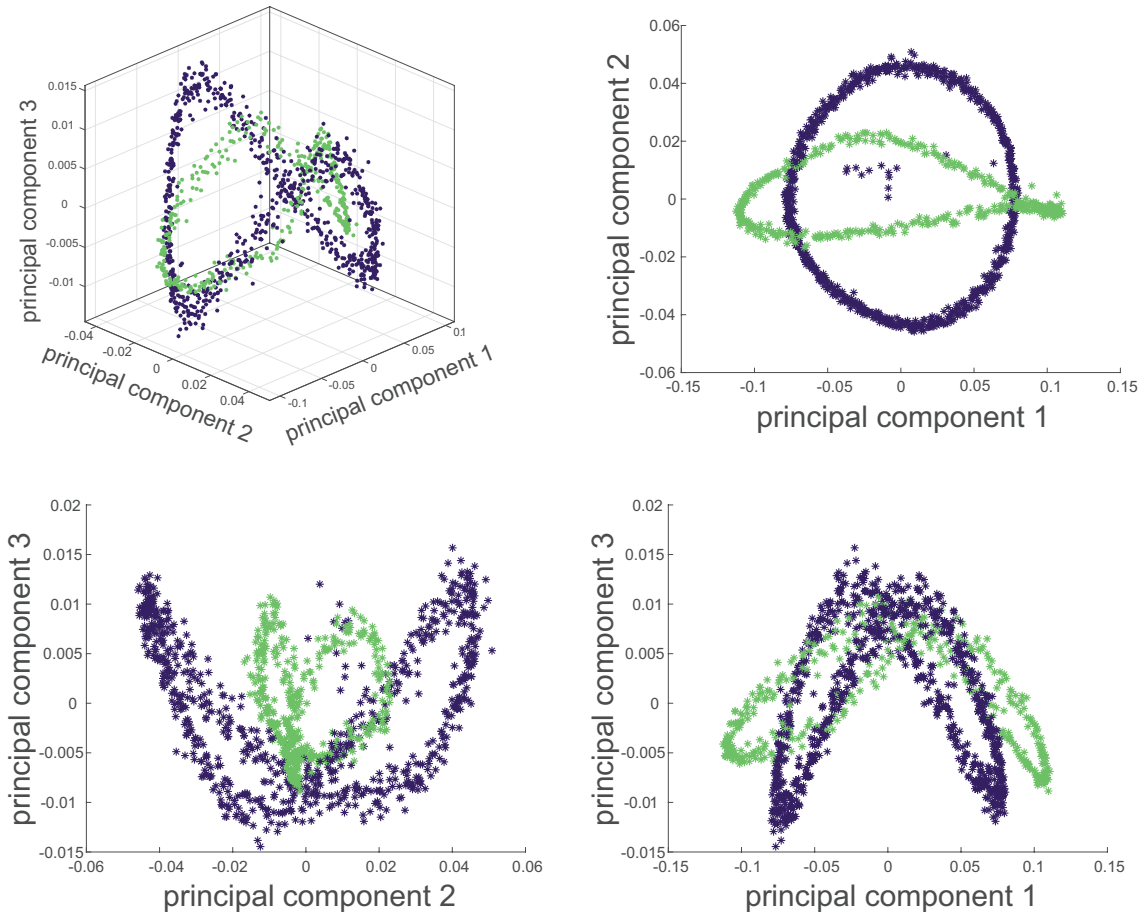

Figure 3.14: Shapes plotted as points in the space of the components. The motion of the tentacle is a closed loop in the space of the first three principal components. The curve in violet represents the movement of the tentacle through water. The green curve is for the experiment in air.

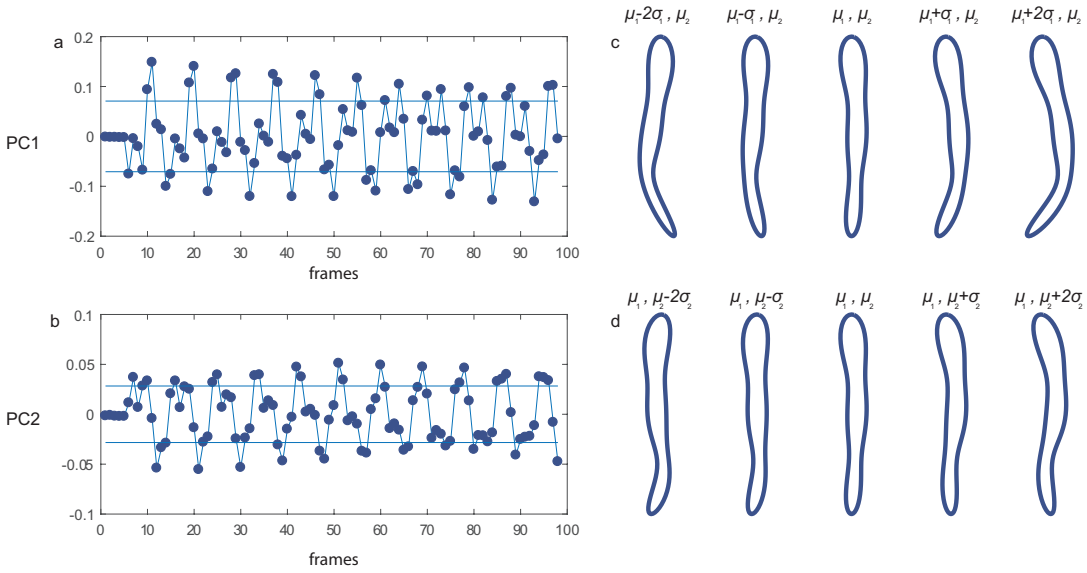

Figure 3.15: Estimated shapes of the tentacle when moving in air for a non-periodic signal. Change in scores on the (a) first and (b) second principal components. (c) and (d) show the effect on shape due to changes in weights on these principal components.

3.4 Extension to Three Dimensions

The analysis presented above was on two dimensional shapes of robots and organisms. The method of using elliptic Fourier descriptors can be extended to three dimensional movement. One possible extension would be to consider a third coordinate z in addition to the x and y coordinates and represent it as a Fourier series on its own. This method was followed to study the shape of the skull in rabbits [129]. It is to be noted that this method helps in describing three dimensional curves but not surfaces or volumes. An example would be the curve traced by the end effector of a soft manipulator.

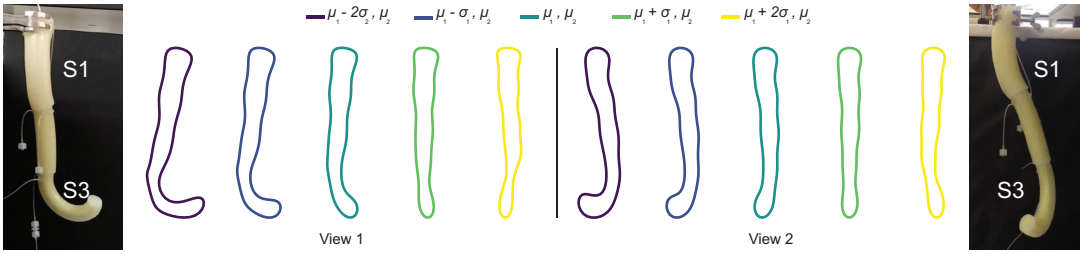

Figure 3.16: Estimated shapes of the active tentacle when captured from two perpendicular viewpoints. Bending of segment S1 is in the plane of the camera recording from view 2 and perpendicular to that from view 1 and is therefore not visible in the first camera. The effect on shape due to change in the first principal component for each view is shown.

A different approach is to treat the three dimensional object as a collection of two dimensional shapes. For instance, a study on the anatomy of the nasal cavity used 3D

geometry obtained from CT scans and sliced it into two dimensional curves, each of which was represented using Fourier descriptors [140]. A method of reconstructing the 3D geometry from sectional slices using radial basis functions was also proposed. In a similar manner, we visualise the three dimensional shape from two different viewing planes, essentially reducing the problem to a pair of simultaneous two dimensional representations. Since the silhouette is recorded in both the viewing planes, this approach captures surface projections of a three dimensional object. We applied this approach to the motion of an actively controlled soft pneumatic tentacle. Unlike the passive tentacle considered in the first case study, the continuum robot considered here consists of three segments that can be actuated independently and can bend in different directions. The tentacle was suspended from a rigid support and its motion was recorded from two perpendicular viewing directions. Two of the segments (S1 and S3 in fig. 3.16) were actuated to move in directions perpendicular to each other. The corresponding shapes and principal components are shown in fig. 3.16. The first principal component in each case clearly captures the deformation of the tentacle at different positions on the body as seen from the two viewpoints.

3.5 Limitations

In this section some of the limitations of using elliptic Fourier descriptors are pointed out. The descriptors only contain information regarding the perimeter of the specimen under investigation. Information concerning position and orientation of an entity is neglected. This limits their use in kinematic analysis of motion. For example, the analysis of body segments of the caterpillar cannot determine the degree of rotation or the vertical displacement of each segment during a cycle of locomotion. Using our shape descriptors in combination with other additional shape information such as a set of landmarks would help overcome this problem. In addition, some details of the shape are not captured. For example, points and features on the surface of the 3D object are not projected. There is therefore a partial loss in information in terms of the evolving location in space of these markers. Hence this approach may not be suitable for studies of mechanical interactions between objects and their surroundings where the interaction is defined by both the position and velocity of markers on the surface. Due to this reason, this approach cannot say anything about the frictional interaction between the segments of the caterpillar's feet and the substrate. Similarly, in the case of hydrodynamic studies it is unable to provide information regarding the flow of the surface.

Using multiple viewpoints of the 3D object has been proposed as a possible solution to capture more information about the shape of the deformable object. This approach may not be feasible in certain applications such as the study of microscopic organisms where it is difficult to obtain images from different directions with sufficiently high magnification. Additional information about the system can help overcome this limitation. An interesting

study is the flagellar swimming in the case of a uni-cellular organism (*Euglena gracilis*) where simultaneous knowledge of two dimensional shapes and the corresponding orientation of the object was used to reconstruct the three dimensional shape of a revolving object [77] thus recovering the lost information. In our study of the euglenoids, this was not a hindrance since the organism is approximately axisymmetric.

The descriptors are susceptible to artefacts caused during recording. For example, in earlier trials with the passive tentacle, the camera that was used to record motion was not sufficiently fast to capture the swinging movement of the robot. This resulted in some image frames containing a blur at the tip where the body was swinging at the fastest velocity. If not accounted for during preprocessing, the principal components capture this as a bulging of the tip. This might result in the under representation of some components, skewing the analysis. This is not a defect of the method itself but a consequence of error in recording or processing image frames.

3.6 Discussion

In this chapter, we have shown how shapes of soft bodies can be described using elliptic Fourier descriptors. The eigenshape analysis identified key features that change during the movement of these entities. The giant changes in shape during euglenoid movement were characterised. In the next chapter this description shall be used to aid in the design of a soft robot. The shapes of the euglenoid shall be revisited to make a comparison with those of the robot.

Differences in locomotion between two species of caterpillar were captured by the shape descriptors. In the case of the locomotion of the *Manduca sexta*, the analysis correctly identified extension of the terminal segment as the key feature of crawling. Dynamics such as cyclic shape change and phase delay between movement of segments were also captured. Different modes of oscillation were identified in various media in the case of the passive tentacle. We also showed that the method works across diverse scales ranging from microscopic organisms to centimetre scale caterpillars and artificial tentacles. These studies show that the method proposed in this chapter is applicable to a variety of deformable soft bodies beyond just the examples presented here.

Chapter 4

Giant Shape Change for Highly Deformable Soft Robots

The work described in this chapter has been published at the following peer-reviewed venues.

- **Digumarti KM**, Conn AT, Rossiter J. EuMoBot: Replicating Euglenoid Movement in a Soft Robot. *Journal of the Royal Society Interface*. 2018 Nov 21;15(148):20180301.
- **Digumarti KM**, Conn AT, Rossiter J. Euglenoid-Inspired Giant Shape Change for Highly Deformable Soft Robots. *IEEE Robotics and Automation Letters*. 2017 Oct;2(4):2302-7.

This chapter presents the design of a soft robot capable of achieving large body deformations. To achieve this change in shape, a pneumatic actuator with a novel operating behaviour was designed, taking insights from the analysis of euglenoid shapes seen in the previous chapter. The first part of the chapter presents the design objectives for the actuator, its fabrication and characterisation. The second part of the chapter discusses the construction of the autonomously operated soft robots called EuMoBots. This is followed by an experimental study into the locomotion of the robots. The hydrodynamic similarity in motion to that of the euglenoids is demonstrated. Furthermore, the multi-modal locomotion capability of the robots is presented.

4.1 Bio-inspiration from Euglenoid Movement

As described in section 2.3, euglenoids are soft bodied micro-organisms and can actively deform the shape of their cells. The cell transitions in shape between a slender form and a spherical form. Several intermediate shapes are also observed during this transition (fig. 1.1).

The analysis from chapter 3 highlighted certain key aspects of the shape that change during euglenoid movement, which we wish to capture in a controllable robotic form.

These features, as captured by the principal components of shape are:

1. Extension and contraction in length - shown by the 1st principal component;
2. Anterio-posterior transfer of mass - described by the 2nd principal component, and;
3. Change in radius - represented by the 3rd principal component.

In an experimental study [63], the shape of the cell in *Euglena fusca*, a relatively larger member of the *Euglena* family, was studied during euglenoid movement. The radius of the cell was measured at various points along the length of the cell. Unlike in the study from the previous chapter where several shapes were quantified, these measurements were restricted to two of the more extreme shapes, one being the slender form and the other the spherical form. In [63], they use the recorded data as a mathematical description of the shape. Their analysis showed that the length of the cell reduced by about 37% while the radius nearly doubled during the transition from the elongated form to the spherical form.

To achieve euglenoid-like movement, it is also important to replicate the transitions of shape and not just individual shapes in isolation. One observation in the euglenoids is that the cell is able to collect all its contents in a bunched-up space (spherical form). The other observation is that as the cell transitions out of this form into the longer elongated form, it does so by first extending a slender portion of the body (third and fourth frame in fig. 1.1). This happens prior to shifting of the mass and the associated appearance of a bulge. The method used to replicate euglenoid movement should also be able to capture these dynamics of shape.

The euglenoids achieve changes in shape by sliding strips of protein on their cell surfaces (see section 2.3). In this chapter however, we attempt to reproduce the shapes, and therefore the locomotion of euglenoids, without relying on the mechanism seen at the microscopic scale in the euglenoid pellicle. The focus here, is on generating body-scale (global) deformations by not relying on organelle-scale (local) mechanisms, which will be considered in chapter 5.

4.2 Biomimetic Soft Actuation

The studies presented above indicate the requirements for the design of a euglenoid-like robot by providing insights into the features of shape and the extent to which they change during euglenoid movement. A selection of the most prominent soft actuator technologies are now reviewed in this context, that have the potential to achieve the high strains discussed above.

Hydrostatic skeletons are commonly found in invertebrates and worm-like organisms. A primary feature of these is a cavity that operates with constant volume that is surrounded by muscles. These muscles may be arranged in longitudinal, circumferential, radial,

transverse or helical orientations in relation to the cavity [141]. Some may feature a combination of muscles in multiple configurations. The cavity is usually filled with water, which resists volume change due to its high bulk modulus and therefore, a contraction of these muscles results in a shortening of the length and an increase in the diameter, or vice versa.

Designs inspired by these arrangements of actuators have been used in the construction of robots. A purely mechanical example is the SoftWorm [142]. This design uses a single motor pulling on circumferential cables within a rhomboidal braided mesh to achieve a continuous peristaltic motion. A second example is the CMMWorm [143], which has actuation in both the circumferential and longitudinal directions. These designs are mechanically complex and require large structures to accommodate large actuators.

In contrast, the Meshworm presented in [27] is completely soft and flexible. Coiled shape memory alloy actuators [107] are used to generate peristaltic movement and the robot can handle mechanical impacts. However, these actuators have a slow actuation-relaxation cycle. Their antagonistic arrangement results in limited stroke length and therefore cannot produce the large strains required.

Muscular hydrostats, such as the tentacle of an octopus, have also been used as biological inspirations for soft robotic actuators. The robotic tentacle from [144] is an example. Once again, the advantages are continuous motion with no rigid parts. These designs are capable of exhibiting bending and twisting motions, but are not well suited for large volumetric change because of the tight integration of muscle-like actuators and hydrostatic structures needed to deliver significant forces.

Origami inspired structures are an alternative approach to designing worm like robots [145] and soft actuators [146]. Making use of particular folding patterns, these structures undergo a change in shape upon actuation. Expanding structures using shape memory polymers arranged in specific patterns have also been developed [88]. Such actuators could be used to achieve control over deformations. However, their design and control is not straightforward.

In a recent study, we have investigated auxetic structures as a means of generating interesting mechanical behaviours and shape complexity. We designed cylindrical auxetic structures with various tiling patterns and characterised their behaviour. Using a combination of patterns, the change in length and change in radius of the structure can be coupled in novel ways. While they are an attractive choice for the design of soft robots, it remains to be seen if auxetic behaviour is essential to obtaining euglenoid-like shapes. A combination of auxetic and regular meta-materials could be a possible solution. These structures are discussed in greater detail in chapter Appendix B.

Soft active materials such as dielectric elastomers have been used in a worm-like robot [147]. The design exploits hydrostatic coupling between membranes [148] of these electro-active polymer actuators. Though large strains have been reported in the dielectric elastomer literature [149], they are not sufficient enough for this study. Additional

disadvantages include their reliance on high electric fields and their low reliability.

Yet another approach is based on granular jamming [150]. By changing the volume of the confining space, particulate material can be made to behave both like a solid and a liquid [150]. This technique has been used in [151] to design a soft robot that moves by changing the stiffness of individual sections. The robot presented is almost spherical but this concept could be extended to euglenoid-like shapes. However, it is not clear if this actuation produces the desired amount of strain in the material to show a drastic change in shape. Additionally, the ability to modulate stiffness is not, at present, seen as a requirement in a robot that mimics euglenoid motion.

4.3 Hyper-Elastic Bellows

A different approach to realising soft robot actuators is the use of pneumatic chambers [152]. These have been used in many applications ranging from micro scale actuators [153] to macro scale robot locomotion [30]. Exploiting their ease of fabrication, benefits of rapid expansion [154], minimal control and repeatability of actuation, these soft fluidic actuators have been chosen as suitable candidates in this study. We designed a novel bellows-like pneumatic device that captures and separates two of the key features of euglenoid motion: axial extension and contraction, and radial expansion. This is termed the Hyper-Elastic Bellows (HEB) actuator [155].

The basic shape of the HEB is a soft, elastomeric, folded structure which changes shape as the internal pressure is varied. The design exploits the unfolding bellows structure and the hyper-elastic property of the elastomer to achieve a linear expansion followed by a huge change in volume when a positive pressure is applied. The folds in the structure also allow it to collapse to a minimum configuration when a vacuum is applied. Hence the actuator functions both under positive and negative pressure, and can exhibit both radial and axial expansion. This is a functional advantage over traditional actuators with pneumatic networks (eg. [152]) and other recent designs (eg. [156] and [157]) whose operation is restricted to a single regime.

Similar designs have been proposed recently and therefore a comparison is in order. Visually, the design appears similar to that of [158], a flexible manipulator designed for surgery. However, that design aimed to constrict radial expansion. In contrast, we exploit unconstrained expansion in radius to deliver greater activation sophistication. A second relevant design is presented in [159], where the aim was to induce a curvature in the actuator by imposing a constraint on one side of the bellows. Radial and axial expansion were not considered in isolation in that study.

4.3.1 Principle of Operation

Traditional bellows are designed for actuation only in the axial direction. There is negligible change in the radius. The geometry and the materials are chosen to maximise

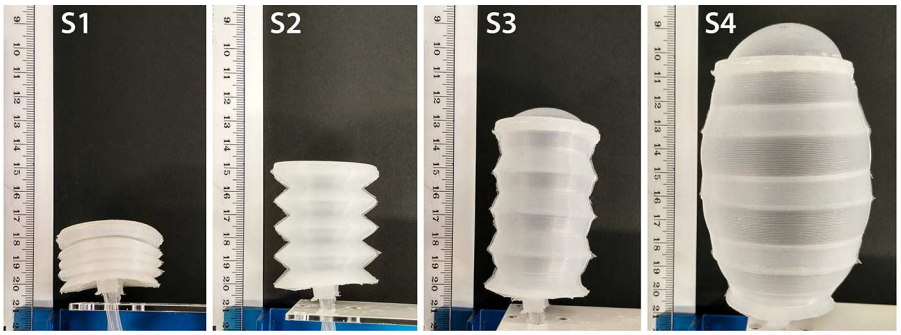

Figure 4.1: The four states of actuation. S2 is the neutral state of the actuator when both internal and external pressure are equal. Upon application of vacuum, the structure contracts axially to S1. When inflated, the membrane first stretches axially (S3), then balloons out (S4). An extremely large change in volume is observed from S1 to S4. [155] © 2017 IEEE

uniaxial actuation whilst minimising radial expansion. While this is the desired behaviour for many engineering applications, it is less attractive in the current study of euglenoid motion, where both axial and radial strains are large.

The soft HEB actuator (fig. 4.1, S2) when inflated at low pressures works in a manner similar to that of conventional bellows. It expands axially with negligible change in radius (fig. 4.1, S3). The difference in behaviour is observed at higher pressures, when the actuator starts expanding radially. This is possible because the folds of the bellows straighten out owing to the choice of the soft material used in their construction. The elastic nature of the material allows the expansion of the actuator like a balloon. This ballooning phase can be seen in fig. 4.1 (S4). In this manner an increasing pressure causes the actuator to transition from its rest shape (S2) to an elongated shape at first (S3), and then to a spherical shape (S4).

The elasticity of the material and the bellows design also ensures that the actuator returns to its original shape when deflated. When pressure in the fully inflated state is released the balloon shrinks and returns first to an elongated bellows shape (S3). As all pressure is released it returns to its original length with all folds intact (S2). Now a negative pressure can be applied to the actuator which causes the structure to compress axially and to collapse to a minimal-length configuration in which it is entirely folded (S1). In this way we can describe the actuator as having 4 states:

S1 Minimal length axially-compressed state ($L < L_0$, $R = R_0$, $P < P_a$),

S2 Rest bellows state ($L = L_0$, $R = R_0$, $P = P_a$),

S3 Axially expanded state ($L > L_0$, $R = R_0$, $P > P_a$),

S4 Ballooned state ($L > L_0$, $R > R_0$, $P \gg P_a$),

where L_0 is rest length, R_0 is rest radius, P_a is atmospheric pressure, L is current length, R is current radius and P is current internal pressure of the actuator. By exploiting these four states we design multi-segment soft robots that mimic the giant shape changes of euglenoid motion.

4.3.2 Fabrication

The HEB actuator was fabricated by casting silicone elastomer in a 3D printed mould. A central core and two outer halves formed a cavity of the desired shape and thickness (fig. 4.2). The material used was Dragon Skin 10 SLOW (Smooth-On). This material is a two-component, platinum-cure, room temperature vulcanizing silicone elastomer. It shows up to 1000% elongation before breaking under a tensile load and is therefore suitable for large strains. The ends of the chamber were cast separately and bonded to the main structure using an adhesive, Sil-Poxy (Smooth-On). The adhesive has a modulus of elasticity that is similar to that of the silicone and therefore has a negligible influence on the performance of the actuator. The process of fabrication is listed out below.

- Step 1: Prepare the mould for casting by spraying a release agent. Mann Ease Release 200 from Smooth-On was used in our case.
- Step 2: Bring together the core and outer halves and fix them in place making sure to align the parts correctly. Using hot melt adhesive, seal the seams at all the mating surfaces to reduce flash during casting.
- Step 3: Measure out the required amount of silicone and mix the two components thoroughly.
- Step 4: Remove trapped air in the mixture by vacuum degassing. Leaving the material in the vacuum chamber for a few minutes (≈5min gave the best results).
- Step 5: After degassing, transfer the silicone mixture into a syringe with a nozzle of diameter compatible with that of the inlet to the mould. It is preferable to pour material into the syringe with the plunger completely removed rather than to suck material into it. This prevents introduction of air into the degassed mixture.
- Step 6: Inject the silicone mixture into the mould at a constant rate until it slightly overflows from the air vent. This indicates that the entire cavity is filled with material and the air has been pushed out.
- Step 7: Leave the material to cure in the mould.
- Step 8: Once cured, carefully pry apart the outer pieces of the mould. The cast bellows can then be extracted by removing it off the core.

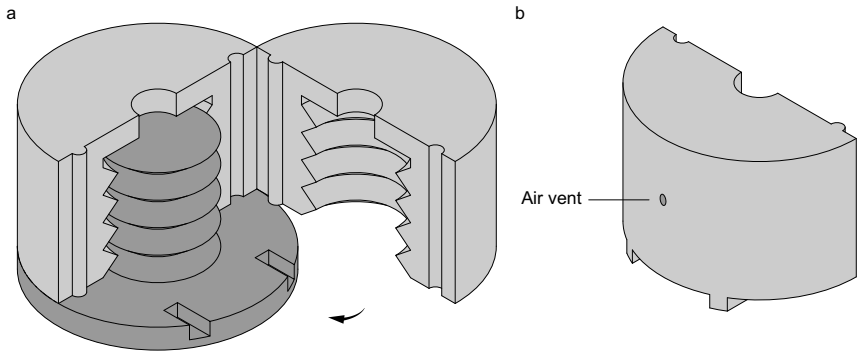

Figure 4.2: (a) The three-part 3D printed mould used to fabricate the HEB actuator. (b) One of the outer halves of the mould indicating the air vent.

Initially, a mould made of stacked acrylic sheets was used with the intention of rapidly prototyping designs. However, the interface between layers of the mould was not seamless and resulted in flash at the joins, leading to asymmetric expansion upon inflation (fig. 4.3). Since the spacing between layers could not be precisely controlled each time the mould was re-assembled, there was inconsistency in the behaviour of individual actuators [160]. When using the 3D printed mould, actuators were more consistent and showed symmetric expansion. The characterisation that will be described in section 4.4 also supports this claim.

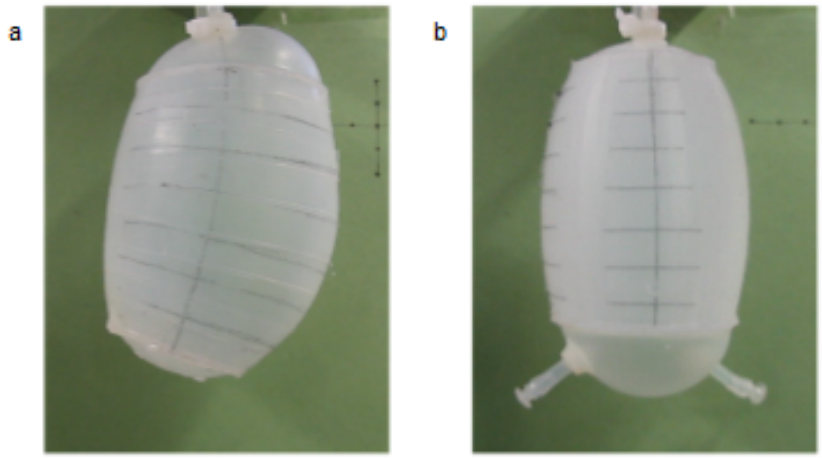

Figure 4.3: (a) Actuator cast in a stacked acrylic mould. The expansion is not uniform. (b) Actuator cast from a 3D printed mould. It shows a more uniform expansion. Adapted from [160].

At rest (state S2), each chamber measures 50mm in length with an inner diameter of 30mm and outer diameter of 45mm. The thickness of the wall is 2mm throughout. The half angle of the fold θ was chosen to be 38.66°. See fig. 4.4 and 4.6. A simulation of the behaviour for various angles is discussed in the next section.

The particular design used in this study has four folds spanning the entire length. An

actuator with these dimensions was used in the experiments characterising its behaviour (section 4.4). These parameters result in a chamber with large enough space to accommodate a pump on the inside. These parameters were used for evaluation only and the later experiments with the robots have smaller chambers.

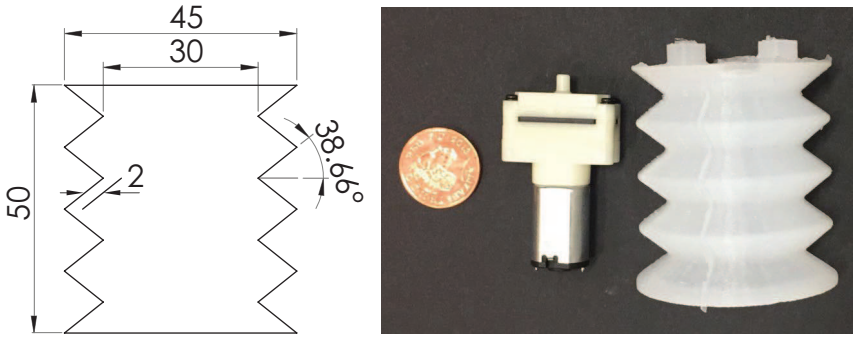

Figure 4.4: Design and dimensions of the HEB actuator. On the right is a comparison of the actuator and pump size with that of an English penny (20.3mm diameter). [155] © 2017 IEEE

Other bellows configurations were examined, including designs with more corrugations for the same length, but these resulted in actuators that did not expand or contract as effectively. Increasing the number of corrugations for a given length, while keeping the angle constant implies that the folds are less pronounced. This resulted in stiffer bellows that transitioned from the rest state to the ballooning state directly. The stiffness also prevented them in achieving the minimal length compressed state.

While this study used a simple angular design for the corrugations, other configurations may also be used. A study of these is presented in [161] which discusses the effect that the shape of the fold has on the behaviour of the bellows. These were not fabricated in this study as the simple design proved to be sufficient in achieving the strains seen in euglenoids.

4.3.3 Finite Element Analysis

To examine the effect of the half angle θ (see fig. 4.6), on the ability of the actuator to extend axially, a finite element analysis (FEA) of the expansion of a single fold of the bellows was performed on models of varying angles. All the models had the same initial length. They also had the same wall thickness and diameter values as the HEB prototype mentioned above. A second order reduced polynomial model (Yeoh model [162]) was used for the constitutive relation based on material data from [163]. The only change is geometric and it is the angle of the folds.

The analysis was performed in ANSYS using solid geometries designed in SolidWorks. A fixed constraint was imposed on the top surface of the model. A pressure was applied on the internal walls of the cavity. During the simulation, the pressure was increased from 0 to 60mbar in 60 simulation steps. Figure 4.5 shows the model before and after the pressure

is applied. The colours indicate displacement from initial position in the axial direction. Strain in the axial direction (considered in terms of geometric deformation from initial position, $\Delta L/L_0$) as a function of internal pressure was analysed. A plot of the results for four different angles is shown in fig. 4.6.

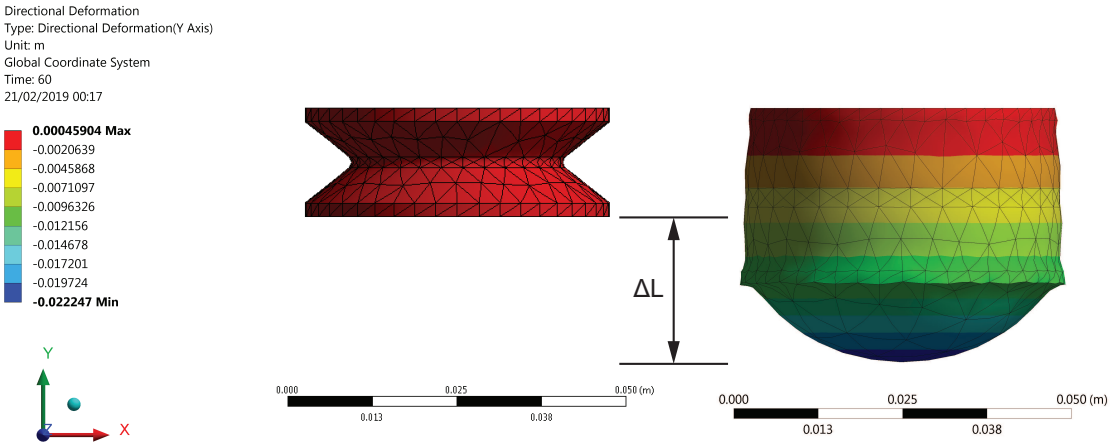

Figure 4.5: Figure showing the elongation of the HEB actuator, modelled with a single fold, upon pressurisation. The colour bar represents displacement from initial position in the axial direction.

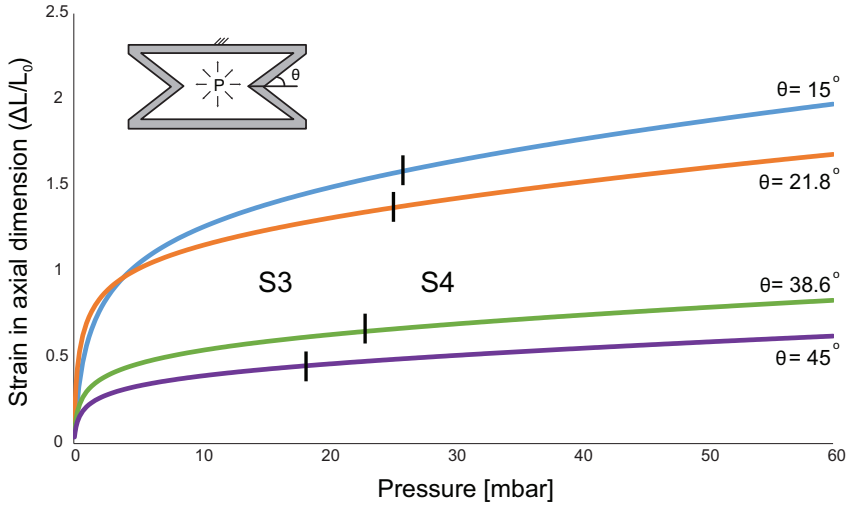

Figure 4.6: Axial strain as a function of internal pressure, obtained from finite element analysis of the expansion of a single fold of the bellows, with varying half angles, θ. Inset shows a sectional view of the 3D model used for FEA.

Two main conclusions may be drawn from the observed trend. The first is that as the half angle increases, the transition from axially expanded state (S3) to ballooned state (S4) occurs at a lower pressure. This is in agreement with what is expected. A larger angle implies that the chamber wall is closer to being flat and hence transitions more readily into the ballooned state. The second conclusion is that a smaller angle results in a larger strain in the ballooned state. This is also realistic, since the designs with smaller

angles have more scope for extension because they are more compressed to begin with. There is therefore a trade-off between transitioning to the ballooned state and the axial extension in that state for a given internal pressure. The FEA model thus provides a basis for optimization of the structure for different goals.

4.4 Characterisation of HEBs

The behaviour of the HEB actuator was characterised in terms of its elongation and compression in the axial and radial directions as a function of the internal pressure. The experimental set-up is shown in fig. 4.7. A single chamber with two ports was suspended from a rigid support. A micro pump (KPM14A, Yujin Electric), with a maximum dimension of 46mm and volumetric flow rate of 1.16ml/s, was connected to one of the ports to inflate or deflate the chamber. The other port was connected to a pressure sensor (Honeywell) that measured the difference in pressure between the inside of the chamber and the atmosphere. Prior to characterisation, the actuator was inflated and deflated multiple times to account for Mullins effect. A laser displacement sensor (KEYENCE LK-G152) was positioned below the chamber pointing upwards at its base. This provided an accurate measurement of the change in length in the axial direction. Actuation of the chamber was also recorded on video (Canon G9 camera). Expansion in the radial direction was measured through image processing. Frames from the video were extracted at 1s intervals. The width at the widest part of the actuator was extracted on each frame. Ten trials were recorded for each of the inflation and the deflation phases. The results are presented below. Volumetric change was measured separately using a syringe filled with water as it is nearly incompressible.

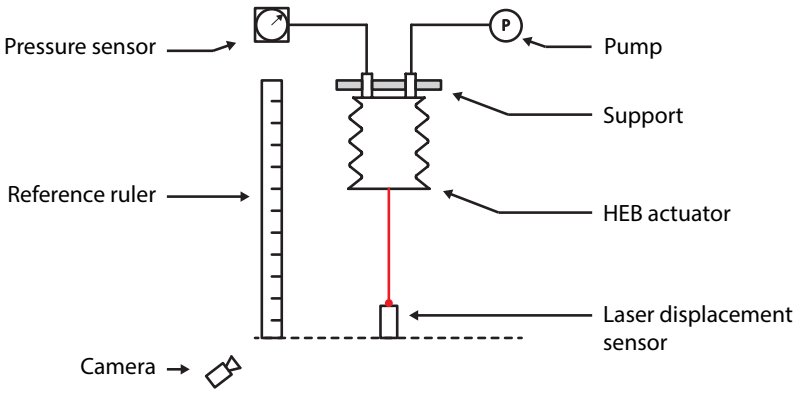

Figure 4.7: The experimental set-up used to measure axial and radial change in dimension of the HEB actuator. [155] © 2017 IEEE

4.4.1 Inflation Phase

During the inflation phase from state S2 to S4, when air is pumped into the chamber, two distinct behaviours are observed. First, the bellows extend, resulting in a quick linear

change in length. This corresponds to the steep section of the length change curve in fig. 4.8, labelled S3. This initial period lasts for a relatively short time (7s). There is a slight but negligible change in radius to accommodate the extension of the folds. Internal pressure increases linearly as seen in fig. 4.9. Once the bellows fully extend, the second behaviour is observed. This is the ballooning state, S4. There is comparatively gradual increase in length and simultaneous increase in diameter (fig. 4.8). The pressure increases slightly, but has a flatter profile indicative of ballooning (S4, fig. 4.9). Radial and axial expansion as functions of internal pressure are shown in fig. 4.10.

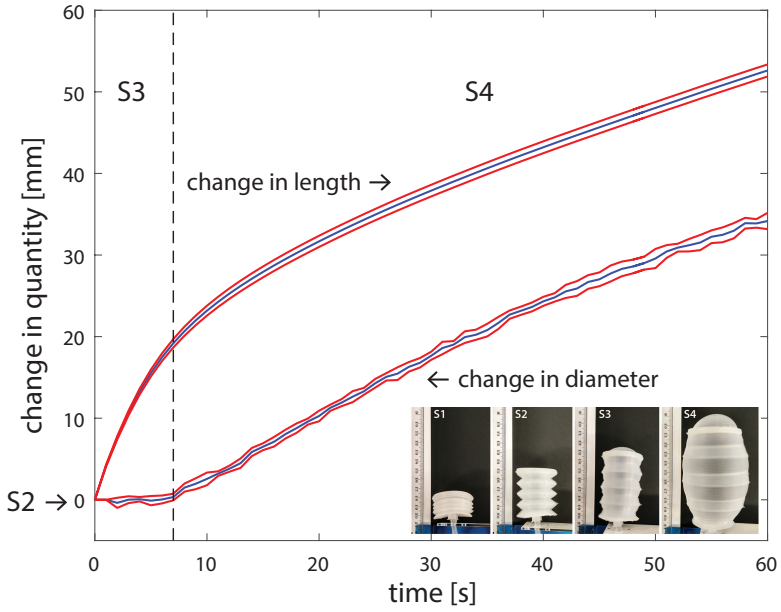

Figure 4.8: Mean change in length and diameter of the chamber as a function of time during inflation. The upper and lower curves for each plot represent one standard deviation from the mean. The actuator starts in the neutral state (S2). As the actuator is extending (S3), there is a steep increase in length and no significant change in diameter. Once the folds are fully extended, both length and diameter start to increase in the ballooning state (S4). [155] © 2017 IEEE

4.4.2 Deflation Phase

Starting from the rest position (S2), as air is pumped out of the chamber, no change in radius was observed. The bellows contract in length to state S1 and the trend is linear as can be seen in fig. 4.11. fig. 4.12 shows the change in internal pressure. A sudden drop in pressure towards the negative side indicates that the actuator has fully compressed. fig. 4.13 shows the contraction in length as a function of pressure. As read from right to left on the horizontal axis, a small negative pressure (less than 80mbar) is sufficient to cause the structure to attain a minimum configuration (length of 20mm when folds of the bellows are fully compressed, see S1 in fig. 4.1).

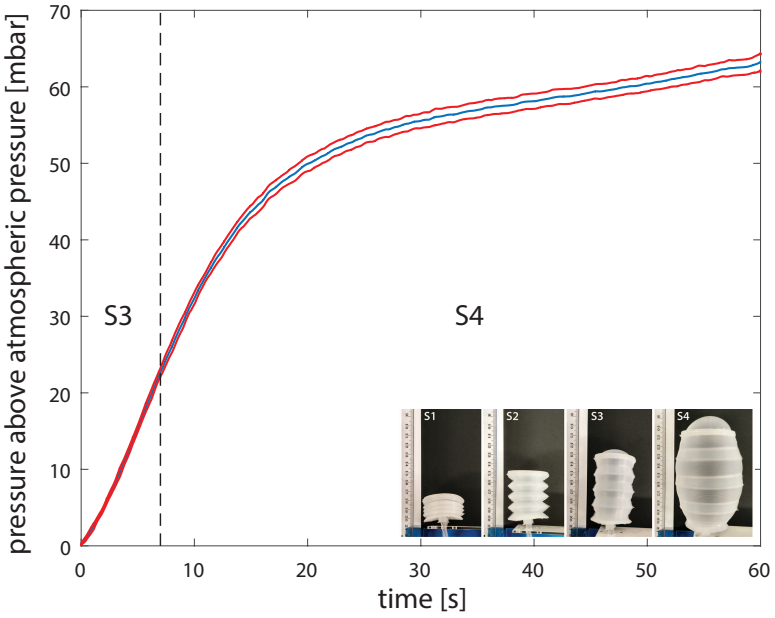

Figure 4.9: Mean internal pressure (above atmospheric pressure) as a function of time, measured over ten trials of inflation. The upper and lower curves represent one standard deviation from the mean. The beginning of the curve where there is a linear increase in pressure corresponds to the period in which the bellows are extending (S3). The later part corresponds to the ballooning period (S4). [155] © 2017 IEEE

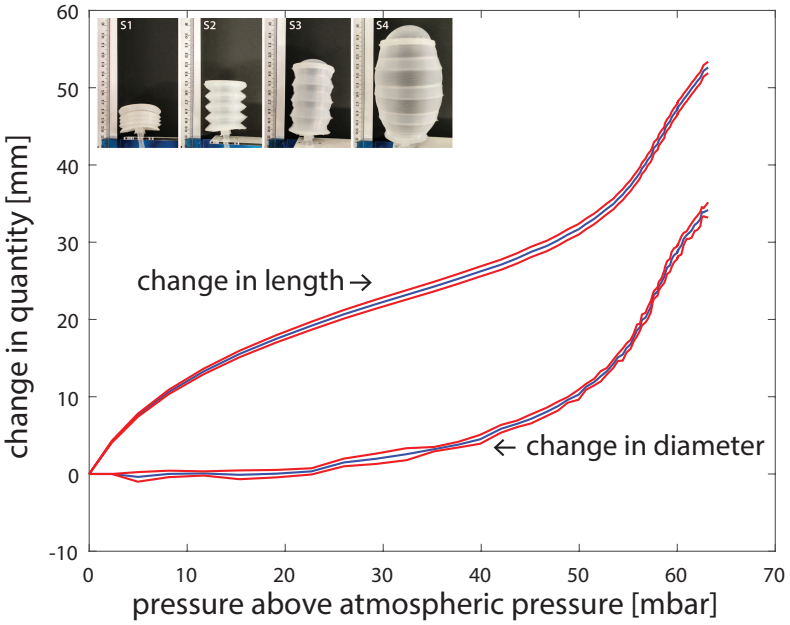

Figure 4.10: Mean change in length and diameter as a function of internal pressure computed over ten trials of inflation. The upper and lower curves for each plot represent one standard deviation from the mean. [155] © 2017 IEEE

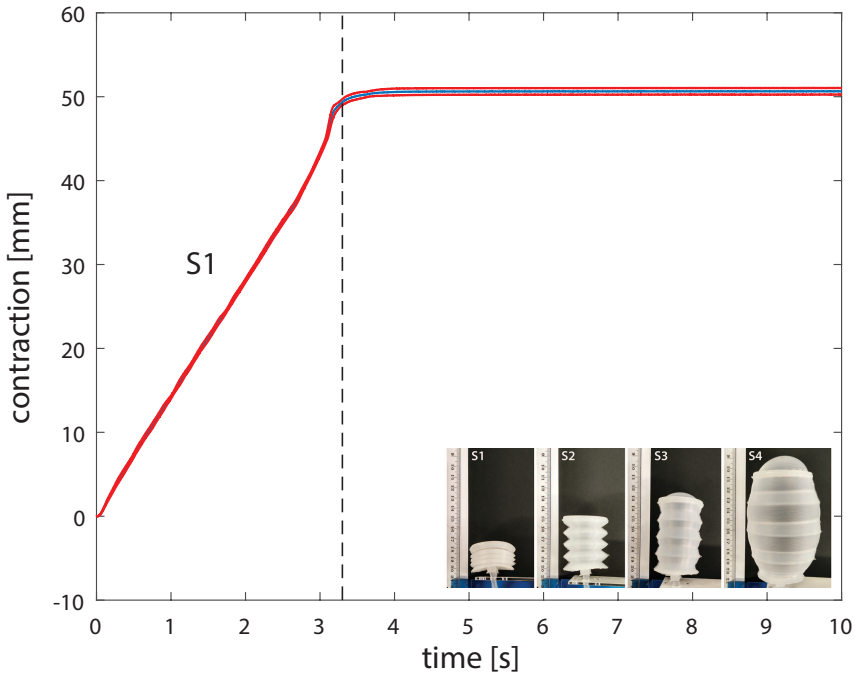

Figure 4.11: Mean contraction as a function of time measured over ten trials of deflation (S1). The upper and lower curves represent one standard deviation from the mean. A linear decrease in length is observed as the structure compresses to its minimum configuration. [155] © 2017 IEEE

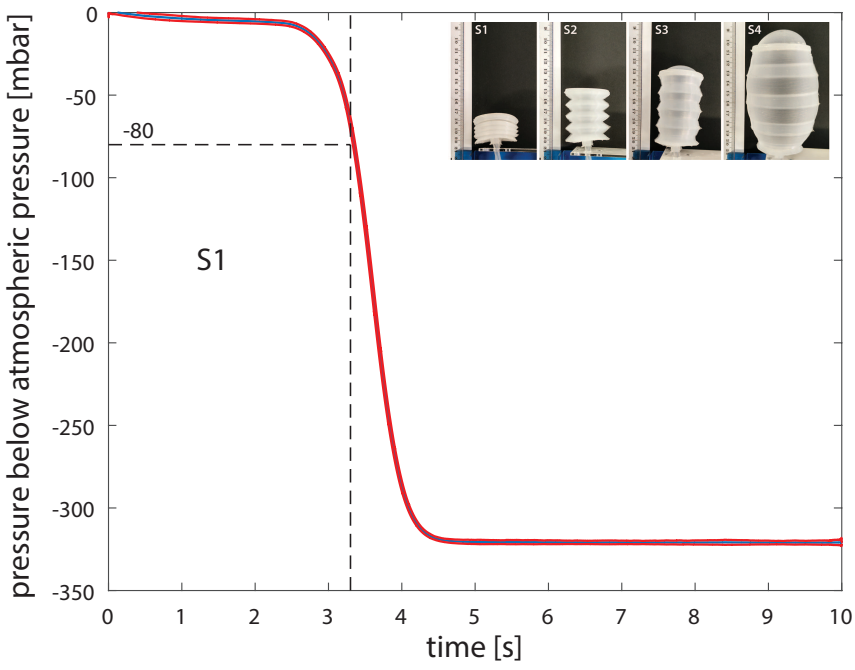

Figure 4.12: Internal pressure (below atmospheric pressure) as a function of time during deflation (S1), measured over ten trials. The upper and lower curves represent one standard deviation from the mean. A sudden drop and high negative pressure indicates that the structure has reached its minimum configuration at 80mbar. [155] © 2017 IEEE

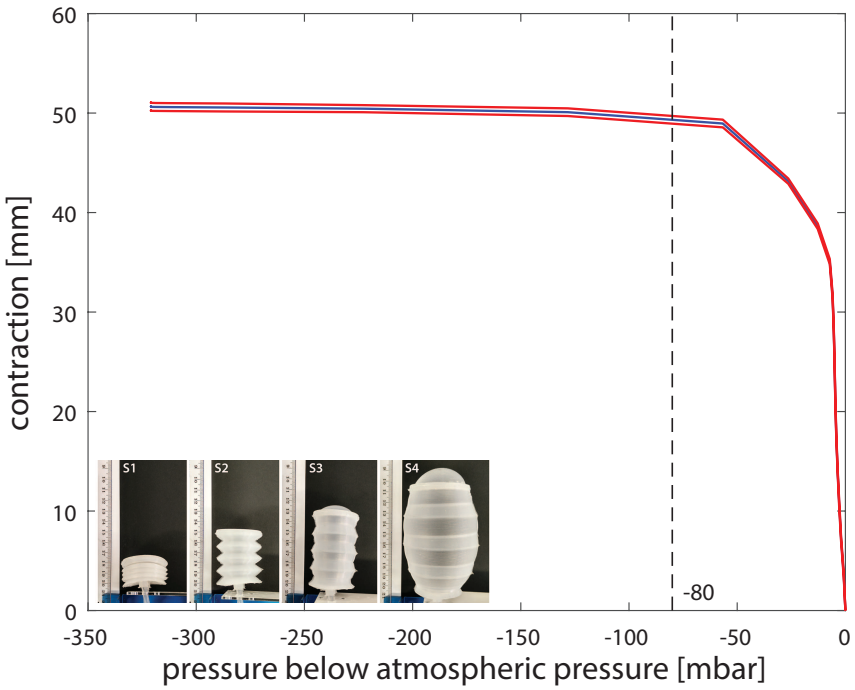

Figure 4.13: Mean compression as a function of internal pressure computed over ten trials of deflation. Reading from the right on the horizontal axis, the curve indicates that only a small change in pressure (80mbar) is required to reach a fully compressed state, starting from the rest state. The upper and lower curves represent one standard deviation from the mean. [155] © 2017 IEEE

4.4.3 Comparison with Other Classes of Actuators

The results show that the length of the soft pneumatic actuator more than doubles during the inflation phase (S2→S4). During the deflation phase (S2→S1) the structure compresses to its minimum possible configuration. This amounts to a total change in length of 450%. In the radial direction, there is 80% increase in diameter during expansion. The overall volumetric change from the fully compressed state to the expanded state was close to 300 times the minimum volume. The low standard deviation observed in all parameters, displacement, radial expansion and internal pressure across multiple tests suggests that the shape change is highly repeatable and readily controllable by adjusting the internal pressure accordingly.

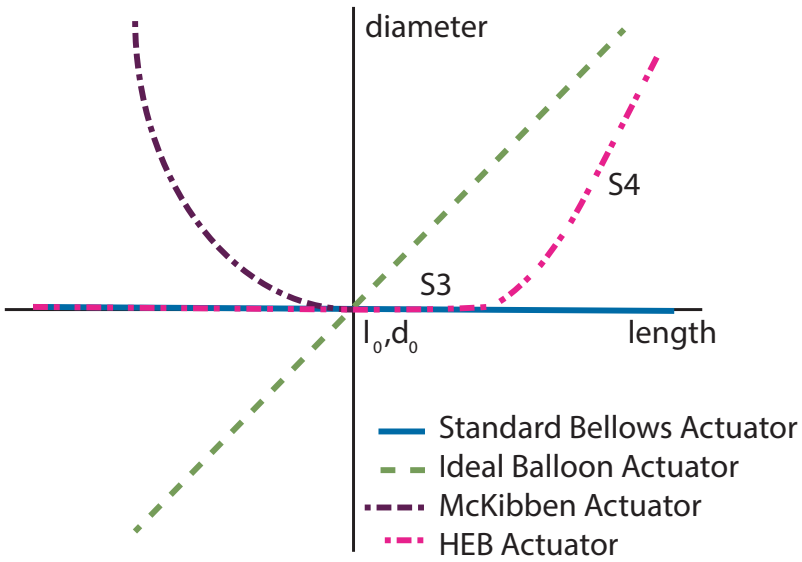

Figure 4.14: Comparison of different classes of actuators showing the relationship between diameter and length during actuation. All actuators are assumed to have an initial length of l_o and diameter d_o. [155] © 2017 IEEE

The conceptual relation between diameter and length for different classes of actuators is shown in fig. 4.14 and for the HEB design presented here in fig. 4.15. The HEB actuator is compared to standard bellows, an ideal balloon [164] and McKibben actuators. When actuated from an initial length of l_o and diameter d_o, a standard bellows actuator changes in length with negligible change in diameter. This is represented by the nearly horizontal line in the figure. An ideal spherical balloon actuator shows a linear relationship between its diameter and length. In a McKibben actuator, the diameter increases as it is pressurised causing a decrease in length. The HEB actuator presented here demonstrates a state of expansion in length with no change in diameter (S3) followed by a state in which both length and diameter increase (S4). Thus, it belongs to a class of actuators whose behaviour lies in between that of the standard bellows and ideal balloon actuators.

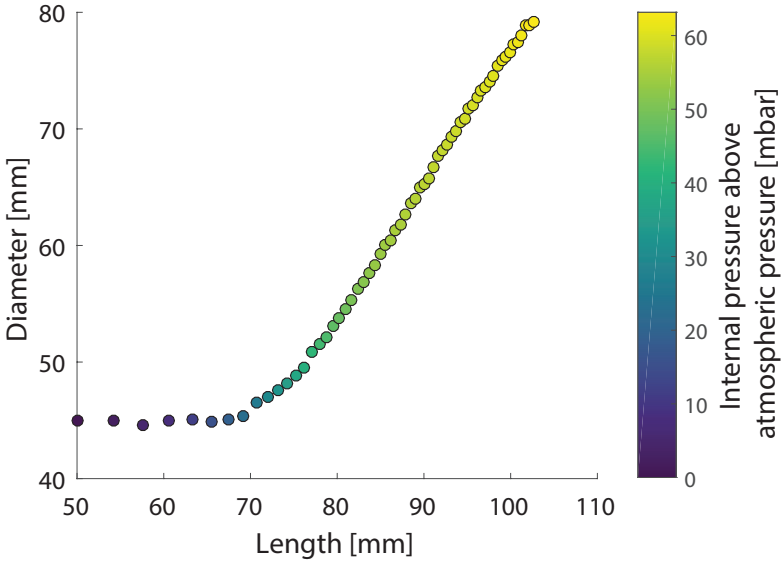

Figure 4.15: Relation between diameter and length for the actuator design considered in this study. Internal pressure is indicated by the colour of the data point. Initially there is no change in diameter as the actuator elongates axially. This is followed by the ballooning state in which a large radial and axial expansion is observed. [155] © 2017 IEEE

4.5 EuMoBot - Euglenoid Inspired Soft Robot

The HEB actuators presented above capture the key features of euglenoid movement while delivering large strains. They were used in the construction of soft robots (called EuMoBots [165], a portmanteau of euglenoid movement and robots) to demonstrate their potential in realising sophisticated euglenoid-like behaviour. This section describes the fabrication, control and an experimental study of the locomotion of these robots.

4.5.1 Fabrication

Multi-segment robots were fabricated by bonding together three of the actuators. Each HEB actuator chamber was cast separately as described in section 4.3.2. They were then bonded to each other using silicone adhesive. The chambers were isolated from each other by a thin layer of silicone of 1mm thickness. The elastomer cures to a translucent white colour. To visually distinguish the chambers and to allow for an autonomous vision based control of the robot (discussed in section 4.5.2), coloured pigments (Silc-Pig, Smooth-On) were mixed with the elastomer before the actuators were cast.

Robots of two different sizes were made. The larger robot was of length 110mm and diameter 30mm. In the case of the smaller robot, the corresponding dimensions were 45mm and 12mm. The motivation behind designing two robots was to examine the effect of scale on the locomotion capability of the robot. The chosen dimensions vary by one order of magnitude and hence their behaviour makes for an interesting study. In both the

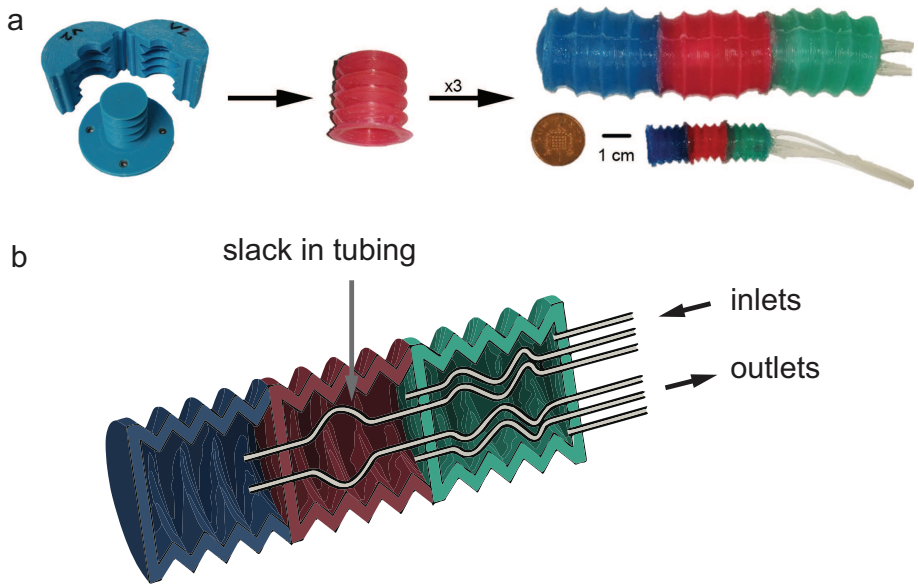

Figure 4.16: a. Fabrication of the soft robot. Left: 3D printed mould with two halves and a core used to cast the silicone elastomer. Middle: A single HEB actuator chamber. Right: three-segment robot fabricated at different scales. An English penny is shown for comparison. b. Cross sectional view of the robot showing the different chambers. Each chamber was supplied with an inlet and an outlet tube. Sufficient slack was provided in the tubes to allow for free expansion of the chambers.

cases, the HEB actuators incorporated a similar design with four folds and a half angle of 38.66°.

Each actuator was provided with a pair of silicone tubes to carry fluid to and from it. They had an outer diameter of 1mm and inner diameter of 0.8mm and were fed through to each chamber and affixed in place. Sufficient slack was provided in the tubing to allow the actuators to expand freely. A cross sectional view of the robot is shown in fig. 4.16b. A fluid pump (flow rate: 250ml/s) was used to move fluid in an out of each chamber and actuate the corresponding HEB actuator. These were external to the robot.

4.5.2 Autonomous Control

The aim with the robots was to operate them in a tank of fluid to study their locomotion and understand the progression of shapes. To achieve this, the HEB actuators on each robot had to be actuated in a specific sequence. To ensure consistency of the sequence and reduce experimental error the operation of the robots was made completely autonomous. A feedback-based approach was used to this end (fig. 4.17). Initial experiments relied on sensing the internal pressure of each actuator chamber to control its state of expansion. However, this proved to be challenging. The pressure sensors (Honeywell, ±15psi range), due to their size, could not be placed on the inside of the robot. They could also not be placed close to the body of the robot on the outside without drastically increasing the drag

on the surface. Therefore, they had to be located sufficiently far away and external to the robot. This required the use of long tubes, resulting in loss of pressure and inaccurate measurements at the sensor.

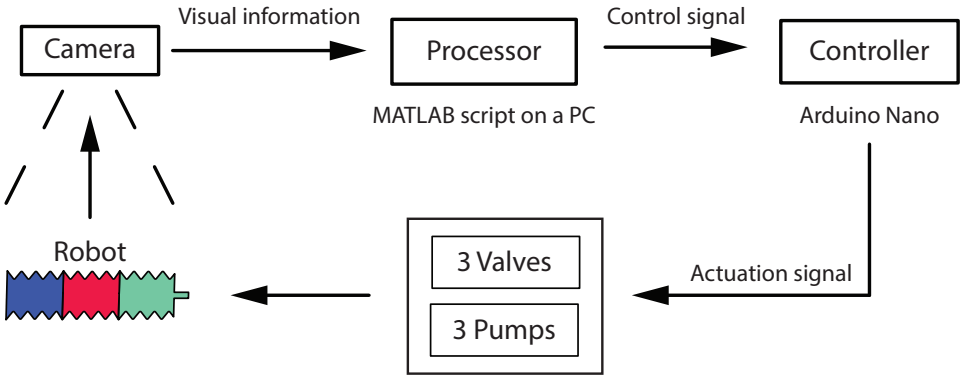

Figure 4.17: Schematic view of the control architecture of the robot [165]. A camera is used to determine the current state of the robot. A MATLAB script processes that information to determine the current state of the robot i.e., the expansion and contraction of each chamber. It then passes appropriate control signals to an Arduino which controls the operation of pumps and valves to direct the flow of fluid inside the robot.

To overcome the challenge of obtaining information regarding the state of the HEB actuators, a visual feedback system was incorporated. This negates the need to model the dynamics of the pump and the flow of fluid within the robot. A camera (Microsoft LifeCam HD-3000, 30fps) suspended above the tank recorded a video of the robot and transmitted a live image feed to a MATLAB script. This script identified the three chambers based on colour (blue, red or green) and estimated the size of the chamber in terms of the number of pixels of that colour in the image. This machine-vision estimate of chamber size was then relayed to the controller (Arduino Nano) which determined the flow of fluid within the chambers. The controller therefore had information regarding the state of expansion or contraction of each chamber, thus closing the feedback loop. This method proved to be more consistent than the remote measurement of pressure. It also did not require alterations to the robot other than a change in its colour.

4.5.3 Experimental Set-up

As discussed in chapter 2, the euglenoid movement may be classified as a low Reynolds number flow regime (estimated Re = 10^{-2} to 10^{-4} [68, 69]). To reproduce a similar environment, a solution of methyl cellulose (M0512, Sigma-Aldrich) in water was used for the robots to swim through. At a concentration of 1% w/w, this solution has a viscosity of 1000cP. This is a versatile substance and its viscosity can be tuned to suit the experiment by adjusting the concentration of the solution. A tank of dimensions 750mm $\times$ 210mm $\times$ 140mm was used to test the robots in. This was sufficiently large to maintain the robots in the centre of the tank and away from the walls to avoid effects arising from the boundary.

The approach of using a more viscous medium when working with larger scale experimental models has been shown to give insights into the dynamics of smaller physical systems such as insect wings [166]. This is the reason for the choice of the experimental medium which replicates the Reynolds number at the length and velocity scale of the robots. Scaling of physical properties in biological systems with the size and shape of organisms is also discussed in [167]. Water was chosen as the fluid of operation inside the robot to make it neutrally buoyant in the viscous medium.

The process of dissolving methyl cellulose powder in water is not straightforward. It is hydrophilic in nature and dissolves in cold water but not in hot water. However, when mixed directly with cold water, the powder does not dissolve thoroughly due to the formation of a gel layer around the particles, leading to their insufficient wetting. To ensure proper dissolution, it is necessary to ensure complete dispersal of the powder, which is best done in hot water. The steps to producing a solution of are described below.

- Step 1: Calculate the weight of methyl cellulose and the volume of water required to form a solution of the desired concentration and volume.
- Step 2: Take 1/3 of the volume of water and heat it up to 80°C.
- Step 3: Cool the remainder of the water to 0°C
- Step 4: Add the methyl cellulose to the hot water and disperse it to make sure that it is thoroughly wetted.
- Step 5: Once thoroughly dispersed, add the cold water to the mixture and vigorously mix the dispersion until all the methyl cellulose is dissolved. Continue mixing for at least half an hour to ensure that all of the solute is in the solution.
- Step 6: Allow the mixture to reach room temperature and let it stand still until all the air trapped inside has escaped.

When conducting the locomotion experiments, it was essential to make sure that there was negligible drag due to the tubes carrying fluid in and out of the robots and that their propulsion was only due to changes in shape of the body. The design choice to place the exit point of all the tubes at one end of the robot helped in this regard. The tubes were aligned parallel to the length of the robot. Their small diameter also helped reduce any hydrodynamic effects.

4.5.4 Locomotion Experiments

The robots were tested for their locomotion ability by placing them in the tank filled with the methyl cellulose solution. The fluid internal to the robot was moved from one chamber to the next, starting from the anterior end and moving towards the posterior, reproducing the motion of an expansion wave as is the case in euglenoids. This is the anterio-posterior

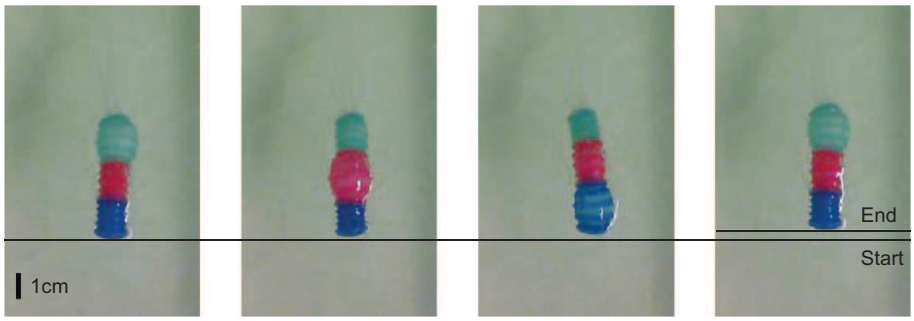

Figure 4.18: A sequence of images captured during one cycle of locomotion of the smaller robot. Scale bar = 1cm.

transfer of fluid mentioned earlier in section 2.3. When the last chamber expanded fully, the cycle was reset by moving the fluid directly to the foremost chamber, skipping the intermediate chamber. One cycle of locomotion in the smaller robot is shown in fig. 4.18. The internal area of the chamber is plotted for one of the trials in fig. 4.20b.

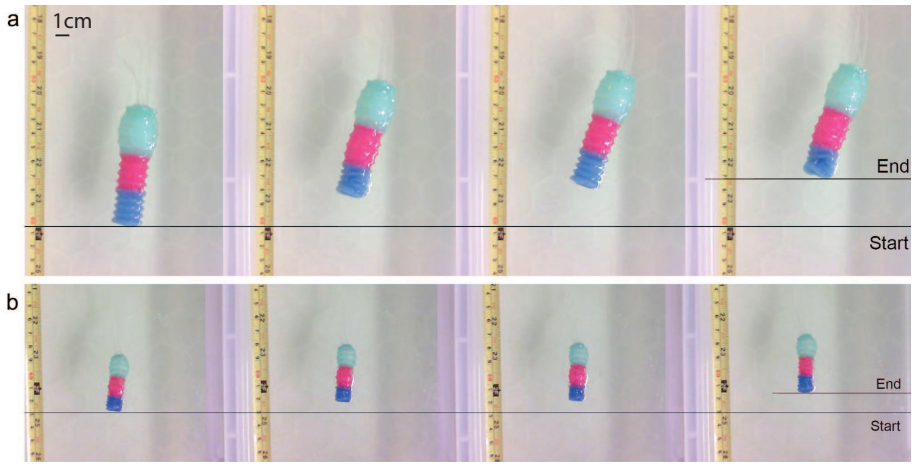

Figure 4.19: A sequence of three cycles of locomotion of the robot [165]; (a) larger version of the robot and (b) the smaller version. Scale bar = 1cm.

Euglenoids have been observed to both change in volume and maintain a fixed volume during euglenoid movement depending on their species. Exact values of volume change are not readily available due to the wide variety of observed shapes between different members of the family, but one study reported up to a 20% change in volume in one of the many cells studied [69]. The robots here, operated with a constant internal volume. They do however, possess the ability to operate with variable volume if desired. At the beginning of the cycle, the foremost chamber was inflated to a volume six times that of its resting state, while the other chambers remained contracted.

A sequence of images from the motion of the robots is shown in fig. 4.19. Three trials were run with each robot and the centroid was tracked as it moved. Figures 4.20 and 4.21 show the mean and standard deviation in the displacement of the centroid during three steps of locomotion. The smaller robot moved at an average velocity of 20mm/min (1/5

body lengths per cycle, 2.2 cycles/min). In case of the larger robot, the average velocity was 4.5mm/min (1/10 body lengths per cycle, 0.4 cycles/min). This is comparable to the estimated speed of swimming in a euglenoid, which is also 1/10 body lengths per cycle [69].

In fig. 4.19, a slight deviation for a straight line motion of the robot can be seen. This could be attributed to irregularity in fabrication. Though the behaviour of each chamber is very consistent (see section 4.4), a minor irregularity in the region joining two adjacent chambers can lead to a misalignment of the axis which causes the robot to exhibit a drift. This issue combined with the transient effect during the beginning of motion and non-linearity in material response contribute towards both the increase in uncertainty of position from one cycle to another and the dissimilarity in the magnitude of the increase between consecutive cycles. This problem could potentially be avoided by altering the method of fabrication. Each new chamber could be cast directly on top of the adjacent one instead of manually gluing them to reduce errors in fabrication.

Both the robots demonstrated the ability to swim by changing the shape of the body (fig. 4.19). The disparity in speed of the larger robot could be attributed to the volume of fluid being pumped between chambers of the robot. A pump with a larger flow rate could improve the average velocity. It is important to note that the distance travelled in each cycle would not change because of the low Reynolds number regime in which inertia has little effect (rate independence of Stokes equations, section 2.3.4). However, the cycle of motion would repeat in lesser time and thus increase average velocity. The characteristic lengths (taken to be the minimal lengths) for the smaller and larger robots are in the order of 10^{-3}m and 10^{-2}m respectively. Their velocities are in the order of 10^{-4}m/s and 10^{-5}m/s respectively. Viscosity of the medium is 1Pas. The resulting Reynolds numbers are of the order of 10^{-4} for both the sizes, which represents the flow regime of the euglenoids.

As explained in section 2.3, the euglenoid needs to develop a force against the water to propel itself forwards. The mass of the euglenoid is so negligibly small that if the force of propulsion vanishes, it is estimated that the drag due to water stops the motion of the cell within 1/8 of its body length [168]. Therefore, the euglenoid maintains a series of propulsions generated by cyclic changes in body shape. Additional aspects of the dynamic interaction between the body and the environment such as the motion that generates the most thrust and the flow of fluid around the body have not been studied. Having shown the hydrodynamic similarity between the robot and the organism in terms of the Reynolds numbers at both the sizes, the robots can now be used as a test platform to elicit new insights into euglenoid movement.

4.5.5 Analysis and Comparison of Shapes

The analysis of cell shapes during euglenoid movement was presented in chapter 3. This section applies the same method of analysis to the shapes of the robots and compares them

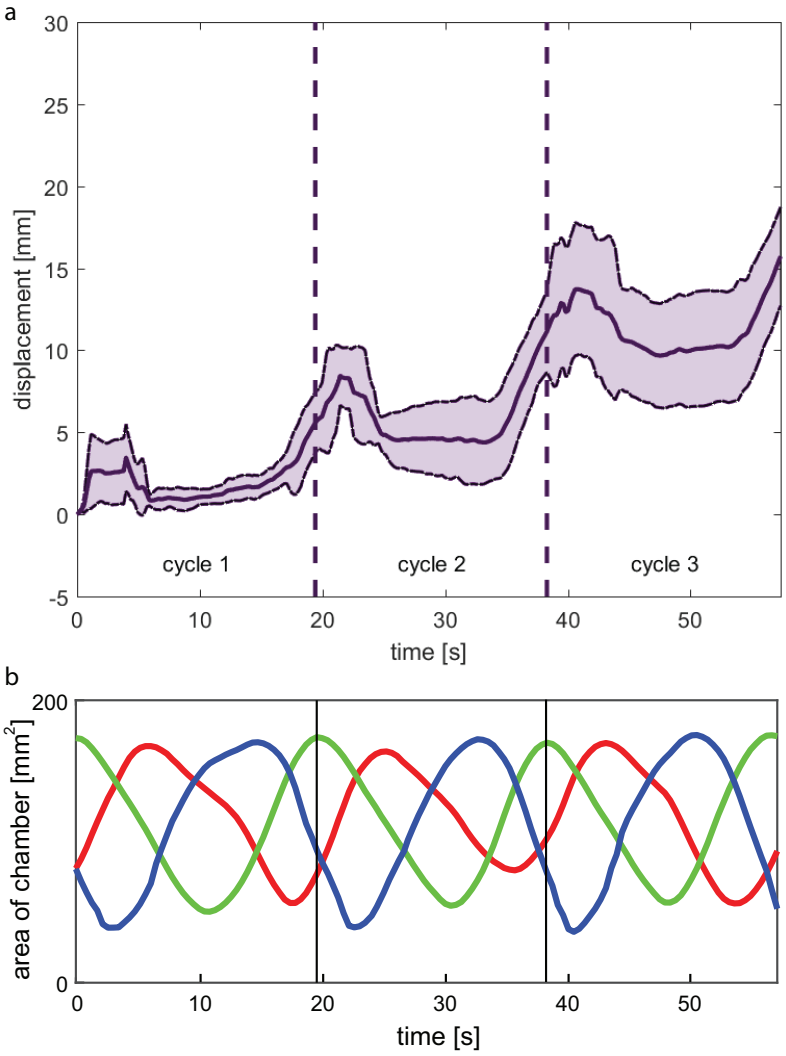

Figure 4.20: (a) Displacement of the centroid of the smaller robot during three cycles of motion. The solid line represents mean of three trials and the dotted line is one standard deviation away from the mean. (b) The change in area of individual chambers (smoothed with a moving average filter with window span of 15 points) during one of the trials is shown below, each curve corresponding to the chamber of the same colour [165].

with those of the euglenoids. Firstly, a qualitative comparison of shapes is shown in fig. 4.22. Outlines of the cell during euglenoid movement (fig. 1.1) are shown for comparison. Inflating and deflating chambers of the robot enables it to replicate many of the shapes displayed by the euglenoid.

For a quantitative analysis, videos of the robots in locomotion were analysed in the manner described in sections 3.1 and 3.2. The eigenvalues are shown in fig. 4.23. Those for the euglenoid are also shown for comparison. In the case of the smaller robot, the first three eigenvectors capture a cumulative variance of 86.9% and in the case of the larger robot, 88.3%. Scores on the first five principal components are shown in fig. 4.24 for the

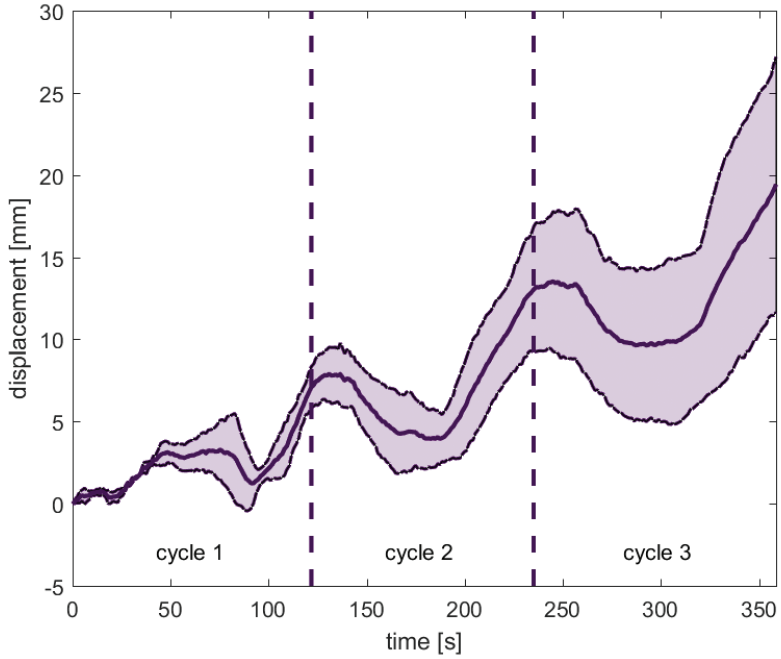

Figure 4.21: Displacement of the centroid of the larger robot during three cycles of motion [165]. The solid line represents mean of three trials and the dotted line is one standard deviation away from the mean.

smaller robot during one cycle of locomotion. Figure 4.25 shows the change in shapes of smaller robot as the scores on the first three principal components are varied. The corresponding figures for the case of the larger robot are shown in fig. 4.26 and 4.27. In this case, three cycles are shown in which the periodic nature of movement can be clearly observed.

In the case of both the robots, the first principal component represents the position of the widest portion of the robot along the length. In other words, this component describes the shifting of mass from one end to the other. The second component in case of the smaller robot and the third component for the larger robot describe an hour glass shape as the score increases and its inversion when the score decreases. The other component describes a subtler feature of the shape.

To compare the shapes with those of the euglenoids, the method of looking at the statistical variance in shape described in section 3.2 was used. First, videos of one cycle of locomotion were taken from the robots and the euglenoid. They were then sampled to have the same number of frames (46 shapes in each case). Fourier coefficients up to six harmonics were computed for each shape.

The coefficients were then reduced to three principal components. The variance captured by these components was computed by using coefficients from one sample and eigenvectors from another sample (table 4.1). The higher the variance, the better the ability to capture details of shape. It can be seen that the first principal component of the large

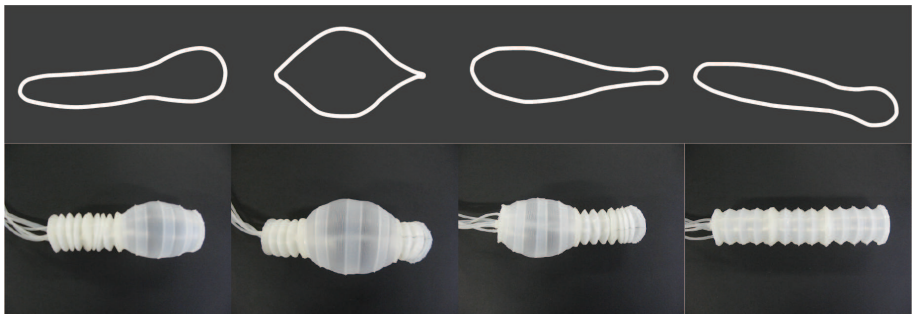

Figure 4.22: Top: outlines of cell shapes from fig. 1.1 during euglenoid movement. Bottom: the soft robot illustrating euglenoid shapes. Note that in this specific demonstration, the volume is not constant [165].

Table 4.1: Variance in shape captured by principal components

Coefficients $[D]$	Eigenvectors $[X]$	normalised variance of first three principal components $[DX]$
Euglenoid	Large robot	78.78%, 5.96%, 15.26%
Large Robot	Euglenoid	9.3%, 84.95%, 5.75%
Euglenoid	Small robot	30.33%, 14.33%, 5.53%
Small Robot	Euglenoid	28.74%, 55.19%, 24.26%

robot, which corresponds to anterior-posterior mass transfer, captures 78.78% of the variance in euglenoid cell shape. The second principal component of the euglenoid, again corresponding to shifting of mass, captures 84.95% of the variance in shape in the larger robot. The corresponding numbers for the smaller robot and the euglenoid are 30.33% and 55.19%.

Based on these values, shapes of the euglenoid were reconstructed using the first principal component describing robot shapes. Similarly, shapes of the robot were reconstructed using the second principal component describing euglenoid shapes. These are shown in fig. 4.29 and 4.28.

A key feature of euglenoid movement is the transport of internal mass from one end of the body to the other. This is observed in the diversity of shapes. The comparative analysis of shapes shows that the principal components capture this variation to a high degree and that the robots achieve these drastic changes in shape. Based on analysis of shape alone, this observation suggests that the robots will be able to achieve euglenoid-like locomotion given a suitable medium (which has already been proven in section 4.5.4), provided the dynamic shape change closely matches that of the euglenoids, not just the quasi-static representations in fig. 4.29 and 4.28. This is indeed the case, as seen from the shapes of the robot and the principal components. This highlights the usefulness of the mathematical analysis as the prediction of movement did not require a fluid dynamics model of the euglenoid.

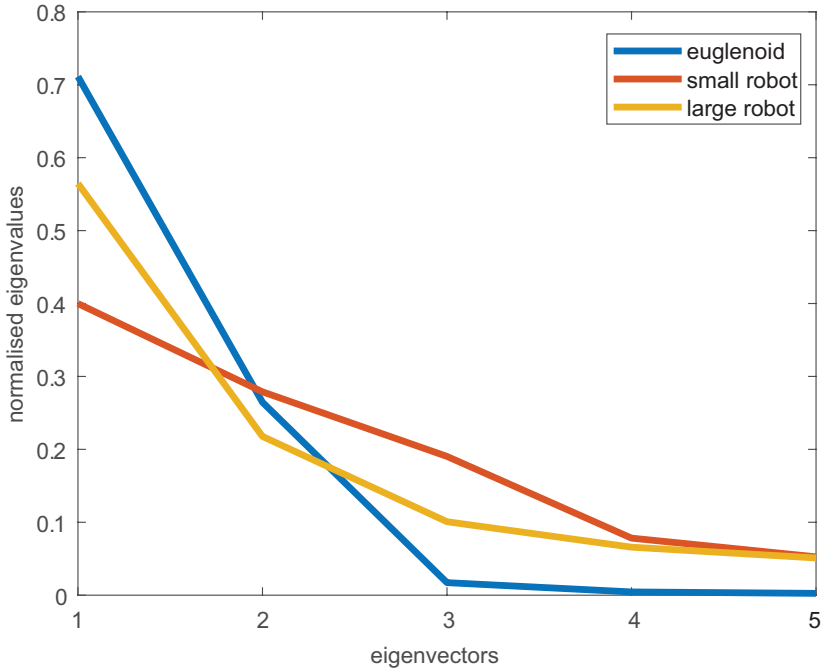

Figure 4.23: Normalised eigenvalues of the first five eigenvectors describing the shape [165].

The presence of the state of axial expansion prior to ballooning in the HEB contributes towards similarity in dynamic shape transition with the euglenoids. As mentioned earlier, a slender extension of the body in the direction of motion is observed in the organisms prior to the appearance of a large bulge at the anterior. The robot is capable of exhibiting a similar extension because of the axially extending state of the HEB. This would not have been possible if it were to be constructed out of simple ballooning chambers.

From the plot of eigenvalues in fig. 3.4 it can be seen that the shape of the euglenoid is distinctly characterised by the first three principal components whereas in the case of the robots, the variance is spread across more components. This might suggest that extreme shapes as seen in the euglenoids are not fully reproduced in the robots. The reconstructed shapes in fig. 4.28 and 4.29 support this claim. On the other hand, based on the similarity in locomotion, it can be argued that such extreme shapes might not be necessary for propulsion as long as a sufficiently large wave of expansion travels along the length of the body.

An interesting question to address would be the reason for the existence of extreme shapes in euglenoids. It is possible that the organism actively tries to achieve such shapes to sustain its motion. On the other hand, it could be a consequence of the strip-like mechanism and the constraints on its construction. The approach of using a robot in studying the effect of changes in body shape is appropriate to address this question because of the ease of generating shapes in a controllable manner. In this context, a quantitative method of comparing shapes is particularly useful.

In case of the euglenoids, efficiency of swimming using euglenoid movement is estimated

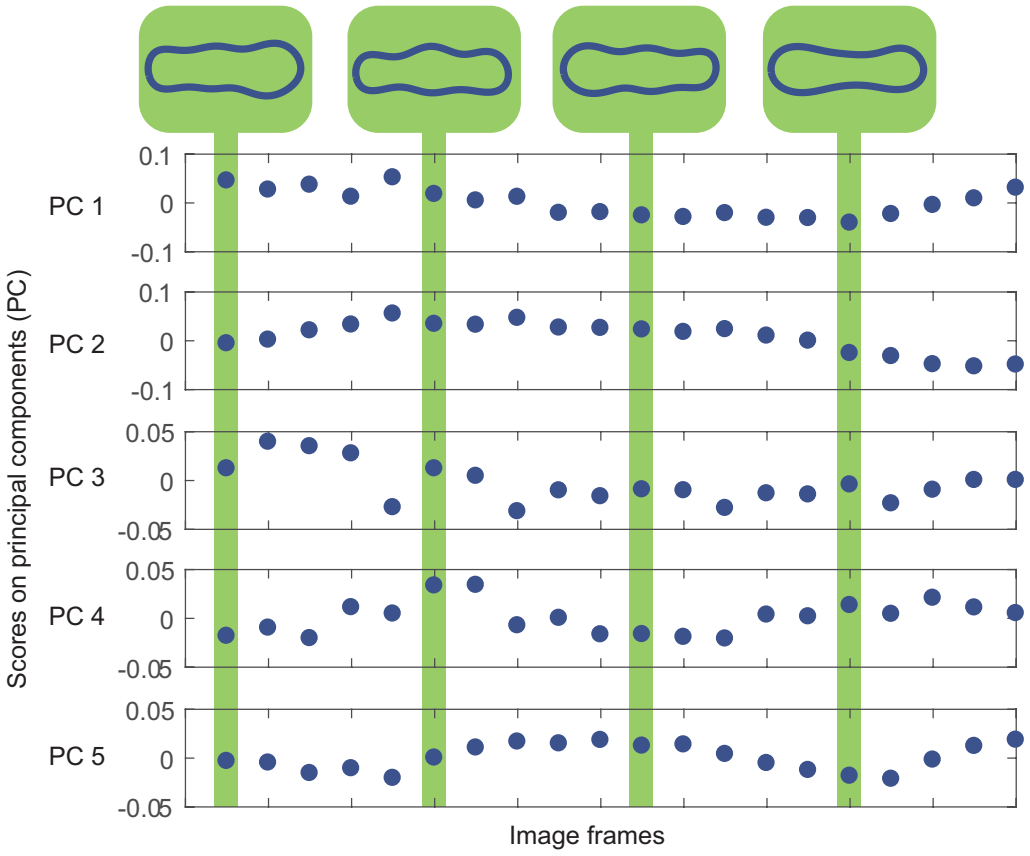

Figure 4.24: Change in scores on principal components describing the shape of the smaller robot during one cycle of locomotion. Reconstructed shapes are shown above for the scores indicated in the plots, using only the first 5 principal components [165].

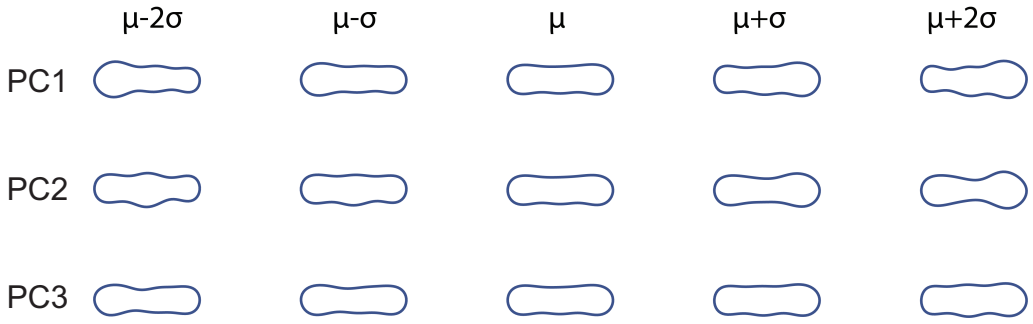

Figure 4.25: Effect of change in scores of each principal component on the estimated shape of the smaller robot. Each row corresponds to change in score of one principal component. The central column represents the mean shape. On either side, are one and two units of standard deviation away from the mean [165].

to be around 1% [69]. This low efficiency could in part be due to the aforementioned presence of extreme shapes. Efficiency of the robots has not been investigated here. There is scope for investigating this in a future work. This would shed light on whether it is possible for the euglenoids to move with greater efficiencies while making use of less extreme shapes.

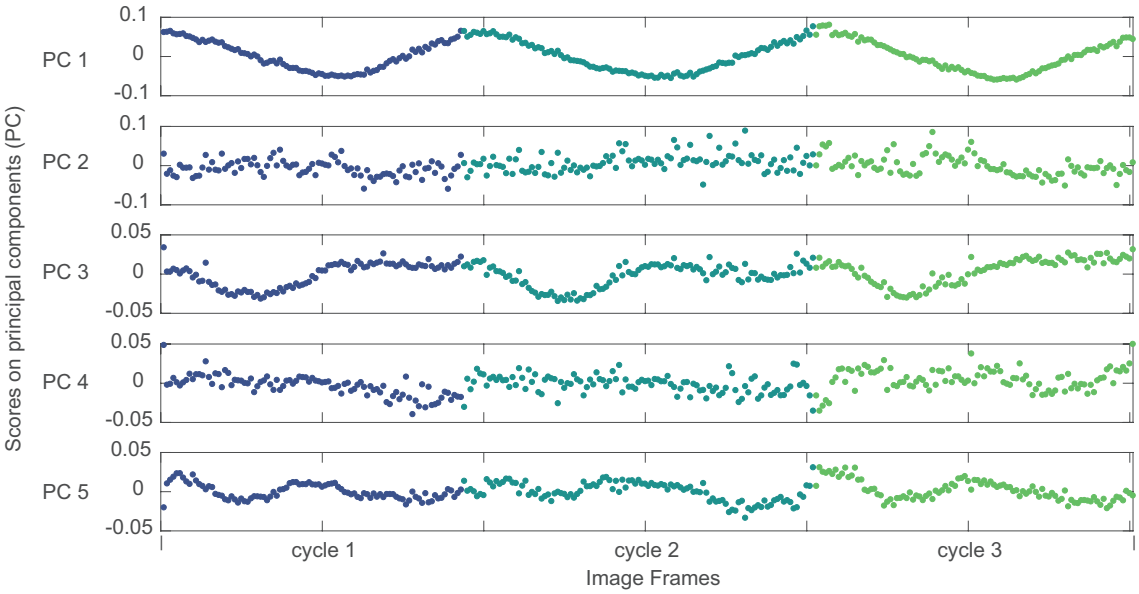

Figure 4.26: Change in scores on principal components describing the shape of the larger robot during three cycles of locomotion [165].

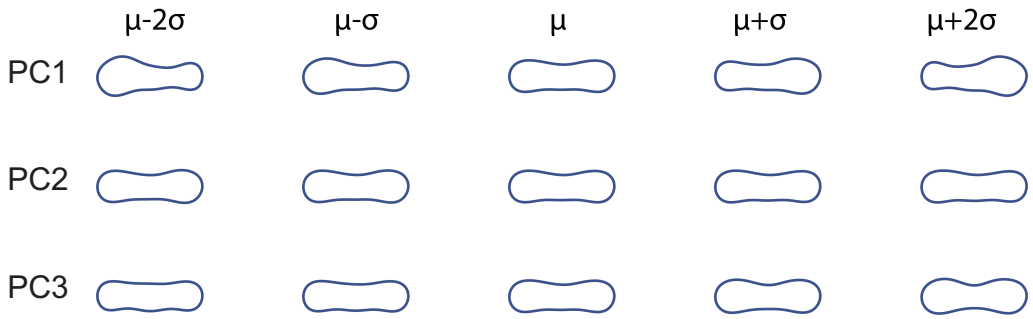

Figure 4.27: Effect of change in scores of each principal component on the estimated shape of the larger robot. Each row corresponds to change in score of one principal component. The central column represents the mean shape. On either side, are one and two units of standard deviation away from the mean [165].

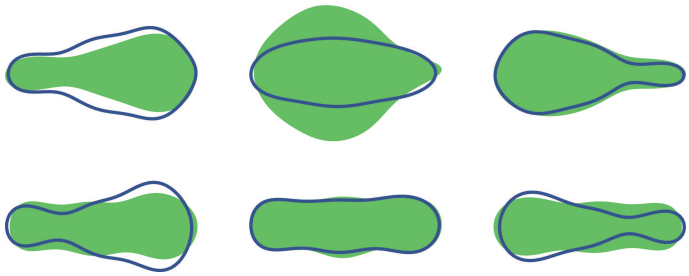

Figure 4.28: Comparison of shapes between euglenoid and the smaller robot at three different instances during one cycle of locomotion. Top row: Shaded region indicates the true shape of the euglenoid. The outline in blue is the shape estimated using the scores on the first principal component from the shape of the smaller robot. Bottom row: Shaded region indicates the true shape of the smaller robot. The outline in blue is the shape estimated using the scores on the second principal component from the shape of the euglenoid [165].

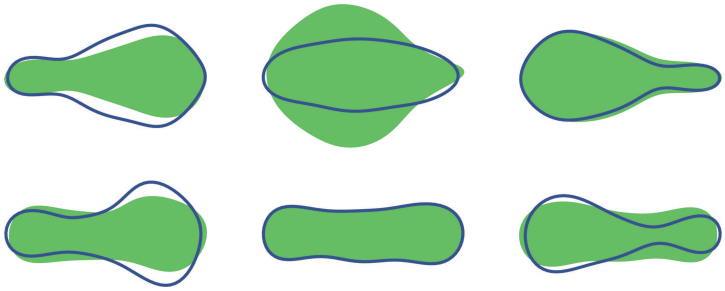

Figure 4.29: Comparison of shapes between euglenoid and the larger robot at three different instances during one cycle of locomotion. Top row: Shaded region indicates the true shape of the euglenoid. The outline in blue is the shape estimated using the scores on the first principal component from the shape of the larger robot. Bottom row: Shaded region indicates the true shape of the larger robot. The outline in blue is the shape estimated using the scores on the second principal component from the shape of the euglenoid [165].

A second difference between the robots and the organism is that transition of fluid from one chamber to another in the robot does not produce a smooth transition in the shape of the contour. The boundary wall that separates two chambers, though elastic, locally restricts the expansion of the chambers to a certain extent. This difference partially explains the inability of the robot to assume more extreme shapes. Given a sufficiently large number of chambers, the transition in shape could be made smoother. Based on eigenvalues of fig. 3.4, and the variances shown in table 4.1, it can be seen that the larger robot reproduces shapes closer to the euglenoid than the smaller one. A possible reason for this difference could be the change in angular stiffness of the folds due to scaling. The difference in shape between extremes due to expansion and contraction of folds is less pronounced at smaller scales. Parameters such as angle of folds, their number and density could be optimised to achieve better replication of shape.

4.5.6 Multi-modal Locomotion

Unlike the organism, the robot is not restricted to working in a fluidic environment and in addition to replicating euglenoid movement, the soft robot presented here is capable of multi modal locomotion and locomotion outside liquid environments. Compliance of the structure is demonstrated in fig. 4.30a. Figure 4.30b shows the robot moving on a flat table and fig. 4.30c shows the robot climbing a pipe with an inchworm gait, using a non constant volume of operation. Therefore, the robot can also be used to test and compare different locomotion strategies.

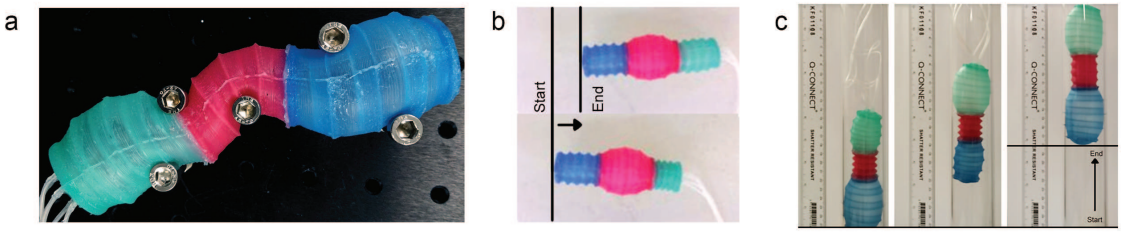

Figure 4.30: a. Demonstration of compliance of the robot in a static test. b. Sequence of images at the start and end of one cycle of dynamic locomotion of the robot on a flat table. c. Robot climbing inside a pipe using an inch-worm type gait [165].

4.6 Discussion

Taking inspiration from the shapes of euglenoids, a novel solution for achieving multi-modal actuation and large volumetric change in biomimetic soft robotics has been presented. This was achieved by designing a custom pneumatic bellows-like actuator with soft elastomer materials that exhibits four distinct states, depending on internal pressure. A key novelty of the HEBs design is that the actuator both extends and contracts axially and can, in a high pressure state, balloon out radially. The actuator was characterised and its behaviour at different pressures was analysed.

To demonstrate the potential of the versatile HEB actuator and suitability for euglenoid-like biomimetic soft robots, three-segment robots (EuMoBots) were fabricated. These robots showed the capability to swim with shape change. In addition, they are capable of locomotion in non fluid environments. The soft and compliant nature of the robot could be exploited for operating in constrained spaces.

The quantitative method of comparison based on elliptic Fourier descriptors was used to show similarity in shapes of the organism and the robot. The method of comparison presented here could potentially be used for other soft robotic systems where accurate models of shape do not exist. Hydrodynamic similarity between the robot and the organism was established. The robot can therefore be used as a tool to study the dynamics of locomotion in euglenoids and possibly other organisms, thereby contributing back to the understanding of biology.

There is scope for investigating the efficiency of locomotion and changes in design and control required to improve their performance. The effect of parameters such as the frequency, amplitude and phase of actuating pressures in individual chambers on the locomotion could be yet another interesting avenue for research. Control of the robot through shape matching, using the Fourier descriptors, is also possible because of the vision based feedback system that was implemented to drive the robot.

The extremity of shapes exhibited by the robot is limited by the ultimate tensile strength of the material used for fabrication. Even though each chamber of the robot is unconstrained during operation, as internal pressure increases, the actuator can eventually fail due to rupture of the membrane. This limitation is primarily due to the monolithic skin design. Alternative fabrication techniques such as 3D printing and soft lithography [169] could partially address limitations of the elasticity of the material. On the other hand, euglenoids do not suffer from this limitation, because they employ a different mechanism of achieving change in shape, namely sliding of pellicles. Unlike the robot, between two extreme shapes, there is negligible strain in the pellicle strips as they do not change in length but only slide against each other. This allows the euglenoid to transition between shapes without rupturing its cell membrane. This demonstrates a fundamental challenge in achieving giant shape change in robotics; to exceed the mechanical limits of the material requires multi-element structures with moving parts. This is the topic of the next chapter.

Another limitation of the current design is the inability of the robot to change direction. Ability to steer could be added to the current design by adding mechanisms to orient chambers in the desired direction. Using actuated coils of shape memory alloy [170] or using constraints on the material [171] are two of several possible solutions. Sources of power, actuation and control could be placed within the body of the robot [105], eliminating the need for a tether and thus reducing the size of the robot.

Chapter 5

Pellicular morphing for soft robots

The work described in this chapter has been published as

- **Digumarti KM**, Conn AT, Rossiter J. Pellicular Morphing Surfaces for Soft Robots. *IEEE Robotics and Automation Letters*. 2019 July;4(3):2304-9.

In the previous chapter, we presented the design of EuMoBot, a soft robot capable of swimming like and reproducing the shapes seen in euglenoids. It relied on folding, extension and ballooning of soft cylindrical bellows (HEBs) to change shape. In this chapter, the focus is on replicating the fundamental mechanism that drives shape change in euglenoids, namely the sliding of strips in the pellicle.

We first revisit the microstructure of the pellicle. This is followed by a kinematic model of the pellicle that helps guide the design of bio-inspired artificial strips. The design, fabrication, characterisation and actuation of the strips is presented next. An application in the context of soft robotics is also discussed by demonstrating a shape morphing surface.

5.1 Pellicle Structure in Euglenoids

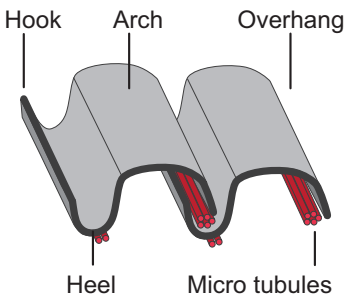

Figure 5.1: Illustration showing the four main structural components of a pellicular strip: arch, heel, hook and overhang. [172] © 2019 IEEE

The structure of the pellicle in euglenoids and its movement has been extensively studied [17, 50, 54, 62, 63, 64, 65, 69, 173] and was described in chapter 2. The main features are briefly restated here for context. The width of the strips in pellicle has been determined to be 0.1µm - 0.25µm [174]. Their cross section (fig. 5.1) consists of four key elements: an arch, a heel, a hook and an overhang. The hook of one strip interlocks with the overhang of its neighbouring strip. The sliding of strips is achieved by molecular motors in the micro-tubules that are present in the region of overlap. Several shapes for the cross section have been observed [65], but we focus on the S-shaped structure (fig. 5.5).

5.2 Kinematic Model of Pellicular Sliding

Kinematics of sliding within the pellicle have been studied in [69]. The model is briefly recounted here and later used in section 5.3 to build a MATLAB tool with the aim of aiding in the design of artificial pellicular strips and morphing surfaces. The primary assumption in the model is that the deformation in shape is due to simple shear between adjacent strips. In other words, the strips remain parallel to each other and maintain a constant distance as they slide against each other. Since the strips are assumed to be inextensible, the total surface area (S) of the cell also remains constant. The sliding can therefore be described as an in-plane, equi-area shear [175].

Consider the two configurations of the cell shown in fig. 5.2(b and c). Let fig. 5.2b be the reference configuration and fig. 5.2c be the deformed configuration. To describe points on the surface of the cell in each of the configuration, a set of two parameters is defined. The first of these is the body coordinate $\lambda \in [0,1]$. To understand its definition, imagine a plane with its normal along the long axis of the cell, cutting the surface into two parts. The body coordinate is the ratio of the surface area delimited by the plane (s) to the total surface area (S). This is shown pictorially in fig. 5.2a. The second parameter is the azimuth angle about the long axis $\theta \in [0,2\pi]$. Together, λ and θ parameterise the surface.

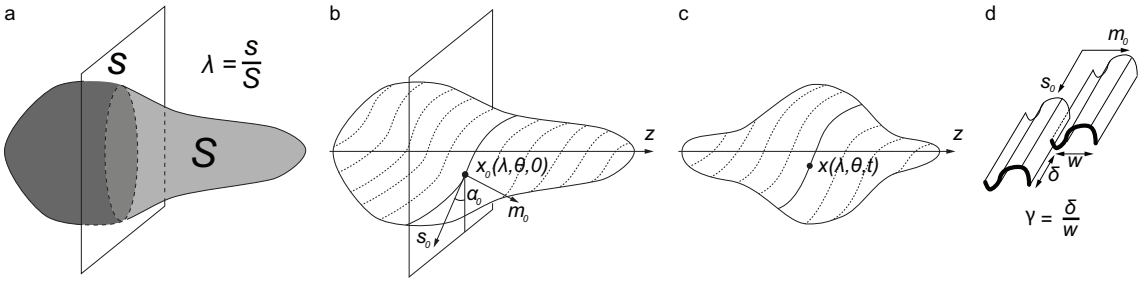

Figure 5.2: (a) Illustration showing the definition of the body coordinate λ. (b) Reference configuration of the pellicle. (c) Deformed configuration of the pellicle. (d) Definition of strain γ.

Assuming both the configurations to be axisymmetric, the surfaces can be described in terms of generating curves $\{r_0(\lambda), z_0(\lambda)\}$ and $\{r(\lambda,t), z(\lambda,t)\}$ in the reference and deformed cases respectively. The problem being solved is to find the local shear strain in the strips $\gamma(\lambda,t)$ (defined as the ratio of local displacement to the width of the strips, fig. 5.2d), given these generating curves. The approach followed in [69], solves this problem by comparing the Caucy-Green deformation tensor computed from the given configurations with that constructed from the definition of simple shear. A simplified formulation is presented here, with a more detailed derivation of each quantity in Appendix A.

Points on the surface of the cell in the reference configuration, $\mathbf{x}_0$ and in the deformed configuration $\mathbf{x}$ can be written in Cartesian coordinates as

$$\mathbf{x}_0(\lambda,\theta,0) = \begin{Bmatrix} r_0(\lambda)\cos\theta \\ r_0(\lambda)\sin\theta \\ z_0(\lambda) \end{Bmatrix} \quad , \quad \mathbf{x}(\lambda,\theta,t) = \begin{Bmatrix} r(\lambda,t)\cos(\theta+\psi(\lambda,t)) \\ r(\lambda,t)\sin(\theta+\psi(\lambda,t)) \\ z(\lambda,t) \end{Bmatrix}, \tag{5.1}$$

where $\psi(\lambda,t)$ is an unknown displacement in the azimutal direction. Partial derivatives of the coordinates with respect to parameters λ and θ can be written as

$$\mathbf{x}_{0_\lambda} = \frac{\partial \mathbf{x_0}}{\partial \lambda} = \begin{Bmatrix} r_{0_\lambda}\cos\theta \\ r_{0_\lambda}\sin\theta \\ z_{0_\lambda} \end{Bmatrix} \quad , \quad \mathbf{x}_{0_\theta} = \frac{\partial \mathbf{x_0}}{\partial \theta} = \begin{Bmatrix} -r_0\sin\theta \\ r_0\cos\theta \\ 0 \end{Bmatrix} \tag{5.2}$$

$$\mathbf{x}_\lambda = \frac{\partial \mathbf{x}}{\partial \lambda} = \begin{Bmatrix} r_\lambda\cos(\theta+\psi) - r\psi_\lambda\sin(\theta+\psi) \\ r_\lambda\sin(\theta+\psi) + r\psi_\lambda\cos(\theta+\psi) \\ z_\lambda \end{Bmatrix} \quad , \quad \mathbf{x}_\theta = \frac{\partial \mathbf{x}}{\partial \theta} = \begin{Bmatrix} -r\sin(\theta+\psi) \\ r\cos(\theta+\psi) \\ 0 \end{Bmatrix}$$

where, $r_{0_\lambda} = \dfrac{\partial r_0(\lambda)}{\partial \lambda}$, $z_{0_\lambda} = \dfrac{\partial z_0(\lambda)}{\partial \lambda}$, $r_\lambda = \dfrac{\partial r(\lambda,t)}{\partial \lambda}$, $\psi_\lambda = \dfrac{\partial \psi(\lambda,t)}{\partial \lambda}$ and $z_\lambda = \dfrac{\partial z(\lambda,t)}{\partial \lambda}$.

Since the surface is axisymmetric, the local geometry does not depend on azimuthal position. Therefore, without loss of generality, the conditions $\theta = 0$ and $\theta + \psi = 0$ may be used to simplify the expressions in the two configurations respectively. With the additional definitions $a_0 = \sqrt{r_{0_\lambda}^2 + z_{0_\lambda}^2}$ and $a = \sqrt{r_\lambda^2 + z_\lambda^2}$, these can be written as

$$\mathbf{x}_{0_\lambda} = \begin{Bmatrix} r_{0_\lambda} \\ 0 \\ z_{0_\lambda} \end{Bmatrix} = a_0\hat{e}_{0_\lambda} \quad , \quad \mathbf{x}_{0_\theta} = \begin{Bmatrix} 0 \\ r_0 \\ 0 \end{Bmatrix} = r_0\hat{e}_{0_\theta} \quad , \quad \mathbf{x}_\lambda = \begin{Bmatrix} r_\lambda \\ r\psi_\lambda \\ z_\lambda \end{Bmatrix} \quad , \quad \mathbf{x}_\theta = \begin{Bmatrix} 0 \\ r \\ 0 \end{Bmatrix}, \tag{5.3}$$

The metric tensor, $\mathbf{g}$, is the product of tangent vectors and is given as

$$\begin{aligned}\mathbf{g} &= \begin{bmatrix} \mathbf{x}_\lambda \cdot \mathbf{x}_\lambda & \mathbf{x}_\lambda \cdot \mathbf{x}_\theta \\ \mathbf{x}_\lambda \cdot \mathbf{x}_\theta & \mathbf{x}_\theta \cdot \mathbf{x}_\theta \end{bmatrix} \\ &= \begin{bmatrix} r_\lambda^2 + r^2\psi_\lambda^2 + z_\lambda^2 & r_\lambda^2\psi_\lambda \\ r_\lambda^2\psi_\lambda & r^2 \end{bmatrix} \\ &= \begin{bmatrix} a^2 + r^2\psi_\lambda^2 & r^2\psi_\lambda \\ r^2\psi_\lambda & r^2 \end{bmatrix}\end{aligned} \tag{5.4}$$

Simple shear happens along the direction of the strips ($\mathbf{s_0}$ in fig. 5.2d) and occurs in the $\mathbf{s_0} - \mathbf{m_0}$ plane. Therefore, the deformation gradient can be given as

$$\mathbf{F} = \mathrm{R}\left(\mathrm{I} + \gamma\left(\mathbf{s_0} \otimes \mathbf{m_0}\right)\right), \tag{5.5}$$

where R is an undetermined rotation and I is the identity matrix. To eliminate R, the right Cauchy-Green deformation tensor $\mathbf{C} = \mathbf{F}^\top\mathbf{F}$ is used, which can be expressed as

$$\mathbf{C} = \begin{bmatrix} 1 - \gamma\sin 2\alpha_0 + \gamma^2\cos\alpha_0 & -\gamma\cos 2\alpha_0 - \gamma^2\sin\alpha_0\cos\alpha_0 \\ -\gamma\cos 2\alpha_0 - \gamma^2\sin\alpha_0\cos\alpha_0 & 1 + \gamma\sin 2\alpha_0 + \gamma^2\sin^2\alpha_0 \end{bmatrix} \tag{5.6}$$

The components of $\mathbf{g}$ are also those of the Cauchy-Green deformation tensor expressed in the natural basis of the reference configuration (by definition of the tensors). Using equations 5.4 and 5.6, results in the following three relations.

$$\frac{a^2 + r^2\psi_\lambda^2}{a_0^2} = 1 - \gamma\sin 2\alpha_0 + \gamma^2\cos^2\alpha_0 \tag{5.7}$$

$$\frac{r^2 + \psi_\lambda}{r_0 a_0} = -\gamma\cos 2\alpha_0 - \gamma^2\sin\alpha_0\cos\alpha_0 \tag{5.8}$$

$$\frac{r^2}{r_0^2} = 1 + \gamma\sin 2\alpha_0 + \gamma^2\sin^2\alpha_0 \tag{5.9}$$

Given r_0 and r, these equations can be solved for γ and ψ. γ is a solution to the quadratic equation

$$\left(\sin^2\alpha_0\right)\gamma^2 + \left(\sin 2\alpha_0\right)\gamma + \left(1 - \frac{r^2}{r_0^2}\right) = 0, \tag{5.10}$$

which results in

$$\gamma = \frac{-\cos\alpha_0 \pm \sqrt{\cos^2\alpha_0 - \left(1 - \frac{r^2}{r_0^2}\right)}}{\sin\alpha_0} \tag{5.11}$$

For a real solution to exist, the discriminant must be non-negative. This results in the constraint $\frac{r}{r_0} \geq \ \mid \sin\alpha_0 \mid$. Combining equations 5.7 and 5.8, the following relation is obtained

$$\frac{r^2}{a_0 r_0}\psi_\lambda = \frac{\cos\alpha_0}{\sin\alpha_0}\left(1 - \frac{r^2}{r_0^2}\right) + \gamma, \tag{5.12}$$

which can be integrated to find ψ.

It is to be noted that r_0 and z_0 are not independent but are related through the constant surface area assumption. Similarly, r and z are also related. This relation is explained in Appendix A.

5.3 Design Tool for Artificial Pellicles

Using the model presented above, we developed a MATLAB tool to aid in the choice of actuator mechanism for the soft robot. The reference configuration is assumed to be cylindrical with the strips oriented along the axis (i.e. $\alpha_0 = \pi/2$). Under this assumption, the constraint on the radius simplifies to $r(\lambda, t) \geq r_0(\lambda, 0) \quad \forall t$. The user is free to specify the initial radius (r_0) and the length of the initial cylinder. The number of strips on the surface may also be specified. In addition, the user can lay out the shape of the deformed configuration ($r(\lambda, t)$). This input is provided through a graphical user interface where the curve forming the surface of revolution can be manipulated (fig. 5.3a).

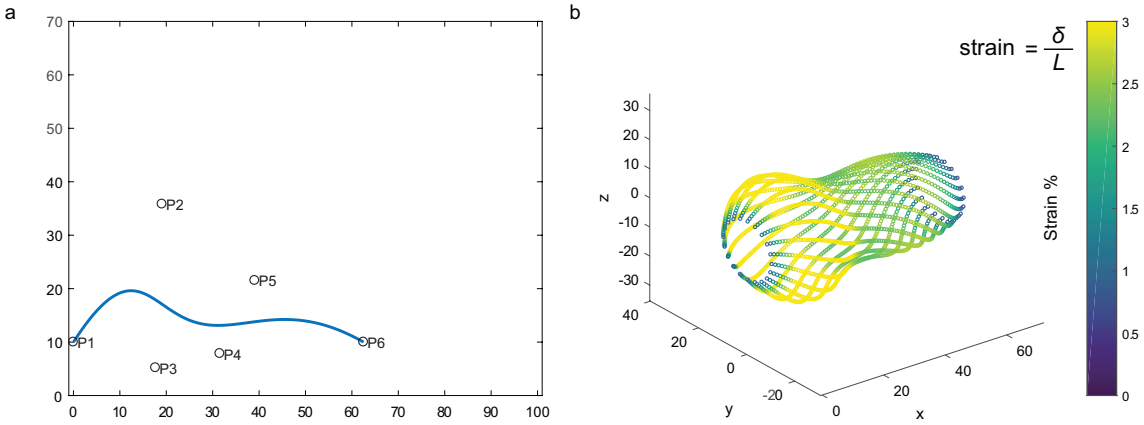

Figure 5.3: (a) Input from the user specifying the generating curve in the deformed configuration using control points P1-P6. (b) Output of the design tool showing the curved pellicular strips and the local strain percent.

A Bezier curve was used to represent the generating curve. Starting with a minimum of two points representing the ends, any additional number of points can be added to, or removed from the control polygon. They can also be moved around to create undulating shapes, as long as the constraint on the radius is satisfied. Furthermore, for every change made to the generating curve, the position of the last control point (i.e. one end point of the curve; P6 in fig. 5.3a) is automatically updated to ensure that the constant surface area condition is met. This provides an intuitive, visually guided design experience in specifying the shape of the deformed configuration.

The output of the design tool is a representation of the strips in the deformed configuration (fig. 5.3b). Information regarding the local strain percentage (displacement, δ, over length expressed as a percentage) is overlaid on top of the strips using colour. This

provides a visual indication of the regions of higher strain within a given deformed shape. It also allows for comparison of strains between various deformed shapes.

Using this tool, the shapes of the euglenoid were reconstructed by manually moving control points to make the input Bezier curve resemble the cell outlines from fig. 1.1. The shear is estimated to be a maximum of 8% of the length of the strip in the extreme case (fig. 5.4), which makes it a very attractive candidate for bio-inspiration. It should be noted that our interest is in generating local shear at a specific region on the strip, which would require an actuator capable of producing much larger strain per unit length (≈25-30%). This observation helps in the choice of an appropriate soft robotic actuator technology that could be used to generate sliding.

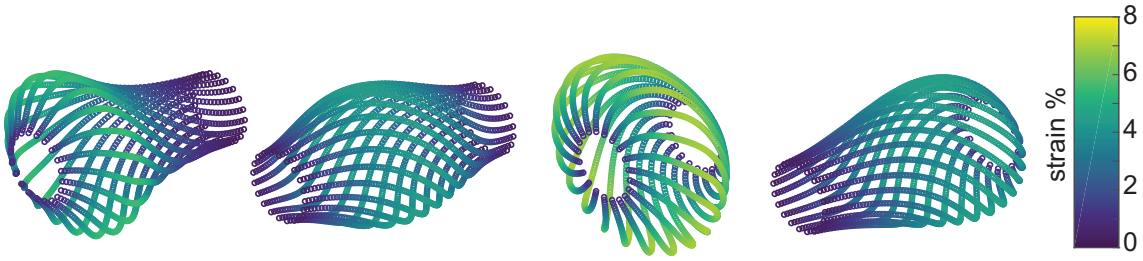

Figure 5.4: Shear between strips for various input shapes. [172] © 2019 IEEE

5.4 Review of Actuator Technologies

In chapter 2, some of the soft actuator technologies were presented which are commonly used to substitute for the muscle-like actuation found in animals. In the context of reproducing the strains discussed above, a few prominent methods are reviewed here.

Ionic polymer metal composites (IPMCs) have been used to construct multi-segmented artificial cilia [176]. These actuators could be used between the strips to mimic the motion of comb like structures found in the euglenoid pellicle [65], thus enabling sliding. However, the small forces produced, make them less appealing at the scale required. Ultrasonic motors have been fabricated by bonding polymers to piezoelectric materials [177] and could drive motion between the strips. Another approach could be to generate movement through the use of travelling waves, such as through soft, active materials like dielectric elastomers [178].

In a recent study [118], we investigated a combination of dielectric elastomer actuators and electroadhesive grippers as a means of generating controllable motion between two surfaces. The study resulted in a crawling robot capable of moving in multiple directions (see Appendix C). An inchworm-like movement was generated by using the elastomer actuator to move the body, while the electroadhesive regions held parts of the body in place. A similar mechanism could be used to generate localised displacement in the strips. However, incorporating the actuation and adhesion mechanism at the small scale of the

strips is a challenge.

Other actuators that exploit electrostatic polarisation of liquids have been developed which deliver extremely large strains ($\approx 99\%$) and large force densities [179, 180]. These actuators are light in weight and easy to manufacture at a low cost. However, their performance at small scales has not been evaluated. The requirement for high operating voltages limits the applicability of the robot. Alternative muscle-like materials have been proposed that rely on evaporation of a low melting point liquid within a silicone matrix to achieve actuation when heated [181]. Once again, scaling down the actuator could be difficult.

In this work, we use coiled shape memory alloy actuators [107] to achieve relative motion between adjacent strips of custom-designed and fabricated soft polymer. These actuators have been shown to generate the large strains that are suitable for the task. In addition, they can conform to the changing shape of the strips such that the force is more or less directed along the length of the strips even in a deformed configuration. Exploiting these benefits and the relative ease of control of these actuators, we present the design, fabrication and actuation of bio-inspired pellicle strips and use them in a soft robot module that is able to actively deform its surface.

The novelty of our design and advantage over traditional tendon driven continuum robots is that the actuation is localised. This enables a more continuous deformation of the structure and thus a much wider range of robot deformations. In addition, we show novelty in the replication of a microscopic structure at the centimetre scale while retaining its functionality.

5.5 Bio-inspired Polymer Strips

The structure of the strips in the euglenoid pellicle is unique and an off the shelf engineering equivalent is not readily available. This motivated the fabrication of custom polymer strips [172]. The bio-inspired flexible strips used in this study were fabricated by extruding thermoplastic polyurethane (Desmopan 2786A [182]) in a filament extruder (Noztek Pro, fig. 5.6). A custom die was fabricated using wire electrical discharge machining (wire EDM), giving the S-shaped cross-section with a material thickness of 0.5mm throughout (fig. 5.5).

The Noztek Pro filament extruder has an $L/\Delta D$ ratio of 100:1. It has two heating bands, one covering the barrel and the other covering the melt chamber. It was necessary to carefully control the temperature of the extruder to ensure a uniform cross section over the length of the filament. The process of extrusion is described below.

- Step 1: Dehumidify the material (obtained as pellets of approximately 5mm diameter) in an oven at 80°C for at least 2 hours.
- Step 2: Preheat the melt chamber to 190°C, let it stabilise and maintain the tem-

perature for 15min.

- Step 3: Introduce the material into the hopper and begin the process of extrusion.
- Step 4: Reduce the temperature to 145°C in decrements of 5°C, allowing the temperature to stabilize each time.
- Step 5: At 145°, extrude the required amount of material.
- Step 6: Cut the material into strips of the required length using a surgical scalpel

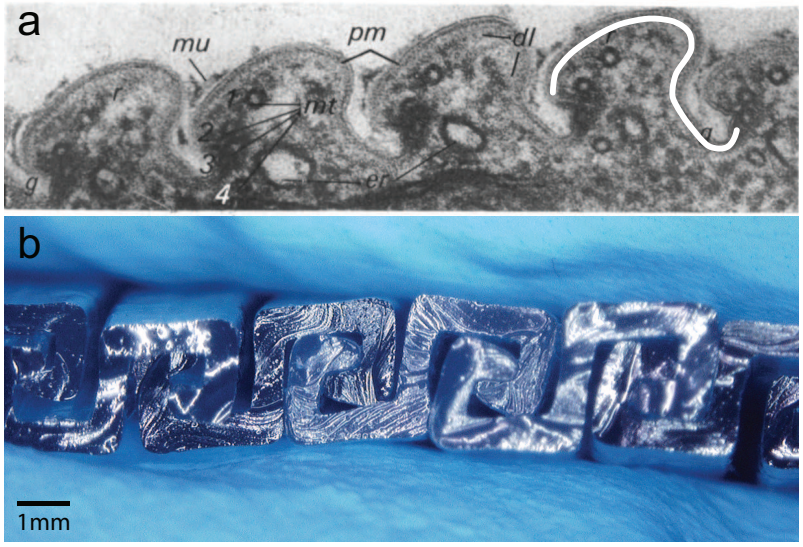

Figure 5.5: (a) Cross section of the pellicle in *Euglena gracilis*. Rreproduced with permission from [183]. One of the strips has been highlighted in white. (b) Microscopic image of the cross section of our bio-inspired polyurethane strips. [172] © 2019 IEEE

Figure 5.5 shows the resulting strips of polymer, interlocked to create a stable pellicle-like sheet. The customised cross section ensures that the strips stay within a fixed distance of each other. They are however free to slide along the length of the strip.

It is essential to dehumidify the material prior to extrusion. Any moisture content leads to bubbles of water vapour due to evaporation at the temperature of extrusion. These may either be trapped within the polymer or leave voids on the surface. This results in defects such as an uneven cross-section of the strip (fig. 5.7a)

Consistent results were obtained at 145°C. However, directly extruding at this temperature resulted in a barrel jam and torsional fracture in the auger screw. This is because the material is not fluid enough. Therefore, preheating and reducing the temperature slowly (Steps 2-4) was essential. However, care must be taken to not raise the temperature too high. At temperatures of 180°C - 200°C, the material is fluid, collapses immediately upon exiting the nozzle and does not hold its shape.

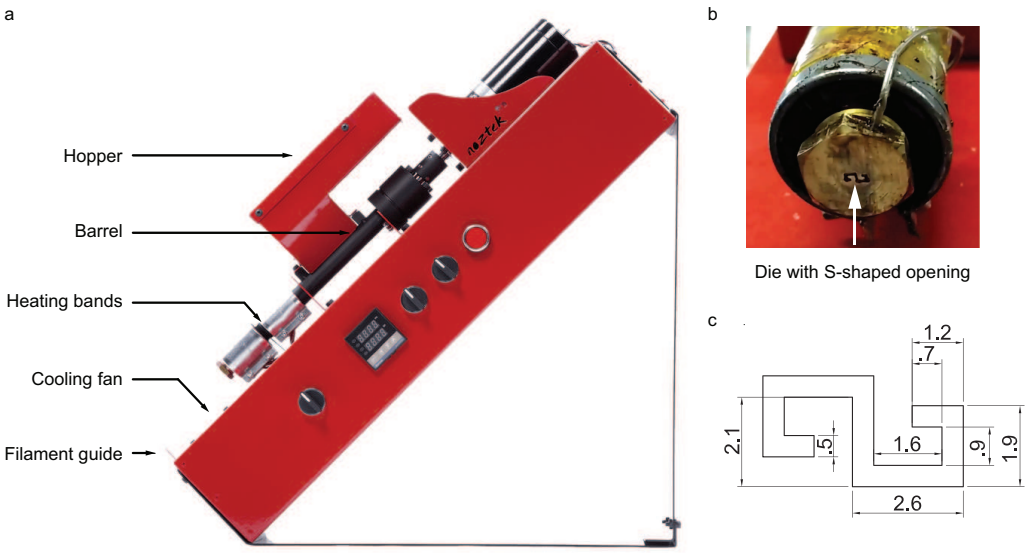

Figure 5.6: (a) The Noztek Pro filament extruder used to manufacture the bio-inspired strips. Relevant parts have been labelled. Image has been adapted from www.noztek.com. (b) The custom die with S-shaped cross section. (c) Dimensions in mm of the cross-section of the bio-inspired strips.

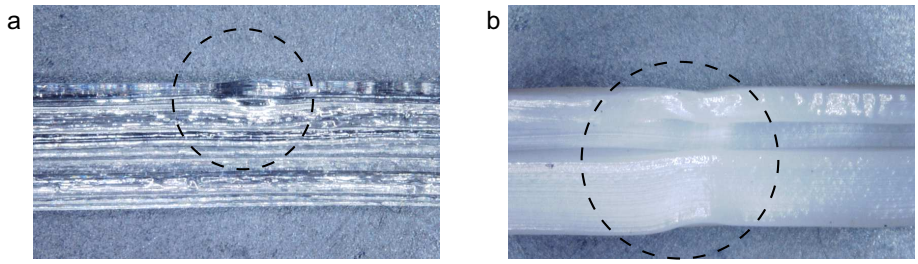

Figure 5.7: Images of extruded polymer strips, under a microscope, showing common defects during fabrication. (a) Defect caused by the presence of moisture in the material leading to a trapped bubble during extrusion. (b) Inconsistent cross section due to variation in drawing force.

Circulating cold air was used to cool the strips as they exited the nozzle. In addition to the fan built into the equipment, two external fans were used to blow air from either side. This increased the circulation of colder air around the tip of the nozzle and helped with cooling the material quickly.

In addition to controlling the temperature, a uniform drawing force needs to be maintained to obtain a consistent cross-section and smooth surface finish. Uneven surface or alterations to the cross-section (fig. 5.7b) result in higher friction and prevent easy sliding of the strips. The extruder was placed on an elevated surface inside a fume cupboard at a height of about 1m and at an angle of 45° with the horizontal. The strips exiting the

nozzle were allowed to fall naturally under the effect of gravity. A spooler was not used to aid in drawing out the material. As sufficient material was extruded, the weight of the material between the tip of the nozzle and the ground reached a near constant and ensured a stable and uniform drawing force. The resulting strips when locked together (fig. 5.5b), had low sliding friction and moved across each other freely. When required, a drop of silicone oil was used to provide extra lubrication.

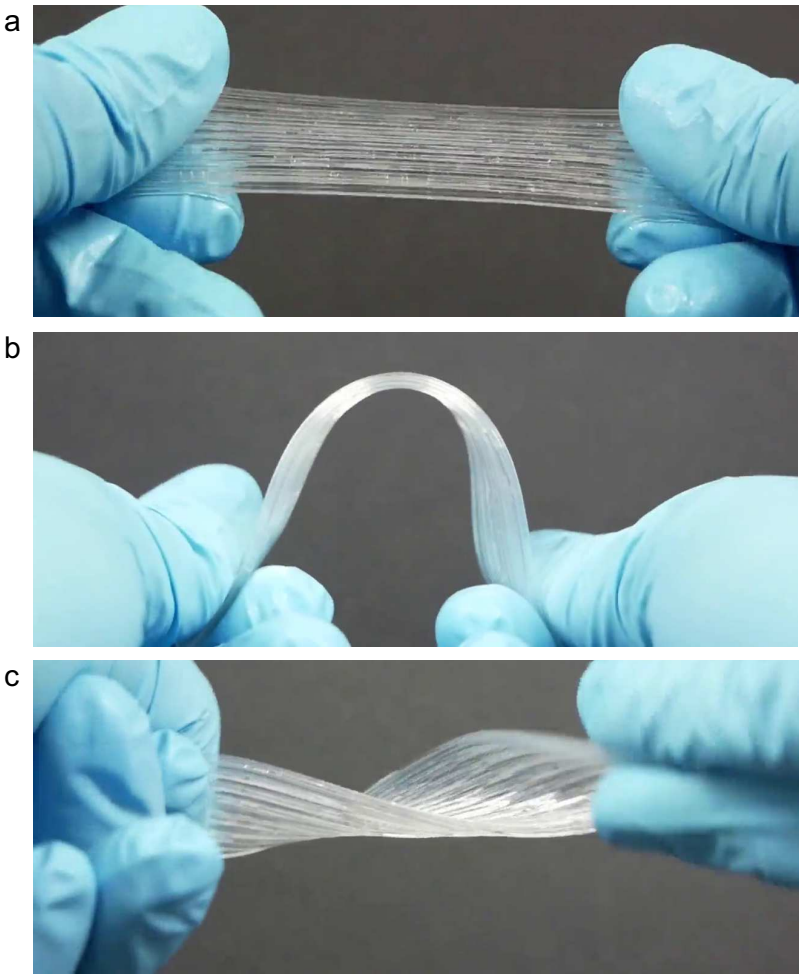

Figure 5.8: (a) A sheet of interlocked strips. (b) Bending of the sheet about an axis perpendicular to their length. (c) Twisting of the sheet around an axis along their length

Unlike 3D printable plastics such as PLA (polylactic acid) and ABS (Acrylonitrile butadiene styrene) which lack flexibility (elasticity modulus, E $\sim$ 1GPa), the chosen thermoplastic polyurethane can deform into the required twisted shape (fig. 5.4) while being rigid enough to hold the new shape (E $\sim$ 1MPa). Elastomers commonly used in soft robots such as silicones (DragonSkin, Ecoflex, etc.) are too flexible and readily deform (E $\sim$ 0.01MPa). Ease of extrusion at the small scale was another reason for its choice.

The elasticity of the polyurethane can be easily tuned using additives. The particular material chosen in this thesis is readily compatible with PLA, in addition to other poly-

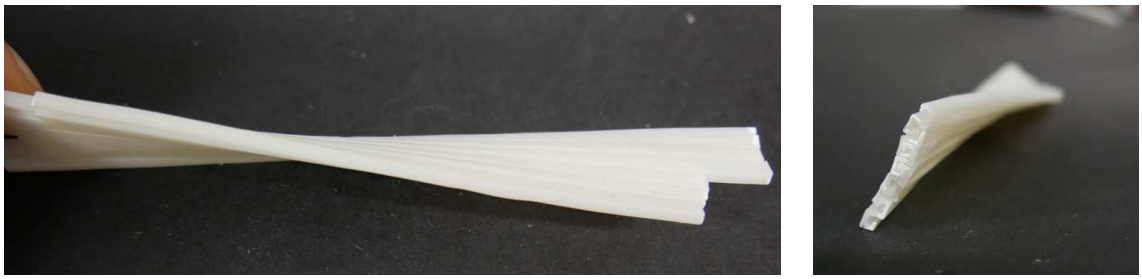

Figure 5.9: A sheet of pellicle strips with a pre-induced twist. These were fabricated in PLA.

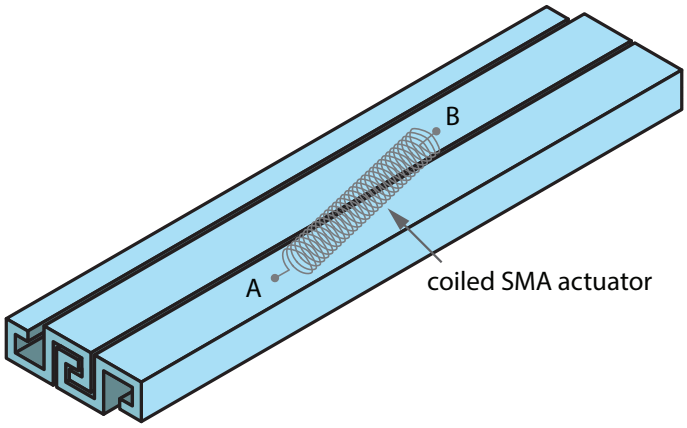

Figure 5.10: Illustration of coiled SMA actuator placement on a pair of interlocked polymer strips.

mers. Blends of the material were successfully fabricated at ratios of 20%, 50% and 70% (weight of PLA in the mixture). As the proportion of PLA increased, the stiffness of the extruded strips increased. These were however, not used in the study but proved that blending of materials was indeed possible. The characterisation of these polymeric blends in terms of mechanical properties was not undertaken.

A flexible sheet can be formed by interlocking multiple strips. The resultant sheet can bend and twist about both planar axes. This is shown in fig. 5.8. Closed cylindrical structures can also be constructed by bringing the strips at the ends of a sheet together and interlocking them in place.

The strips used in the characterisation experiments of the subsequent sections are all straight extrusions. However, a twist can also be induced in the strip while it is being extruded by applying a moment to it as it cools after exiting the nozzle. An example of a sheet made with such strips is shown in fig. 5.9. In this manner, structures with diverse configurations can be constructed.

Actuated strips were fabricated by attaching coiled shape memory alloy (SMA) wire (BMX150, Toki Corporation, contraction of 200% of length) at two points on a pair of interlocked strips. Each end of the actuator is on a different strip (A and B in fig. 5.10).

5.6 Principle of Operation

As discussed in the beginning of this chapter, the deformation of the euglenoid cell is due to localised sliding between pellicle strips. This behaviour is easy to comprehend when the shape of an interlocked pair of actuated polymeric strips is observed (fig. 5.11).

The length of each strip is constant and since the strips do not separate from each other (fig. 5.5b), so is the distance between them. A local shear is generated by contraction in length of the coiled SMA actuator that connects to points on either strip (A and B in fig. 5.11). In a constraint free case, the contraction of the actuator results in the sliding of one strip relative to the other (fig. 5.11a). When the strips are fixed to each other at one end (using adhesive) and left free at the other end, shortening of the SMA actuator results in a C-shaped curving the strips (fig. 5.11b). Sliding is observed only at the free end. When both ends are fixed, the strips take on an S-shape upon actuation (fig. 5.11c). Multiple actuated strips connected to each other can thus create a complex shape-morphing surface.

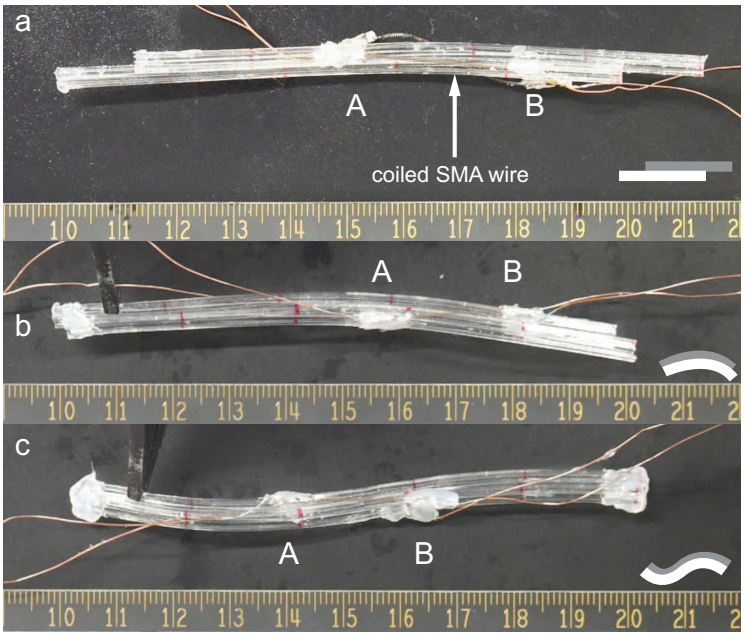

Figure 5.11: Three distinct behaviours observed in two pellicle strips based on constraints imposed upon the ends. (a) With no end constraints, the strips slide against each other. (b) When one end is fixed, the strips bend to form a C-shape. Sliding is observed at the free end. (c) When both ends are fixed, an S-shaped curve is observed.

5.7 Characterisation - Measurement of Separating Force

Three sets of experiments were conducted to measure the force required to separate a pair of interlocked strips. Half strips of length 3cm were affixed to plastic attachments using high-strength epoxy adhesive (RS, Components UK, 159-3957). These acted as the clamps

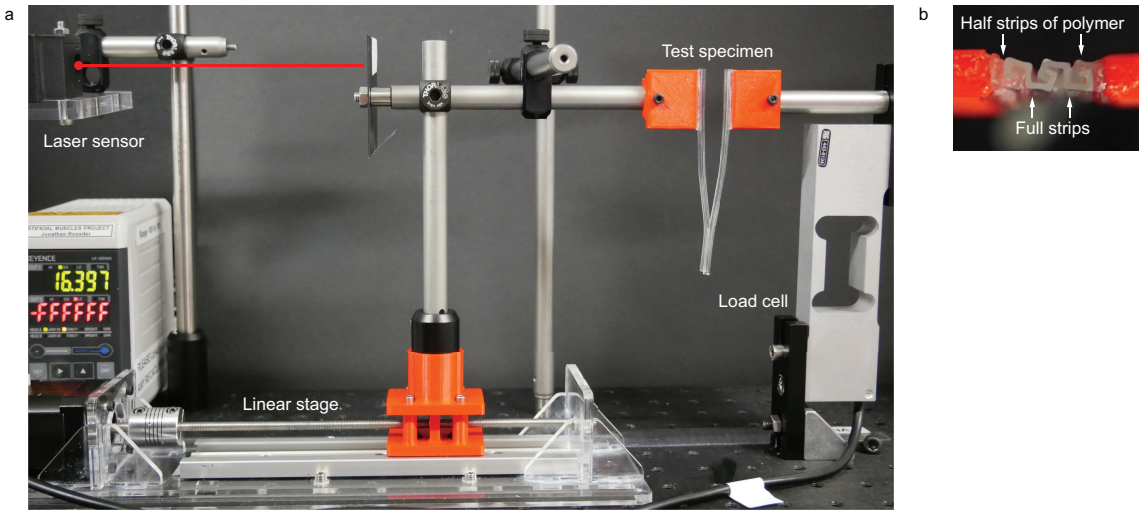

Figure 5.12: (a) Experimental setup used to measure the force of separation in the bio-inspired artificial pelliclular strips. (b) A close-up view showing the strips being held in the clamps. [172] © 2019 IEEE

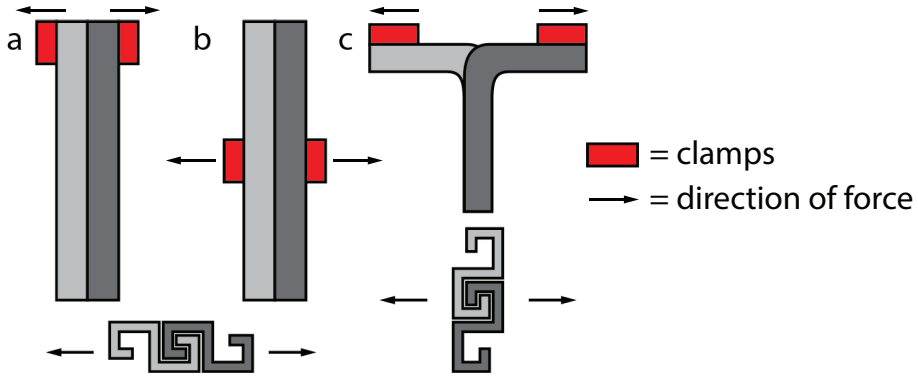

Figure 5.13: The three types of peeling tests that were performed on a pair of interlocked strips. (a) End separation. (b) Mid-point Separation. (c) T-peel.

that pulled the strips apart (fig. 5.12). Two interlocked strips of length 10cm each were held in the clamps with glue. In the first experiment, the strips were held at the end while in the second, they were held in the middle (fig. 5.13a and b respectively). The direction of loading is in the plane of the strips and perpendicular to the direction of sliding. This represents a component that contributes to the circumferential load on the strips of a euglenoid. The third experiment was set up in a manner loosely based on the T-peel test as defined in the ASTM-F88 standard. The two interlocked strips were peeled at one end and bent at 90 degrees (fig. 5.13c). They were then affixed to clamps. The peeled ends were pulled apart and the force required to peel was measured. This experiment replicates the case of radial load in the euglenoids.

In all the experiments, the clamps were pulled apart using a linear stage at a constant

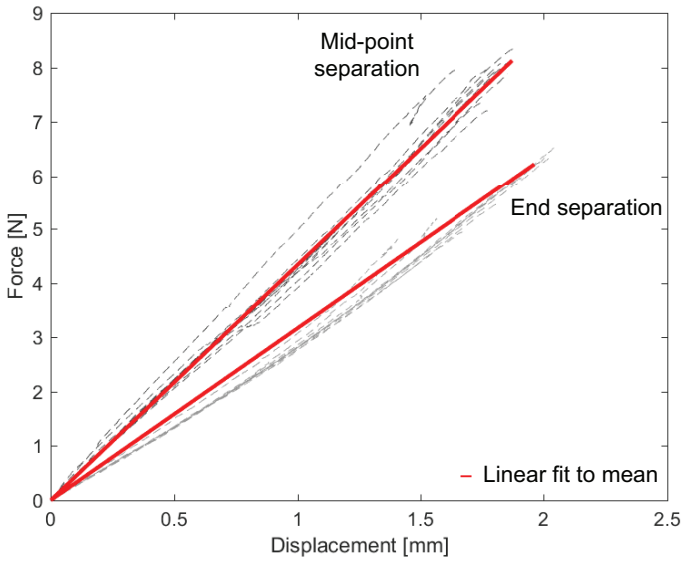

Figure 5.14: Force to separate interlocked strips when peeled from the end (fig. 5.13a) and the middle (fig. 5.13b). The dotted lines indicate recorded data. The solid line is a linear fit to the mean. [172] © 2019 IEEE

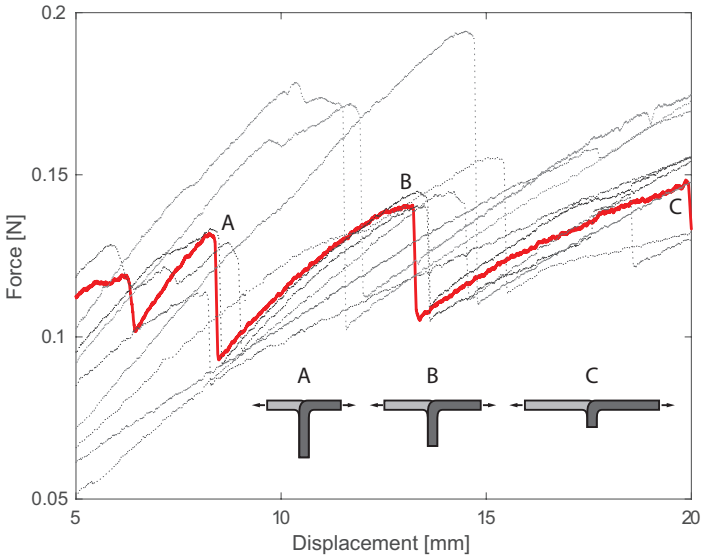

Figure 5.15: Force to separate interlocked strips in the T-peel test (fig. 5.13c). The dotted lines indicate recorded data. The solid line highlights data from one of the experiments. Each peak (A, B, C) corresponds to the instance when separation occurred locally but the strips held together further down the length (illustrations A, B, C). [172] © 2019 IEEE

rate (0.45 mm/s). Force was measured using a load cell. Displacement of one of the clamps was measured using a laser displacement sensor (LK-G152 and LKGD500, Keyence). Both force and displacement readings were recorded (USB-6001, National instruments) at a frequency of 1000Hz. Each experiment was repeated 10 times with the same specimen.

The force required to separate a pair of interlocked strips along a direction perpendicular to the length of the strips and in the plane of the strips is shown in fig. 5.14. In the case of peeling at the end (fig. 5.13a), separation happened at a force of 5.6±0.8N whereas in the case of peeling from the middle (fig. 5.13b), the force of separation was 7.9±0.4N. The solid line in fig. 5.14 is a linear fit to the mean force at each displacement point. The maximum error in fit was 0.0672N and 0.1057N respectively. The slightly larger force in the case of peeling from the middle could be attributed to distribution of force over a comparatively larger area and boundary effects around the region of peeling. The difference in free-edge effects as opposed to bulk peeling are illustrated by this disparity in force.

The force of separation for the case of T-peel (fig. 5.13c) is shown in fig. 5.15. It was observed that the strips do not separate continuously but in stages of easy separation (force drop) followed by resistance to parting (force rise) in what can be described as a 'stick-slip' manner. On the onset of peeling, the strips separate partially but are held together at points further down the length (see illustrations A, B and C in fig. 5.15). As seen from the highlighted data, the force curve shows multiple peaks, each of which corresponds to instances at which stiction was overcome at these points and local separation occurred. The force of separation in this case is 0.14±0.02N (mean of all peaks). The variation in data between experiments could be attributed to minor imperfections on the surface of the test specimen. Since the strips are bent at a right angle during the T-peel, there is deformation of the cross section, which also contributes to variation in force. This could also explain the changing period of 'sticking' with increasing displacement. An experimental measurement of fictional force could help understand the onset of the 'stick-slip' behaviour. In practice, the strips undergo bending and twisting. Therefore, the characterisation of frictional force would have to take into account these conditions as well.

5.8 FEA of Peeling

A 2D finite element analysis of the peeling of strips was performed in addition to the experiments to predict potential regions of failure for a given cross section. One half of the S-shaped cross section was modelled in ANSYS. The two strips were defined as individual bodies that interlock with each other but do not touch initially. One of the strips was fixed while a displacement was applied to the other in the direction that causes them to separate. The contact regions between the bodies were modelled as frictionless and without lubrication. A relatively more refined mesh was used in the regions of contact. The material model was based on tensile test data (DIN 53504) from the manufacturer's

datasheet. Distribution of stress across the cross section shows that the points of likely failure are the internal corners (regions marked in fig. 5.16). The deformed shape closely resembles that which was observed during experiments (fig. 5.17c). A similar analysis can be considered for other cross sections such as a C-shaped to compare maximum stress and predict regions of material failure.

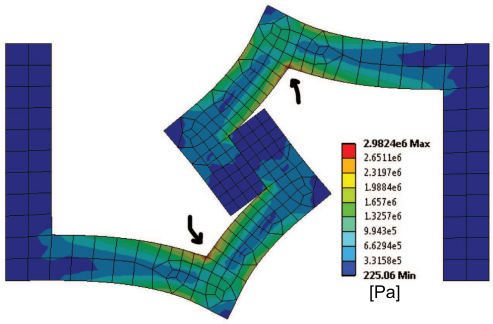

Figure 5.16: Equivalent (von-Mises) stress in the strips as predicted in a finite element analysis of separation of interlocked strips. The analysis predicts material failure at the internal corners (marked with arrows). [172] © 2019 IEEE

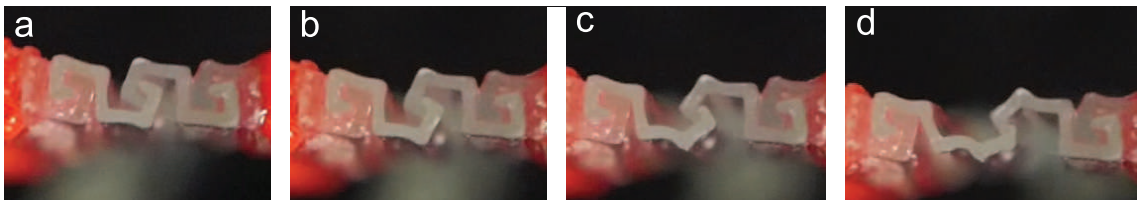

Figure 5.17: Various instances during the separation of interlocked strips when peeling happened at the ends. (a) Initial contact. (b-c) Intermediate instances. (d) Instance prior to separation. [172] © 2019 IEEE

5.9 Shape Exploration

As described in section 5.6, the shape of the actuated strips varies with the type of constraints imposed at the ends. To investigate this behaviour, shear strain was applied to a pair of interlocked strips at different locations, of different magnitudes and under the two constraints: fixed-free and fixed-fixed (fig. 5.18c, d respectively). The amount of strain was varied by changing the length of the SMA actuator used (20mm, 30mm and 40mm prior to actuation, 250mA current). Two actuators were used on either side of the pair of strips. This was done to ensure negligible out-of-plane deformation. Both the actuators were aligned in the same direction. An antagonistic arrangement was not necessary as the inherent elasticity of the material of the strips, restored the shape to the initial configuration upon deactivation of the actuator. The location of actuation was varied by changing

the points at which the actuators were affixed to each of the strips. In all, 10 different configurations were explored (fig. 5.18).

In the cases with a fixed-free constraint imposed on the strips, upon applying a shear strain, the curve took on a C-shape. The curvature of the curve has only one local extremum. As the position of the actuator was moved from one end to the other, so did the extremum (diamond markers in fig. 5.18). Applying a larger strain moved this point closer to the centre of the actuator. The magnitude of strain at the free end was not recorded. In the cases with a fixed constraint on both ends, an S-shaped curve was observed with two local extrema of curvature. Larger strains caused these points to lie within the bounds of the actuator while smaller strains caused either one or both the points to appear outside the bounds of the actuator. The magnitude of maximum curvature was 0.013±0.005 (mean of 6, fixed-free) and 0.017±0.007 (mean of 8, fixed-fixed) in the two cases. This study shows that by changing the length, the position of the actuator and the constraints, the strips can be made to bend in various configurations.

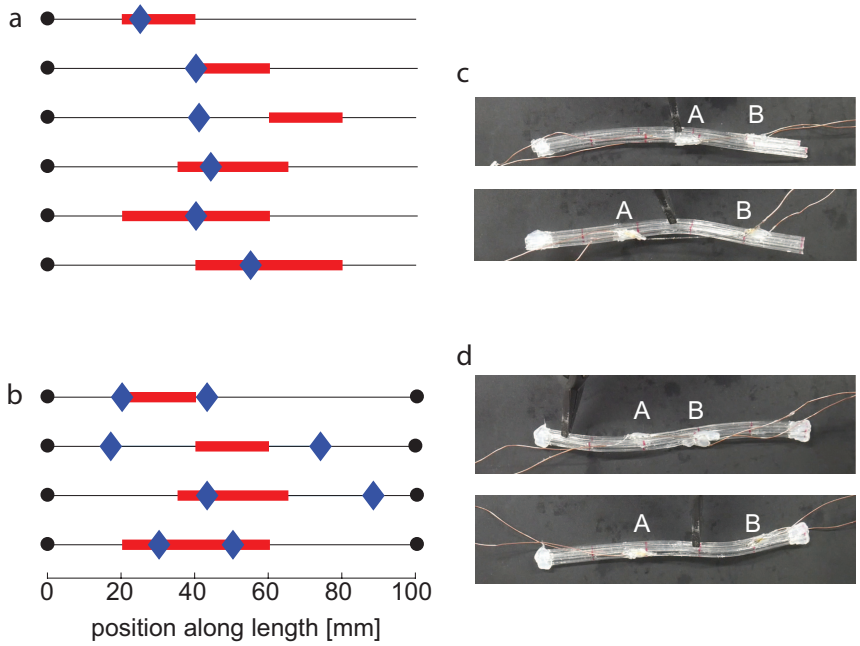

Figure 5.18: Location of extrema of curvature (diamonds) as observed for different end constraints (circle indicates a fixed constraint) and different actuator lengths (thick line). (a) Fixed-free constraint. (b) Fixed-fixed constraint. (c) Examples of fixed-free constraint. (d) Examples of fixed-fixed constraint.

5.10 Deformation of a Pellicular Sheet

In addition to exploring shapes of pairs of strips, the passive deformation of a cylindrical sheet was also analysed. A sheet with 20 strips (compared to approx. 40 in the case of euglenoids), each 100mm in length, was fabricated. The ends were sealed in adhesive. This

imposed a constraint at the ends which prevented sliding but allowed rotation. Unlike the examples from [184], where the ends were left free, the current design is closer to what is observed in the euglenoids where the strips in the pellicle coalesce to a point. An external load was applied in the form of a compression force and twist about the axis. The passive deformation of this cylindrical structure of strips is shown in fig. 5.19.

Markers were placed on the strips at 5mm intervals using permanent ink. Sliding of the strips to accommodate for the change in shape can be clearly seen through the movement of these markers. A maximum local displacement of 2.5mm of the strips was observed in the central region. A comparison of measured local strains with those predicted by the continuum model [69] is shown in fig. 5.19. The 2.5mm of displacement in the central portion (fig. 5.19b) agrees well with the model's prediction (fig. 5.19c).

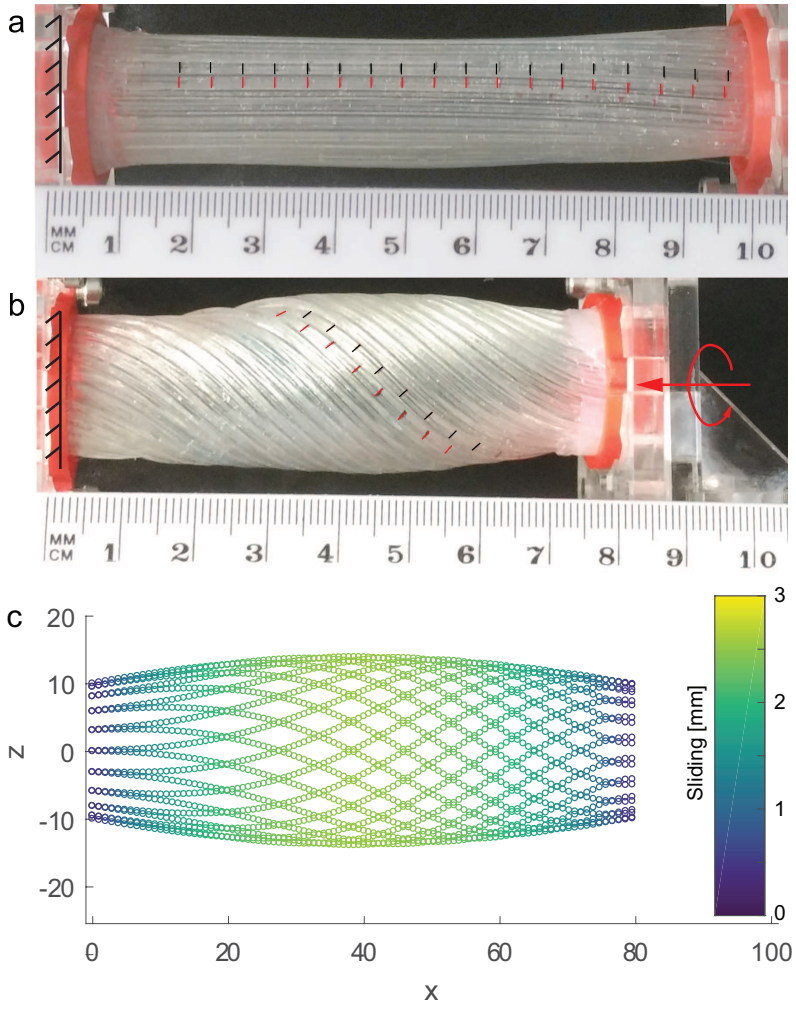

Figure 5.19: Sliding of strips during change in shape is seen through the movement of markers (placed at 5mm intervals) in the (a) undeformed and (b) deformed configuration. The amount of sliding (2.5mm) is comparable to that predicted by (c) the model [69]. [172] © 2019 IEEE

In addition to observing passive deformation, a simple soft robotic module with an

actively deforming surface was fabricated (fig. 5.20c). A total of 10 pairs of actuated strips of length 100mm were used. The length of the SMA actuator was 30mm and it was positioned central to the length on each pair. A flat sheet was first fabricated and the actuators affixed to adjacent pairs. The sheet was then rolled up into a cylindrical configuration. The free ends were then sealed using silicone adhesive (Sil-Poxy, Smooth-On) to impose a fixed constraint on both ends of the strips. All the actuators were connected together to form a parallel circuit. Change in shape of the robot upon actuation was observed.

In the initial configuration with no actuation (fig. 5.20a), the strips are parallel to the cylinder axis. In the deformed configuration after actuation (fig. 5.20b), the strips slide and twist, making a 4.5° with the axis. This indicated the potential to use this mechanism of active deformation in soft robots to enable change in shape.

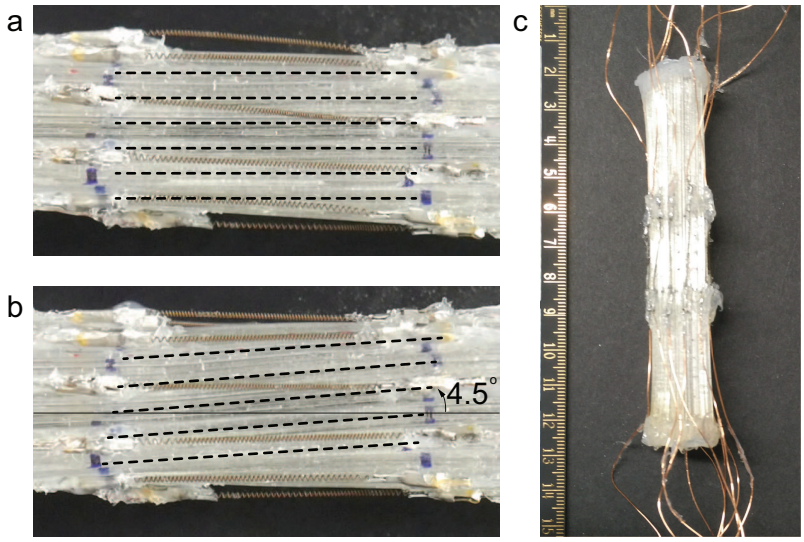

Figure 5.20: Dotted lines showing the orientation of strips in the (a) initial and (b) actuated configurations. (c) A prototype of the soft robot module.

5.11 Discussion

In this chapter, we have shown how a microscopic mechanism found in the *Euglena* unicellular organism can be replicated at a larger scale. We fabricated bio-inspired flexible pellicle strips to be used in the construction of soft robots that can both actively and passively change shape. We demonstrated three different behaviours (sliding, C-shape bending and S-shape bending) arising out of the same actuation mechanism on an interlocked pair of strips by simply changing the imposed constraints. We also explored shapes arising out of varied strains imposed at different locations along the length of the strips. In addition, we demonstrated active shape change in a soft robotic module. We believe that making a completely untethered robot is achievable.

In the case of a robot module, a measure that predicts failure of the surface is desirable. Experimentally determined values for the forces of separation provide this information. Results from peel tests (fig. 5.15) indicate that failure does not instantaneously rip the entire surface apart but only causes a local separation, and peeling is discontinuous.

A second observation during the tests was that the artificial pellicle surface is easy to repair. In traditional robot designs that use a monolithic skin, a failure requires the entire skin to be changed or patched using a suitable filler. For example, in the case of pneumatic networks [152], a punctured shell would have to be repaired using adhesive, which affects the performance of the system due to altering of material properties. Another example is the case of robots using elastomeric actuators, such as dielectric elastomers, where the entire membrane has to be replaced. In contrast, the strip-based pellicle surface presented here is easy to repair, does not require additional material and does not require a complete replacement. A separation of strips can simply be fixed by bringing the strips together and clicking them into place. Additionally, the sliding of strips is a simple shear deformation and hence there is negligible stretching or compression of material perpendicular to the direction of the strips [184].

A key difference in design between the euglenoid pellicle and the cylindrical structure presented here is the arrangement of strips at the ends (fig. 5.21). As mentioned above, strips within the euglenoid pellicle come together to a point. This is achieved through multiple stages of fusion of adjacent strips. This is a challenging feature to replicate in the engineered system. A simplification with a large circular gap was implemented in the design here, while ensuring similar constraints. On the other hand a model of unconstrained strips is presented in [184]. The difference in the two designs is in the force required to cause deformation. In an unconstrained case, force of actuation results in sliding. Whereas in a structure with constraints, sufficient force is required to cause buckling into the S-shaped configuration described earlier. In the current work, this force was not measured, but it would be an interesting study to take up.

The proposed actively deformable sheet is a step towards achieving euglenoid movement in a robot. However, we believe that other forms of locomotion, driven by shape change, such as terrestrial crawling, movement through granular media and traversal through a pipe are also realisable. Conforming soft grippers may also be realised with the same mechanism. It is also a means of creating active morphing surfaces beyond robotics, for example in architecture, medicine and wearable technologies. An excellent review of bio-inspired morphing surfaces is presented in [79], to which the current research adds a novel approach. A theoretical presentation on possible types of surfaces based on sliding of strips is given in [185]. A review of robots with adaptive morphology is presented in [186] many of which make use of deformable surfaces to achieve multi-modal capabilities, in which the current approach may be employed.

In the work presented here, we have only considered shapes arising from a single actuator on each pair of strips. Scaling to multiple actuators and maintaining their orientation

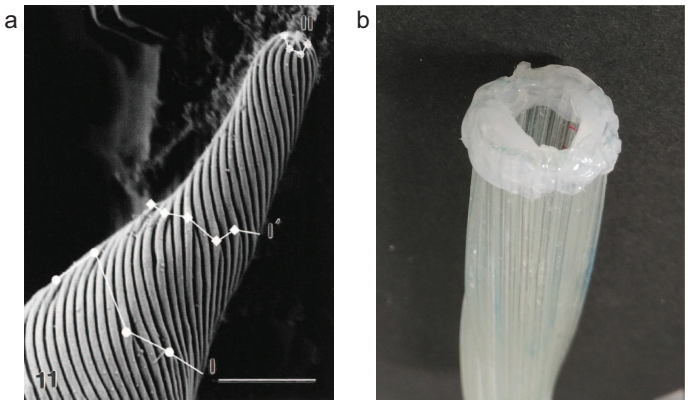

Figure 5.21: (a) Posterior end of *Euglena mutablis* showing strip reduction. Reproduced with permission from [64]. (b) A close up view of the end of the cylindrical soft robot module.

would be a challenge. Controlling several SMAs is challenging and their low efficiency is well documented. Actuation mechanisms other than SMAs, including some of the newer electrostatic ones mentioned earlier, are being explored in part due to this limitation. Alternative materials such as shape memory polymers and polymer blends with tunable stiffness are another avenue for research. Integrating a material model on top of the kinematic model [69] would be a useful addition to aid in the design of deformable surfaces. This would also help in predicting the force required to transition between two states.

There is also the possibility to consider surfaces of strips with non-uniform width leading to interesting structures and transitions of shape. It has been observed that in some euglenoids, a gradual increase in the robustness and size of the pellicle strips is correlated with a decrease in cell plasticity [174]. In the context of structures, this translates to regions of varying stiffness which can be achieved by simply altering the local geometry or the material of the individual strip.

Chapter 6

Conclusion and Future Work

This thesis adopted a bio-inspired approach to investigating and overcoming the problem of locomotion in soft robots. Following the development of novel actuators, structures and robots inspired by euglenoid movement, this chapter summarises the main conclusions of the work and presents an outlook for future research.

6.1 Conclusions

A primary aim of the thesis was to investigate ways in which euglenoid movement could be replicated in a robot. This work presented two different approaches to implementing such a means of locomotion in a soft robotic prototype. These approaches resulted in the original contributions as follows.

Quantifying Deforming Shapes

A mathematical representation based on elliptic Fourier descriptors was presented in chapter 3 as a means to quantitatively describe shapes of deformable entities across a wide variety of scales. This included case studies involving organisms (euglenoids, *Manduca sexta* and *Sphacelodes sp.*) and robots with soft bodies. One of the outcomes was that a quantitative representation of cell shapes during euglenoid movement presented a formal description as opposed to the subjective terms used in the past century to describe them [61]. The method was also able to identify key features of shape that enabled euglenoid movement and aided in the design of the soft robots.

In the case of the caterpillars, the analysis of descriptors captured the differences in motion between the species. It also correctly identified the motion of the terminal proleg as being a key aspect of the gait in the *Manduca*. Dynamics such as cyclic shape change and phase delay between movement of segments were also captured. The different modes of oscillation in the swinging tentacle, including the difference in operation within diverse media was also shown. Using multiple viewing directions as a possible extension of the method to three dimensions was discussed.

Hyper-Elastic Bellows (HEBs)

Based on the analysis of cell shapes, the design of an actuator capable of large strains [155] was presented in chapter 4. The novelty of the design is that it translates simple pneumatic input into predictable and sophisticated deformation using a pleated bellows like design by exploiting the hyper-elastic property of the material of construction. Operation under both positive and negative pressure were demonstrated with four distinctly identifiable states of expansion or contraction. This is a marked difference from other pneumatic actuators such as [152, 156, 157, 187, 188] that operate in a single regime.

A comparison with different classes of actuators showed that the HEBs occupy a unique operational space, the behaviour within which can be tuned by changing design parameters such as the angle of the folds in rest state, their density and even their geometry. The existence of an axially expanding state prior to a ballooning state is an additional distinguishing feature. This is particularly useful in reproducing transitions of shape that are similar to those in the euglenoids, where an extension of a slender portion of the cell is observed prior to transfer of mass from one end of the cell to the other.

In terms of performance metrics, the HEBs achieved a 450% change in length and a doubling of radius along with a volume change of over 300 times. Thus, the ability of the HEB actuator in reproducing the giant deformations of euglenoid cells was demonstrated. The design of the HEBs enables the reproduction of the three key features of shape change seen in euglenoids: expansion and contraction in length, large change in radius and anterio-posterior shifting of mass.

The individual HEB design can be fabricated at multiple scales, as was demonstrated in the thesis. It can therefore be used in other applications such as devices for rehabilitation of stroke patients, implantable medical devices and haptic interfaces. The compliant nature of the material is advantageous in these scenarios that involve interaction with humans.

EuMoBot

The HEB actuators were used to fabricate soft robots called EuMoBots [165] capable of changing shape and moving like the euglenoids in chapter 4. These are the first robots of their type capable of euglenoid-like movement in a fluid. Their motion in a low Reynolds number environment is hydro-dynamically similar to that of euglenoids. This was true in the case of both the robots, differing in characteristic length by an order of magnitude, proving that euglenoid movement can indeed be achieved in a robot and that it can be replicated across different scales.

Comparison of shapes between the robots and the organism showed up to 85% similarity. The robots and euglenoids though identical in swimming behaviour are very distinct in their physical construction. Therefore any method of using landmarks to compare their shapes is prone to subjective errors. The method of describing the contours of the two constantly deforming soft bodies using elliptical Fourier descriptors demonstrates the elegance

of the mathematical tool developed in chapter 3. The quantifiable measure of similarity through the use of principal components of shape is yet another original contribution of this thesis.

The multi-modal locomotion ability of the robot was demonstrated in chapter 4. The robot is capable of moving in non-fluid environments, which was illustrated through its motion on a flat surface. The expansion and contraction of the folds of the bellows is a way to regulate friction between the robot and the surface. This ability to regulate friction was demonstrated in a second example in which the robot moved up the interior of a vertical pipe. The advantage of the HEBs is further highlighted in this example where the same actuator can be used to achieve anchoring as well as the displacement of the body, the two key elements required for inch-worm like locomotion. This is a welcome departure from conventional robots (and soft robots such as [82] and [189]) built for this purpose where different actuation technologies are employed for linear extension and providing traction. Since the design can be scaled down, there is potential for use in invasive medical procedures alon the lines of the peristaltic endoscope presented in [29].

Bio-inspired Pellicular Strips

The thesis explored the replication of the microscopic structure of the euglenoid pellicle in a millimetre scale design [172]. Bio-inspired polymer strips with a cross section mimicking that found in euglenoids was fabricated in chapter 5. In addition, the mechanism of sliding in the pellicle that results in the drastic changes in shape of the euglenoids was also reproduced. The equi-area shear deformation that is unique to euglenoids is characterised by two key requirements: one that the strips maintain a constant distance between each other and the other that they be free to slide against each other [175]. The S-shaped design of the polymeric strips presented in this thesis is a novel embodiment of these requirements in an engineered system.

Shape change through both passive and active sliding in a sheet of interlocked strips was demonstrated. An SMA actuator was used as an equivalent muscle-like actuator to achieve active sliding. Three types of deformation in a pair of strips was demonstrated namely, sliding, C-shaped bending and S-shaped bending based on constrains imposed at the ends of the strip. A multitude of shapes arising out of variation in actuation strain and constrains was demonstrated. The key result from this investigation is that a global deformation in shape can be attained through appropriate local strain. Additional novelty included successfully showing the working of a microscopic structure at a larger scale while maintaining functionality. An active shape morphing cylindrical sheet, mimicking the arrangement in the euglenoids albeit with fewer strips, was shown to change in shape upon actuation. The thesis therefore proposes pelliclular strips as a new way to design shape changing soft robots.

The polymer strips were also characterised and the force required to separate a pair of

interlocked strips was experimentally determined (> 8N) as a measure of predicting the design limitations for structures composed of strips. Based on a kinematic model of sliding in the pellicle [69], a design tool was developed in MATLAB to investigate the diversity of shapes both euglenoid-like or otherwise. A theoretical exploration of shapes is presented in [185] which, we believe, can be achieved using the designs presented in this thesis. Shape morphing surfaces with pneumatic channels have recently been presented in [190]. An advantage of the pellicle-like design over the one presented there is that deformation is not limited by mechanical failure of the material under tensile loads, which is very likely in the case of designs employing elastomers in their construction.

Fabrication of structures with a predefined twist in the rest configuration was shown. In addition, the manufacture of sheets with different polymers was presented. There is scope for exploiting material properties to achieve an even larger diversity in behaviour. Ease of repair was shown to be an added benefit.

6.2 Future Work

The thesis successfully demonstrated its main goal of implementing of euglenoid movement in a soft robot. However, there is scope for improvement in each of the individual contributions made in the work.

Extension of Fourier Descriptors

The method of describing deforming shapes with elliptic Fourier descriptors is at the moment limited to kinematic analysis. Since the information about the shape is restricted to the knowledge of the contour, there is a loss in detail regarding points on the surface of the deforming body. Therefore mechanical interactions (eg. frictional interactions with a solid surface, hydrodynamic interactions with the surrounding fluid) that require knowledge of both the position and velocity of points on the surface cannot be studied using this method. As an illustrative example, consider the motion of a spherical balloon in the air and a soap bubble in water. The dynamics of these bodies would appear to be the same in terms of the descriptors of contour presented in this thesis. The difference in flow around the two bodies can only be understood by looking at the motion of markers on the surface. Complementing the boundary descriptors with landmarks is a possible avenue for investigation.

Extending the use of elliptic Fourier descriptors to dynamic tasks such as the control of a deformable robot will be considered in the future. A possible application is in using visual feedback to deform an object into a desired shape [191]. Applications to morphological computation will also be studied. An interesting use of the measures would be to quantify the amount of computation happening in the body using a low dimensional representation of observed behaviour to distinguish between morphologies that are useful and harmful to a desired functionality [192]. Quantifying shape change also enables the use of artificial

intelligence approaches for example, neural networks to analyse or control soft robots, since the component scores can be used to train the neural network. Another application would be to study the transients of shape in addition to studying steady state motion as was done in this thesis.

Improvements to EuMoBot

The three segment robots described in the thesis were tethered and relied on external infrastructure to displace fluid within the body. There is scope for making a completely untethered robot by incorporating pumps within the body. Alternatively, other forms of generating pressures such as through a chemical reaction [193, 194, 195] could be employed, provided a method for controlled release and withdrawal is implemented. Since the motion is cyclic, an oscillating circuit implemented using a fluid logic circuit [196] is a possibility.

The robots at the moment are incapable of changing direction. Investigation of mechanisms to implement this such as actuated coils of shape memory alloy [170], using constraints on the material [171] is a possibility. In addition, the efficiency of the robot and optimal changes of shape were not studied. Driving the robot by matching estimated shapes to a reference set of shapes is another avenue for research.

Although the similarity of the robot in swimming like the euglenoid was demonstrated, there is scope to study the hydrodynamics in greater detail. For example, the flow of fluid around the robot could be investigated for example, through particle image velocimetry (PIV). Studying the flow around the euglenoid is extremely challenging due to its small size. Only theoretical estimates have been proposed [69]. Having shown the similarity in Reynold's number, the robots can be used as tools to study the movement of euglenoids, thereby contributing back to biology.

Shape Morphing Surfaces

A limitation of the current design of actively deformable surfaces is the method of actuation used. While coiled SMA actuators were sufficient to prove the concept of deformation, scaling them to large numbers is a challenge. Since the efficiency of SMA actuators is small (1% [1]), employing multiple actuators would be extremely inefficient. Alternative actuation technologies such as the muscle-like actuation discussed in chapter 2 are being investigated.

It is possible to fabricate polymer strips at a larger scale to accommodate the DEA-EA actuation mechanism. Care must be taken to ensure that the strips remain flexible enough to deform into the desired shape. Investigating alternative shapes for the cross-section to address this issue (by altering the second moment of area) is a possibility. Material properties such as the modulus of elasticity can also be tuned by blending polymers.

Bibliography

[1] S. Kim, C. Laschi, and B. Trimmer, "Soft robotics: a bioinspired evolution in robotics," *Trends in biotechnology*, vol. 31, no. 5, pp. 287–294, 2013.

[2] N. F. Lepora, P. Verschure, and T. J. Prescott, "The state of the art in biomimetics," *Bioinspiration & biomimetics*, vol. 8, no. 1, p. 013001, 2013.

[3] Moderator:, J. H. Long Jr, Participants:, S. Combes, J. Nawroth, M. Hale, G. Lauder, S. Swartz, R. Quinn, and H. Chiel, "How does soft robotics drive research in animal locomotion?," *Soft Robotics*, vol. 1, no. 3, pp. 161–168, 2014.

[4] B. Trimmer, "A confluence of technology: Putting biology into robotics," 2014.

[5] S. Kim, M. Spenko, S. Trujillo, B. Heyneman, D. Santos, and M. R. Cutkosky, "Smooth vertical surface climbing with directional adhesion," *IEEE Transactions on robotics*, vol. 24, no. 1, pp. 65–74, 2008.

[6] P. S. Sreetharan, J. P. Whitney, M. D. Strauss, and R. J. Wood, "Monolithic fabrication of millimeter-scale machines," *Journal of Micromechanics and Microengineering*, vol. 22, no. 5, p. 055027, 2012.

[7] M. J. Pearson, B. Mitchinson, J. C. Sullivan, A. G. Pipe, and T. J. Prescott, "Biomimetic vibrissal sensing for robots," *Philosophical Transactions of the Royal Society B: Biological Sciences*, vol. 366, no. 1581, pp. 3085–3096, 2011.

[8] C. Chorley, C. Melhuish, T. Pipe, and J. Rossiter, "Development of a tactile sensor based on biologically inspired edge encoding," in *2009 International Conference on Advanced Robotics*, pp. 1–6, IEEE, 2009.

[9] C. Laschi, M. Cianchetti, B. Mazzolai, L. Margheri, M. Follador, and P. Dario, "Soft robot arm inspired by the octopus," *Advanced Robotics*, vol. 26, no. 7, pp. 709–727, 2012.

[10] M. Raibert, K. Blankespoor, G. Nelson, and R. Playter, "Bigdog, the rough-terrain quadruped robot," *IFAC Proceedings Volumes*, vol. 41, no. 2, pp. 10822–10825, 2008.

[11] M. Hutter, C. Gehring, M. Bloesch, M. A. Hoepflinger, C. D. Remy, and R. Siegwart, "StarlETH: A compliant quadrupedal robot for fast, efficient, and versatile locomotion," in *Adaptive Mobile Robotics*, pp. 483–490, World Scientific, 2012.

[12] S. Seok, A. Wang, M. Y. Chuah, D. Otten, J. Lang, and S. Kim, "Design principles for highly efficient quadrupeds and implementation on the MIT Cheetah robot," in *2013 IEEE International Conference on Robotics and Automation*, pp. 3307–3312, IEEE, 2013.

[13] H. Lipson, "Challenges and opportunities for design, simulation, and fabrication of soft robots," *Soft Robotics*, vol. 1, no. 1, pp. 21–27, 2014.

[14] B. Trimmer, "Soft robots and size," 2015.

[15] "The euglenoid project." http://euglena.msu.edu/index.shtml.

[16] M. Calisti, G. Picardi, and C. Laschi, "Fundamentals of soft robot locomotion," *Journal of The Royal Society Interface*, vol. 14, no. 130, p. 20170101, 2017.

[17] T. Suzaki and R. Williamson, "Euglenoid movement in Euglena fusca: evidence for sliding between pellicular strips," *Protoplasma*, vol. 124, no. 1-2, pp. 137–146, 1985.

[18] K. J. Mealand, "Mikroskopisk pacman." . https://www.usn.no/forskning/forskningsnytt/mikroskopisk-pacman-article194412-27233.html. First Published: 28.06.16. Accessed: 08.03.18.

[19] G. Noselli, A. Beran, M. Arroyo, and A. DeSimone, "Swimming Euglena respond to confinement with a behavioural change enabling effective crawling," *Nature Physics*, p. 1, 2019.

[20] A. K. Stowers and D. Lentink, "Folding in and out: passive morphing in flapping wings," *Bioinspiration & biomimetics*, vol. 10, no. 2, p. 025001, 2015.

[21] H.-T. Lin and B. Trimmer, "Caterpillars use the substrate as their external skeleton: a behavior confirmation," *Communicative & integrative biology*, vol. 3, no. 5, pp. 471–474, 2010.

[22] N. D. Naclerio, C. M. Hubicki, Y. O. Aydin, D. I. Goldman, and E. W. Hawkes, "Soft robotic burrowing device with tip-extension and granular fluidization," in *2018 IEEE/RSJ International Conference on Intelligent Robots and Systems (IROS)*, pp. 5918–5923, IEEE, 2018.

[23] T. Hunt, "Ozy's record jar-opening skills." . http://www.stuff.co.nz/marlborough-express/news/national-news/9603939/Ozys-record-jar-opening-skills. Accessed: 10.09.16.

[24] B. A. Trimmer, A. E. Takesian, B. M. Sweet, C. B. Rogers, D. C. Hake, and D. J. Rogers, "Caterpillar locomotion: a new model for soft-bodied climbing and burrowing robots," in *7th International Symposium on Technology and the Mine Problem*, vol. 1, pp. 1–10, Monterey, CA: Mine Warfare Association, 2006.

[25] K. Jung, J. C. Koo, Y. K. Lee, H. R. Choi, *et al.*, "Artificial annelid robot driven by soft actuators," *Bioinspiration & biomimetics*, vol. 2, no. 2, p. S42, 2007.

[26] T. Umedachi, V. Vikas, and B. Trimmer, "Softworms: the design and control of non-pneumatic, 3D-printed, deformable robots," *Bioinspiration & biomimetics*, vol. 11, no. 2, p. 025001, 2016.

[27] S. Seok, C. D. Onal, K.-J. Cho, *et al.*, "Meshworm: a peristaltic soft robot with antagonistic nickel titanium coil actuators," *IEEE/ASME Transactions on mechatronics*, vol. 18, no. 5, pp. 1485–1497, 2013.

[28] C. D. Onal, R. J. Wood, and D. Rus, "An origami-inspired approach to worm robots," *IEEE/ASME Transactions on Mechatronics*, vol. 18, no. 2, pp. 430–438, 2013.

[29] E. V. Mangan, D. A. Kingsley, R. D. Quinn, and H. J. Chiel, "Development of a peristaltic endoscope," in *Proceedings 2002 IEEE International Conference on Robotics and Automation (Cat. No. 02CH37292)*, vol. 1, pp. 347–352, IEEE, 2002.

[30] R. F. Shepherd, F. Ilievski, W. Choi, S. A. Morin, A. A. Stokes, A. D. Mazzeo, X. Chen, M. Wang, and G. M. Whitesides, "Multigait soft robot," *Proceedings of the National Academy of Sciences*, vol. 108, no. 51, pp. 20400–20403, 2011.

[31] M. Calisti, M. Giorelli, and C. Laschi, "A locomotion strategy for an octopus-bioinspired robot," in *Conference on Biomimetic and Biohybrid Systems*, pp. 337–338, Springer, 2012.

[32] S. Mao, E. Dong, S. Zhang, M. Xu, and J. Yang, "A new soft bionic starfish robot with multi-gaits," in *2013 IEEE/ASME International Conference on Advanced Intelligent Mechatronics*, pp. 1312–1317, IEEE, 2013.

[33] Y. Sugiyama and S. Hirai, "Crawling and jumping of deformable soft robot," in *2004 IEEE/RSJ International Conference on Intelligent Robots and Systems (IROS)(IEEE Cat. No. 04CH37566)*, vol. 4, pp. 3276–3281, IEEE, 2004.

[34] R. Bleischwitz, R. de Kat, and B. Ganapathisubramani, "Aspect-ratio effects on aeromechanics of membrane wings at moderate reynolds numbers," *AIAA Journal*, vol. 53, no. 3, pp. 780–788, 2015.

[35] A. Ramezani, S.-J. Chung, and S. Hutchinson, "A biomimetic robotic platform to study flight specializations of bats," *Science Robotics*, vol. 2, no. 3, pp. Art–No, 2017.

[36] K. Suzumori, S. Endo, T. Kanda, N. Kato, and H. Suzuki, "A bending pneumatic rubber actuator realizing soft-bodied manta swimming robot," in *Proceedings 2007 IEEE International Conference on Robotics and Automation*, pp. 4975–4980, IEEE, 2007.

[37] Z. Chen, T. I. Um, and H. Bart-Smith, "Bio-inspired robotic manta ray powered by ionic polymer–metal composite artificial muscles," *International Journal of Smart and Nano Materials*, vol. 3, no. 4, pp. 296–308, 2012.

[38] K. H. Low, J. Yang, A. P. Pattathil, and Y. Zhang, "Initial prototype design and investigation of an undulating body by SMA," in *2006 IEEE International Conference on Automation Science and Engineering*, pp. 472–477, IEEE, 2006.

[39] Z. Wang, G. Hang, J. Li, Y. Wang, and K. Xiao, "A micro-robot fish with embedded SMA wire actuated flexible biomimetic fin," *Sensors and Actuators A: Physical*, vol. 144, no. 2, pp. 354–360, 2008.

[40] X. Ye, Y. Su, S. Guo, and L. Wang, "Design and realization of a remote control centimeter-scale robotic fish," in *2008 IEEE/ASME International Conference on Advanced Intelligent Mechatronics*, pp. 25–30, IEEE, 2008.

[41] R. K. Katzschmann, A. D. Marchese, and D. Rus, "Hydraulic autonomous soft robotic fish for 3D swimming," in *Experimental Robotics*, pp. 405–420, Springer, 2016.

[42] A. D. Marchese, C. D. Onal, and D. Rus, "Autonomous soft robotic fish capable of escape maneuvers using fluidic elastomer actuators," *Soft Robotics*, vol. 1, no. 1, pp. 75–87, 2014.

[43] J. Pawlowski, S. Audic, S. Adl, D. Bass, L. Belbahri, C. Berney, S. S. Bowser, I. Cepicka, J. Decelle, M. Dunthorn, *et al.*, "CBOL protist working group: barcoding eukaryotic richness beyond the animal, plant, and fungal kingdoms," *PLoS biology*, vol. 10, no. 11, p. e1001419, 2012.

[44] R. O'dor, "A census of marine life," *BioScience*, vol. 54, no. 2, pp. 92–93, 2004.

[45] C. Dobell *et al.*, "Antony van Leeuwenhoek and his 'Little Animals'.," 1932.

[46] J. Harris, "VII. some microscopical observations of vast numbers of animalcula seen in water by John Harris, MA Rector of Winchelsea in Sussex, and FR S," *Philosophical Transactions of the Royal Society of London*, vol. 19, no. 220, pp. 254–259.

[47] S. D. Schwartzbach and S. Shigeoka, *Euglena: Biochemistry, Cell and Molecular Biology*, vol. 979. Springer, 2017.

[48] A. G. Russell, Y.-i. Watanabe, J. M. Charette, and M. W. Gray, "Unusual features of fibrillarin cDNA and gene structure in Euglena gracilis: evolutionary conservation of core proteins and structural predictions for methylation-guide box C/D snoRNPs throughout the domain Eucarya," *Nucleic acids research*, vol. 33, no. 9, pp. 2781–2791, 2005.

[49] J. J. Wolken, "An experimental organism for biochemical and biophysical studies," *Institute of Microbiology, Rutgers, The State University*, 1961.

[50] B. S. Leander, H. J. Esson, and S. A. Breglia, "Macroevolution of complex cytoskeletal systems in euglenids," *Bioessays*, vol. 29, no. 10, pp. 987–1000, 2007.

[51] G. F. Leedale, "Ultrastructure," in *The Biology of Euglena Vol. III Physiology* (D. E. Buetow, ed.), ch. 1, pp. 1–28, London: Academic Press, 1982.

[52] M. A. Farmer, "Euglenozoa," in *Eukaryotic microbes* (M. Schaechter, ed.), ch. 22, pp. 311–321, London: Academic Press, 2011.

[53] G. F *Archiv fr Protistenkunde*, vol. 60, p. 51, 1927.

[54] G. Leedale, B. Meeuse, and E. Pringsheim, "Structure and physiology of Euglena spirogyra. iii–vi," *Archives of Microbiology*, vol. 50, no. 2, pp. 133–155, 1965.

[55] J. B. Lackey, "The flora and fauna of surface waters polluted by acid mine drainage," *Public Health Reports (1896-1970)*, pp. 1499–1507, 1938.

[56] E. C. Bovee, "Movement and locomotion of Euglena," in *The Biology of Euglena Vol. III Physiology* (D. E. Buetow, ed.), ch. 4, pp. 143–168, London: Academic Press, 1982.

[57] P. J. Keeling, "Chromalveolates and the evolution of plastids by secondary endosymbiosis 1," *Journal of Eukaryotic Microbiology*, vol. 56, no. 1, pp. 1–8, 2009.

[58] K. Hilmbauer, "Zellphysiologische studien an Euglenaceen, besonders anTrachelomonas," *Protoplasma*, vol. 43, no. 3, pp. 192–227, 1954.

[59] R. C. BATES and R. E. HURLBERT, "The effect of acetate on Euglena gracilis var. bacillaris as a function of environmental conditions," *The Journal of Protozoology*, vol. 17, no. 1, pp. 134–138, 1970.

[60] E. MIKOLAJCZYK and B. DIEHN, "Light-induced body movement of Euglena gracilis coupled to flagellar photophobic responses by mechanical stimulation," *The Journal of Protozoology*, vol. 23, no. 1, pp. 144–147, 1976.

[61] E. Pringsheim, "Taxonomic problems in the Euglenineae," *Biological Reviews*, vol. 23, no. 1, pp. 46–61, 1948.

[62] G. Leedale, "Pellicle structure in euglena," *British Phycological Bulletin*, vol. 2, no. 5, pp. 291–306, 1964.

[63] T. Suzaki and R. E. Williamson, "Cell surface displacement during euglenoid movement and its computer simulation," *Cytoskeleton*, vol. 6, no. 2, pp. 186–192, 1986.

[64] B. S. Leander and M. A. Farmer, "Comparative morphology of the euglenid pellicle. i. patterns of strips and pores," *Journal of Eukaryotic Microbiology*, vol. 47, no. 5, pp. 469–479, 2000.

[65] B. S. Leander and M. A. Farmer, "Comparative morphology of the euglenid pellicle. ii. diversity of strip substructure," *Journal of Eukaryotic Microbiology*, vol. 48, no. 2, pp. 202–217, 2001.

[66] C. L. Lachney and T. A. Lonergan, "Regulation of cell shape in Euglena gracilis. iii. involvement of stable microtubules," *Journal of cell science*, vol. 74, no. 1, pp. 219–237, 1985.

[67] T. A. Lonergan, "Regulation of cell shape in Euglena gracilis. iv. localization of actin, myosin and calmodulin," *Journal of cell science*, vol. 77, no. 1, pp. 197–208, 1985.

[68] S. M. Gittleson, "Flagellar activity and Reynolds number," *Transactions of the American Microscopical Society*, vol. 93, no. 2, pp. 272–276, 1974.

[69] M. Arroyo, L. Heltai, D. Millán, and A. DeSimone, "Reverse engineering the euglenoid movement," *Proceedings of the National Academy of Sciences*, vol. 109, no. 44, pp. 17874–17879, 2012.

[70] E. Lauga and T. R. Powers, "The hydrodynamics of swimming microorganisms," *Reports on Progress in Physics*, vol. 72, no. 9, p. 096601, 2009.

[71] E. M. Purcell, "Life at low Reynolds number," in *Physics and Our World: Reissue of the Proceedings of a Symposium in Honor of Victor F Weisskopf*, pp. 47–67, World Scientific, 2014.

[72] A. Najafi and R. Golestanian, "Simple swimmer at low Reynolds number: Three linked spheres," *Physical Review E*, vol. 69, no. 6, p. 062901, 2004.

[73] J. Avron, O. Kenneth, and D. Oaknin, "Pushmepullyou: an efficient micro-swimmer," *New Journal of Physics*, vol. 7, no. 1, p. 234, 2005.

[74] F. Alouges, A. DeSimone, and L. Heltai, "Numerical strategies for stroke optimization of axisymmetric microswimmers," *Mathematical Models and Methods in Applied Sciences*, vol. 21, no. 02, pp. 361–387, 2011.

[75] O. S. Pak, E. Lauga, C. Duprat, and H. Stone, "Theoretical models of low-reynolds-number locomotion," *Fluid-Structure Interactions in Low-Reynolds-Number Flows*, p. 100, 2015.

[76] G. Cicconofri and A. DeSimone, "Modelling biological and bio-inspired swimming at microscopic scales: Recent results and perspectives," *Computers & Fluids*, 2018.

[77] M. Rossi, G. Cicconofri, A. Beran, G. Noselli, and A. DeSimone, "Kinematics of flagellar swimming in Euglena gracilis: Helical trajectories and flagellar shapes," *Proceedings of the National Academy of Sciences*, vol. 114, no. 50, pp. 13085–13090, 2017.

[78] A. C. Tsang, A. T. Lam, and I. H. Riedel-Kruse, "Polygonal motion and adaptable phototaxis via flagellar beat switching in the microswimmer Euglena gracilis," *Nature Physics*, vol. 14, no. 12, p. 1216, 2018.

[79] K. Oliver, A. Seddon, and R. S. Trask, "Morphing in nature and beyond: a review of natural and synthetic shape-changing materials and mechanisms," *Journal of Materials Science*, vol. 51, no. 24, pp. 10663–10689, 2016.

[80] D. Rus and M. T. Tolley, "Design, fabrication and control of soft robots," *Nature*, vol. 521, no. 7553, p. 467, 2015.

[81] M. Ashby in *Material Selection in Mechanical Design 3rd edition*, London: Butterworth-Heinemann, 2004.

[82] A. G. Mark, S. Palagi, T. Qiu, and P. Fischer, "Auxetic metamaterial simplifies soft robot design," in *2016 IEEE International Conference on Robotics and Automation (ICRA)*, pp. 4951–4956, Ieee, 2016.

[83] A. Rafsanjani and D. Pasini, "Bistable auxetic mechanical metamaterials inspired by ancient geometric motifs," *Extreme Mechanics Letters*, vol. 9, pp. 291–296, 2016.

[84] R. S. Naboni and L. Mirante, "Metamaterial computation and fabrication of auxetic patterns for architecture," 2015.

[85] K. Wang, Y.-H. Chang, Y. Chen, C. Zhang, and B. Wang, "Designable dual-material auxetic metamaterials using three-dimensional printing," *Materials & Design*, vol. 67, pp. 159–164, 2015.

[86] T. W. Tan, G. R. Douglas, T. Bond, and A. S. Phani, "Compliance and longitudinal strain of cardiovascular stents: influence of cell geometry," *Journal of Medical Devices*, vol. 5, no. 4, p. 041002, 2011.

[87] A. T. Conn and J. Rossiter, "Smart radially folding structures," *IEEE/ASME Transactions on Mechatronics*, vol. 17, no. 5, pp. 968–975, 2012.

[88] J. Rossiter, K. Takashima, F. Scarpa, P. Walters, and T. Mukai, "Shape memory polymer hexachiral auxetic structures with tunable stiffness," *Smart Materials and Structures*, vol. 23, no. 4, p. 045007, 2014.

[89] G. Fallacara, M. Barberio, and M. Colella, "Learning by designing: Investigating new didactic methods to learn architectural design," *Turkish Online Journal of Educational Technology*, pp. 455–465, 2017.

[90] M. Sanami, N. Ravirala, K. Alderson, and A. Alderson, "Auxetic materials for sports applications," *Procedia Engineering*, vol. 72, pp. 453 – 458, 2014. The Engineering of Sport 10.

[91] M. F. Simons, K. M. Digumarti, A. T. Conn, and J. Rossiter, "Tiled auxetic cylinders for soft robots," in *2019 IEEE International Conference on Soft Robotics (RoboSoft)*, pp. 62–67, IEEE, 2019.

[92] J. C. Á. Elipe and A. D. Lantada, "Comparative study of auxetic geometries by means of computer-aided design and engineering," *Smart Materials and Structures*, vol. 21, no. 10, p. 105004, 2012.

[93] F. Scarpa, P. Panayiotou, and G. Tomlinson, "Numerical and experimental uniaxial loading on in-plane auxetic honeycombs," *The Journal of Strain Analysis for Engineering Design*, vol. 35, no. 5, pp. 383–388, 2000.

[94] F. Scarpa, C. Smith, M. Ruzzene, and M. Wadee, "Mechanical properties of auxetic tubular truss-like structures," *physica status solidi (b)*, vol. 245, no. 3, pp. 584–590, 2008.

[95] F. B. Coulter and A. Ianakiev, "4D printing inflatable silicone structures," *3D Printing and Additive Manufacturing*, vol. 2, no. 3, pp. 140–144, 2015.

[96] B. Trimmer, "A practical approach to soft actuation," 2017.

[97] A. Poole and J. D. Booker, "Classification and selection of actuator technologies with consideration of stimuli generation," in *Electroactive Polymer Actuators and Devices (EAPAD) 2008*, vol. 6927, p. 692728, International Society for Optics and Photonics, 2008.

[98] F. Carpi and E. Smela, *Biomedical applications of electroactive polymer actuators*. John Wiley & Sons, 2009.

[99] H. Rodrigue, W. Wang, M.-W. Han, T. J. Kim, and S.-H. Ahn, "An overview of shape memory alloy-coupled actuators and robots," *Soft robotics*, vol. 4, no. 1, pp. 3–15, 2017.

[100] J. M. Jani, M. Leary, A. Subic, and M. A. Gibson, "A review of shape memory alloy research, applications and opportunities," *Materials & Design (1980-2015)*, vol. 56, pp. 1078–1113, 2014.

[101] A. OHalloran, F. Omalley, and P. McHugh, "A review on dielectric elastomer actuators, technology, applications, and challenges," *Journal of Applied Physics*, vol. 104, no. 7, p. 9, 2008.

[102] A. T. Conn, *Development of novel flapping mechanism technologies for insect-inspired micro air vehicles*. PhD thesis, University of Bristol, 2008.

[103] C.-P. Chou and B. Hannaford, "Measurement and modeling of McKibben pneumatic artificial muscles," *IEEE Transactions on robotics and automation*, vol. 12, no. 1, pp. 90–102, 1996.

[104] K. Suzumori, S. Iikura, and H. Tanaka, "Applying a flexible microactuator to robotic mechanisms," *IEEE Control systems magazine*, vol. 12, no. 1, pp. 21–27, 1992.

[105] M. T. Tolley, R. F. Shepherd, B. Mosadegh, K. C. Galloway, M. Wehner, M. Karpelson, R. J. Wood, and G. M. Whitesides, "A resilient, untethered soft robot," *Soft robotics*, vol. 1, no. 3, pp. 213–223, 2014.

[106] R. S. Diteesawat, T. Helps, M. Taghavi, and J. Rossiter, "High strength bubble artificial muscles for walking assistance," in *2018 IEEE International Conference on Soft Robotics (RoboSoft)*, pp. 388–393, IEEE, 2018.

[107] S. Kim, E. Hawkes, K. Choy, M. Joldaz, J. Foleyz, and R. Wood, "Micro artificial muscle fiber using niti spring for soft robotics," in *Intelligent Robots and Systems, 2009. IROS 2009. IEEE/RSJ International Conference on*, pp. 2228–2234, IEEE, 2009.

[108] C. S. Haines, M. D. Lima, N. Li, G. M. Spinks, J. Foroughi, J. D. Madden, S. H. Kim, S. Fang, M. J. de Andrade, F. Göktepe, *et al.*, "Artificial muscles from fishing line and sewing thread," *science*, vol. 343, no. 6173, pp. 868–872, 2014.

[109] A. Simeonov, T. Henderson, Z. Lan, G. Sundar, A. Factor, J. Zhang, and M. Yip, "Bundled super-coiled polymer artificial muscles: Design, characterization, and modeling," *IEEE Robotics and Automation Letters*, vol. 3, no. 3, pp. 1671–1678, 2018.

[110] M. Suzuki and N. Kamamichi, "Control of twisted and coiled polymer actuator with anti-windup compensator," *Smart Materials and Structures*, vol. 27, no. 7, p. 075014, 2018.

[111] S. M. Mirvakili and I. W. Hunter, "Multidirectional artificial muscles from nylon," *Advanced Materials*, vol. 29, no. 4, p. 1604734, 2017.

[112] J. Huber, N. Fleck, and M. Ashby, "The selection of mechanical actuators based on performance indices," *Proceedings of the Royal Society of London. Series A: Mathematical, physical and engineering sciences*, vol. 453, no. 1965, pp. 2185–2205, 1997.

[113] F. Ilievski, A. D. Mazzeo, R. F. Shepherd, X. Chen, and G. M. Whitesides, "Soft robotics for chemists," *Angewandte Chemie International Edition*, vol. 50, no. 8, pp. 1890–1895, 2011.

[114] S. Shian, K. Bertoldi, and D. R. Clarke, "Use of aligned fibers to enhance the performance of dielectric elastomer inchworm robots," in *Electroactive Polymer Actuators and Devices (EAPAD) 2015*, vol. 9430, p. 94301P, International Society for Optics and Photonics, 2015.

[115] J. Cao, L. Qin, H. P. Lee, and J. Zhu, "Development of a soft untethered robot using artificial muscle actuators," in *Electroactive Polymer Actuators and Devices (EAPAD) 2017*, vol. 10163, p. 101631X, International Society for Optics and Photonics, 2017.

[116] C. T. Nguyen, H. Phung, H. Jung, U. Kim, T. D. Nguyen, J. Park, H. Moon, J. C. Koo, and H. R. Choi, "Printable monolithic hexapod robot driven by soft actuator," in *2015 IEEE International Conference on Robotics and Automation (ICRA)*, pp. 4484–4489, IEEE, 2015.

[117] M. Duduta, D. R. Clarke, and R. J. Wood, "A high speed soft robot based on dielectric elastomer actuators," in *2017 IEEE International Conference on Robotics and Automation (ICRA)*, pp. 4346–4351, IEEE, 2017.

[118] K. M. Digumarti, C. Cao, J. Guo, A. T. Conn, and J. Rossiter, "Multi-directional crawling robot with soft actuators and electroadhesive grippers," in *2018 IEEE International Conference on Soft Robotics (RoboSoft)*, pp. 303–308, IEEE, 2018.

[119] M. Kovač, "The bioinspiration design paradigm: A perspective for soft robotics," *Soft Robotics*, vol. 1, no. 1, pp. 28–37, 2014.

[120] V. Vikas, P. Grover, and B. Trimmer, "Model-free control framework for multi-limb soft robots," *IEEE International Conference on Intelligent Robots and Systems*, vol. 2015-December, pp. 1111–1116, 2015.

[121] D. Navarro-Alarcón, Y.-H. Liu, J. G. Romero, and P. Li, "Model-free visually servoed deformation control of elastic objects by robot manipulators," *IEEE Transactions on Robotics*, vol. 29, no. 6, pp. 1457–1468, 2013.

[122] G. Soter, A. T. Conn, H. Hauser, and J. Rossiter, "Bodily aware soft robots: Integration of proprioceptive and exteroceptive sensors," *IEEE International Conference on Robotics and Automation*, 2018.

[123] P. E. Lestrel, *Fourier descriptors and their applications in biology*. Cambridge University Press, 2008.

[124] F. P. Kuhl and C. R. Giardina, "Elliptic Fourier features of a closed contour," *Computer graphics and image processing*, vol. 18, no. 3, pp. 236–258, 1982.

[125] G. Diaz, A. Zuccarelli, I. Pelligra, and A. Ghiani, "Elliptic Fourier analysis of cell and nuclear shapes," *Computers and biomedical research*, vol. 22, no. 5, pp. 405–414, 1989.

[126] S. Ferson, F. J. Rohlf, and R. K. Koehn, "Measuring shape variation of two-dimensional outlines," *Systematic Biology*, vol. 34, no. 1, pp. 59–68, 1985.

[127] N. Furuta, S. Ninomiya, N. Takahashi, H. Ohmori, and U. Yasuo, "Quantitative evaluation of soybean (Glycine max L. Merr.) leaflet shape by principal component scores based on elliptic Fourier descriptor," *Japanese Journal of Breeding*, vol. 45, no. 3, pp. 315–320, 1995.

[128] H. Iwata, S. Niikura, S. Matsuura, Y. Takano, and Y. Ukai, "Evaluation of variation of root shape of Japanese radish (Raphanus sativus L.) based on image analysis using elliptic Fourier descriptors," *Euphytica*, vol. 102, no. 2, pp. 143–149, 1998.

[129] P. E. Lestrel, D. W. Read, and C. Wolfe, "Size and shape of the rabbit orbit: 3-D Fourier descriptors," *Fourier descriptors and their applications in biology*, pp. 359–378, 1997.

[130] J. E. Godefroy, F. Bornert, C. I. Gros, and A. Constantinesco, "Elliptical Fourier descriptors for contours in three dimensions: a new tool for morphometrical analysis in biology," *Comptes rendus biologies*, vol. 335, no. 3, pp. 205–213, 2012.

[131] H. Freeman, "Computer processing of line-drawing images," *ACM Computing Surveys (CSUR)*, vol. 6, no. 1, pp. 57–97, 1974.

[132] A. Adebowale, A. Nicholas, J. Lamb, and Y. Naidoo, "Elliptic Fourier analysis of leaf shape in southern African Strychnos section Densiflorae (Loganiaceae)," *Botanical Journal of the Linnean Society*, vol. 170, no. 4, pp. 542–553, 2012.

[133] G. Haase, "Studien über Euglena sanguinea," *Arch. Protistenk*, vol. 20, pp. 47–59, 1910.

[134] M. Chadefaud and L. Provasoli, "Une nouvelle euglene graciloide: Euglena gracilis Klebs var. urophora n. var," *Arch. Zool. Exp. Gén*, vol. 80, pp. 55–60, 1939.

[135] P.-A. Dangeard, *Recherches sur les Eugléniens*. Direction du Botaniste, 1902.

[136] B. Trimmer and J. Issberner, "Kinematics of soft-bodied, legged locomotion in Manduca sexta larvae," *Biological Bulletin*, vol. 212, no. 2, pp. 130–142, 2007.

[137] H. T. Lin and B. A. Trimmer, "The substrate as a skeleton: ground reaction forces from a soft-bodied legged animal," *Journal of Experimental Biology*, vol. 213, no. 7, pp. 1133–1142, 2010.

[138] M. A. Simon, W. A. Woods Jr, Y. V. Serebrenik, S. M. Simon, L. I. van Griethuijsen, J. J. Socha, W.-K. Lee, and B. A. Trimmer, "Visceral-locomotory pistoning in crawling caterpillars," *Current biology*, vol. 20, no. 16, pp. 1458–1463, 2010.

[139] Y. Elsayed, A. Vincensi, C. Lekakou, T. Geng, C. Saaj, T. Ranzani, M. Cianchetti, and A. Menciassi, "Finite element analysis and design optimization of a pneumatically actuating silicone module for robotic surgery applications," *Soft Robotics*, vol. 1, no. 4, pp. 255–262, 2014.

[140] A. Gambaruto, D. Taylor, and D. Doorly, "Decomposition and description of the nasal cavity form," *Annals of biomedical engineering*, vol. 40, no. 5, pp. 1142–1159, 2012.

[141] W. M. Kier, "The diversity of hydrostatic skeletons," *Journal of Experimental Biology*, vol. 215, no. 8, pp. 1247–1257, 2012.

[142] A. S. Boxerbaum, K. M. Shaw, H. J. Chiel, and R. D. Quinn, "Continuous wave peristaltic motion in a robot," *The international journal of Robotics Research*, vol. 31, no. 3, pp. 302–318, 2012.

[143] A. D. Horchler, A. Kandhari, K. A. Daltorio, *et al.*, "Worm-like robotic locomotion with a compliant modular mesh," in *Conference on Biomimetic and Biohybrid Systems*, pp. 26–37, Springer, 2015.

[144] M. Cianchetti, A. Licofonte, M. Follador, *et al.*, "Bioinspired soft actuation system using shape memory alloys," in *Actuators*, vol. 3, pp. 226–244, Multidisciplinary Digital Publishing Institute, 2014.

[145] C. D. Onal, R. J. Wood, and D. Rus, "An origami-inspired approach to worm robots," *IEEE/ASME Transactions on Mechatronics*, vol. 18, no. 2, pp. 430–438, 2013.

[146] R. V. Martinez, C. R. Fish, X. Chen, and G. M. Whitesides, "Elastomeric origami: programmable paper-elastomer composites as pneumatic actuators," *Advanced functional materials*, vol. 22, no. 7, pp. 1376–1384, 2012.

[147] A. T. Conn, A. D. Hinitt, and P. Wang, "Soft segmented inchworm robot with dielectric elastomer muscles," in *SPIE Smart Structures and Materials+ Nondestructive Evaluation and Health Monitoring*, p. 90562, International Society for Optics and Photonics, 2014.

[148] F. Carpi, G. Frediani, and D. De Rossi, "Hydrostatically coupled dielectric elastomer actuators," *IEEE/ASME Transactions On Mechatronics*, vol. 15, no. 2, pp. 308–315, 2010.

[149] R. Pelrine, R. Kornbluh, Q. Pei, and J. Joseph, "High-speed electrically actuated elastomers with strain greater than 100%," *Science*, vol. 287, no. 5454, pp. 836–839, 2000.

[150] A. J. Liu and S. R. Nagel, "Nonlinear dynamics: Jamming is not just cool any more," *Nature*, vol. 396, no. 6706, pp. 21–22, 1998.

[151] E. Steltz, A. Mozeika, N. Rodenberg, E. Brown, and H. M. Jaeger, "Jsel: Jamming skin enabled locomotion," in *Intelligent Robots and Systems, 2009. IROS 2009. IEEE/RSJ International Conference on*, pp. 5672–5677, IEEE, 2009.

[152] F. Ilievski, A. D. Mazzeo, R. F. Shepherd, X. Chen, and G. M. Whitesides, "Soft robotics for chemists," *Angewandte Chemie*, vol. 123, no. 8, pp. 1930–1935, 2011.

[153] K. Ogura, S. Wakimoto, K. Suzumori, and Y. Nishioka, "Micro pneumatic curling actuator-nematode actuator," in *Robotics and Biomimetics, ROBIO 2008. IEEE International Conference on*, pp. 462–467, 2008.

[154] B. Mosadegh, P. Polygerinos, C. Keplinger, *et al.*, "Pneumatic networks for soft robotics that actuate rapidly," *Advanced Functional Materials*, vol. 24, no. 15, pp. 2163–2170, 2014.

[155] K. M. Digumarti, A. T. Conn, and J. Rossiter, "Euglenoid-inspired giant shape change for highly deformable soft robots," *IEEE Robotics and Automation Letters*, vol. 2, no. 4, pp. 2302–2307, 2017.

[156] M. A. Robertson and J. Paik, "New soft robots really suck: Vacuum-powered systems empower diverse capabilities," *Science Robotics*, vol. 2, no. 9, p. eaan6357, 2017.

[157] D. Yang, M. S. Verma, J.-H. So, B. Mosadegh, C. Keplinger, B. Lee, F. Khashai, E. Lossner, Z. Suo, and G. M. Whitesides, "Buckling pneumatic linear actuators inspired by muscle," *Advanced Materials Technologies*, vol. 1, no. 3, p. 1600055, 2016.

[158] M. Cianchetti, T. Ranzani, G. Gerboni, *et al.*, "Stiff-flop surgical manipulator: mechanical design and experimental characterization of the single module," in *Intelligent Robots and Systems (IROS), 2013 IEEE/RSJ International Conference on*, pp. 3576–3581, IEEE, 2013.

[159] R. F. Shepherd, A. A. Stokes, R. Nunes, and G. M. Whitesides, "Soft machines that are resistant to puncture and that self seal," *Advanced Materials*, vol. 25, no. 46, pp. 6709–6713, 2013.

[160] K. M. Digumarti in *Euglenoid-inspired giant shape change for highly deformable soft robots. Master's Thesis.*, Bristol: University of Bristol, 2016.

[161] G. Udupa, P. Sreedharan, P. Sai Dinesh, and D. Kim, "Asymmetric bellow flexible pneumatic actuator for miniature robotic soft gripper," *Journal of Robotics*, 2014.

[162] O. H. Yeoh, "Some forms of the strain energy function for rubber," *Rubber Chemistry and technology*, vol. 66, no. 5, pp. 754–771, 1993.

[163] Y. Elsayed, A. Vincensi, C. Lekakou, *et al.*, "Finite element analysis and design optimization of a pneumatically actuating silicone module for robotic surgery applications," *Soft Robotics*, vol. 1, no. 4, pp. 255–262, 2014.

[164] D. Merritt and F. Weinhaus, "The pressure curve for a rubber balloon," *American Journal of Physics*, vol. 46, no. 10, pp. 976–977, 1978.

[165] K. M. Digumarti, A. T. Conn, and J. Rossiter, "Eumobot: replicating euglenoid movement in a soft robot," *Journal of the Royal Society Interface*, vol. 15, no. 148, p. 20180301, 2018.

[166] M. H. Dickinson, F.-O. Lehmann, and S. P. Sane, "Wing rotation and the aerodynamic basis of insect flight," *Science*, vol. 284, no. 5422, pp. 1954–1960, 1999.

[167] T. McMahon, "Size and shape in biology: elastic criteria impose limits on biological proportions, and consequently on metabolic rates," *Science*, vol. 179, no. 4079, pp. 1201–1204, 1973.

[168] M. Holwill, "Physical aspects of flagellar movement," *Physiological Reviews*, vol. 46, no. 4, pp. 696–785, 1966.

[169] M. Wehner, R. L. Truby, D. J. Fitzgerald, B. Mosadegh, G. M. Whitesides, J. A. Lewis, and R. J. Wood, "An integrated design and fabrication strategy for entirely soft, autonomous robots," *Nature*, vol. 536, no. 7617, p. 451, 2016.

[170] R. Vaidyanathan, H. J. Chiel, and R. D. Quinn, "A hydrostatic robot for marine applications," *Robotics and Autonomous Systems*, vol. 30, no. 1-2, pp. 103–113, 2000.

[171] A. D. Marchese, R. K. Katzschmann, and D. Rus, "Whole arm planning for a soft and highly compliant 2D robotic manipulator," in *Intelligent Robots and Systems (IROS 2014), 2014 IEEE/RSJ International Conference on*, pp. 554–560, IEEE, 2014.

[172] K. M. Digumarti, A. Conn, and J. Rossiter, "Pellicular morphing surfaces for soft robots," *IEEE Robotics and Automation Letters*, vol. 4, no. 3, pp. 2304–2309, 2019.

[173] H. Silverman and R. S. Hikida, "Pellicle complex of Euglena gracilis: Characterization by disruptive treatments," *Protoplasma*, vol. 87, no. 1-3, pp. 237–252, 1976.

[174] D. Buetow, "The biology of euglena, vol. 3," *Physiology*, 1982.

[175] J. Dumais, "Modes of deformation of walled cells," *Journal of experimental botany*, vol. 64, no. 15, pp. 4681–4695, 2013.

[176] S. Sareh, J. Rossiter, A. Conn, K. Drescher, and R. E. Goldstein, "Swimming like algae: biomimetic soft artificial cilia," *Journal of the Royal Society Interface*, vol. 10, no. 78, p. 20120666, 2013.

[177] J. Wu, Y. Mizuno, M. Tabaru, and K. Nakamura, "Ultrasonic motors with polymer-based vibrators," *IEEE transactions on ultrasonics, ferroelectrics, and frequency control*, vol. 62, no. 12, pp. 2169–2178, 2015.

[178] A. D. Poole, J. D. Booker, C. L. Wishart, N. McNeill, and P. H. Mellor, "Performance of a prototype traveling-wave actuator made from a dielectric elastomer," *IEEE/ASME Transactions on Mechatronics*, vol. 17, no. 3, pp. 525–533, 2012.

[179] M. Taghavi, T. Helps, and J. Rossiter, "Electro-ribbon actuators and electro-origami robots," *Science Robotics*, vol. 3, no. 25, p. eaau9795, 2018.

[180] E. Acome, S. Mitchell, T. Morrissey, M. Emmett, C. Benjamin, M. King, M. Radakovitz, and C. Keplinger, "Hydraulically amplified self-healing electrostatic actuators with muscle-like performance," *Science*, vol. 359, no. 6371, pp. 61–65, 2018.

[181] A. Miriyev, K. Stack, and H. Lipson, "Soft material for soft actuators," *Nature communications*, vol. 8, no. 1, p. 596, 2017.

[182] "Desmopan 2786A." . https://www.tpu.covestro.com/en/Products/Desmopan/ProductList/201304281603/Desmopan-DP-2786A. Accessed: 08.12.18.

[183] M. Lefort-Tran, M. Bre, J. Ranck, and M. Pouphile, "Euglena plasma membrane during normal and vitamin B12 starvation growth," *Journal of cell science*, vol. 41, no. 1, pp. 245–261, 1980.

[184] G. Noselli, M. Arroyo, and A. DeSimone, "Smart helical structures inspired by the pellicle of euglenids," *Journal of the Mechanics and Physics of Solids*, vol. 123, pp. 234–246, 2019.

[185] M. Arroyo and A. DeSimone, "Shape control of active surfaces inspired by the movement of euglenids," *Journal of the Mechanics and Physics of Solids*, vol. 62, pp. 99–112, 2014.

[186] S. Mintchev and D. Floreano, "Adaptive morphology: A design principle for multimodal and multifunctional robots," *IEEE Robotics & Automation Magazine*, vol. 23, no. 3, pp. 42–54, 2016.

[187] D. Yang, B. Mosadegh, A. Ainla, B. Lee, F. Khashai, Z. Suo, K. Bertoldi, and G. M. Whitesides, "Buckling of elastomeric beams enables actuation of soft machines," *Advanced Materials*, vol. 27, no. 41, pp. 6323–6327, 2015.

[188] S. Li, D. M. Vogt, D. Rus, and R. J. Wood, "Fluid-driven origami-inspired artificial muscles," *Proceedings of the National Academy of Sciences*, vol. 114, no. 50, pp. 13132–13137, 2017.

[189] M. S. Verma, A. Ainla, D. Yang, D. Harburg, and G. M. Whitesides, "A soft tube-climbing robot," *Soft robotics*, vol. 5, no. 2, pp. 133–137, 2018.

[190] E. Siéfert, E. Reyssat, J. Bico, and B. Roman, "Bio-inspired pneumatic shape-morphing elastomers," *Nature materials*, vol. 18, no. 1, p. 24, 2019.

[191] D. Navarro-Alarcon and Y.-H. Liu, "Fourier-based shape servoing: A new feedback method to actively deform soft objects into desired 2-D image contours," *IEEE Transactions on Robotics*, vol. 34, no. 1, pp. 272–279, 2018.

[192] K. Ghazi-Zahedi, R. Deimel, G. Montúfar, V. Wall, and O. Brock, "Morphological computation: The good, the bad, and the ugly," in *Proceedings of the IEEE/RSJ International Conference on Intelligent Robots and Systems, Vancouver, BC, Canada*, pp. 24–28, 2017.

[193] M. T. Tolley, R. F. Shepherd, M. Karpelson, N. W. Bartlett, K. C. Galloway, M. Wehner, R. Nunes, G. M. Whitesides, and R. J. Wood, "An untethered jumping soft robot," in *2014 IEEE/RSJ International Conference on Intelligent Robots and Systems*, pp. 561–566, IEEE, 2014.

[194] N. W. Bartlett, M. T. Tolley, J. T. Overvelde, J. C. Weaver, B. Mosadegh, K. Bertoldi, G. M. Whitesides, and R. J. Wood, "A 3D-printed, functionally graded soft robot powered by combustion," *Science*, vol. 349, no. 6244, pp. 161–165, 2015.

[195] C. D. Onal, X. Chen, G. M. Whitesides, and D. Rus, "Soft mobile robots with on-board chemical pressure generation," in *Robotics Research*, pp. 525–540, Springer, 2017.

[196] B. Mosadegh, C.-H. Kuo, Y.-C. Tung, Y.-s. Torisawa, T. Bersano-Begey, H. Tavana, and S. Takayama, "Integrated elastomeric components for autonomous regulation of sequential and oscillatory flow switching in microfluidic devices," *Nature physics*, vol. 6, no. 6, p. 433, 2010.

[197] Y. Liu and H. Hu, "A review on auxetic structures and polymeric materials," *Scientific Research and Essays*, vol. 5, no. 10, pp. 1052–1063, 2010.

[198] H. A. Kolken and A. A. Zadpoor, "Auxetic mechanical metamaterials," *RSC Adv.*, vol. 7, pp. 5111–5129, 2017.

[199] C. S. Kaplan, *Introductory Tiling Theory for Computer Graphics*. Morgan and Claypool Publishers, 2009.

[200] C. Schumacher, S. Marschner, M. Cross, and B. Thomaszewski, "Mechanical characterization of structured sheet materials," *ACM Trans. Graph.*, vol. 37, pp. 148:1–148:15, July 2018.

[201] H. Qi and M. Boyce, "Stressstrain behavior of thermoplastic polyurethanes," *Mechanics of Materials*, vol. 37, no. 8, pp. 817 – 839, 2005.

[202] A. Rafsanjani, Y. Zhang, B. Liu, S. M. Rubinstein, and K. Bertoldi, "Kirigami skins make a simple soft actuator crawl," *Science Robotics*, vol. 3, no. 15, p. eaar7555, 2018.

[203] H. Choi, K. M. Jung, J. Kwak, S. Lee, H. Kim, J. W. Jeon, and J. Nam, "Digital polymer motor for robotic applications," in *2003 IEEE International Conference on Robotics and Automation (Cat. No. 03CH37422)*, vol. 2, pp. 1857–1862, IEEE, 2003.

[204] J. Guo, T. Bamber, T. Hovell, M. Chamberlain, L. Justham, and M. Jackson, "Geometric optimisation of electroadhesive actuators based on 3d electrostatic simulation and its experimental verification," *IFAC-PapersOnLine*, vol. 49, no. 21, pp. 309–315, 2016.

[205] J. Germann, B. Schubert, and D. Floreano, "Stretchable electroadhesion for soft robots," in *2014 IEEE/RSJ International Conference on Intelligent Robots and Systems*, pp. 3933–3938, Ieee, 2014.

[206] X. Gao, C. Cao, J. Guo, and A. Conn, "Elastic electroadhesion with rapid release by integrated resonant vibration," *Advanced Materials Technologies*, vol. 4, no. 1, p. 1800378, 2019.

[207] M. Duduta, R. J. Wood, and D. R. Clarke, "Multilayer dielectric elastomers for fast, programmable actuation without prestretch," *Advanced Materials*, vol. 28, no. 36, pp. 8058–8063, 2016.

[208] P. Wang and A. Conn, "Elastic cube actuator with six degrees of freedom output," in *Actuators*, vol. 4, pp. 203–216, Multidisciplinary Digital Publishing Institute, 2015.

[209] A. Gent, "A new constitutive relation for rubber," *Rubber chemistry and technology*, vol. 69, no. 1, pp. 59–61, 1996.

[210] Y. Wang, B. Chen, Y. Bai, H. Wang, and J. Zhou, "Actuating dielectric elastomers in pure shear deformation by elastomeric conductors," *Applied Physics Letters*, vol. 104, no. 6, p. 064101, 2014.

[211] C. Chiang Foo, S. Cai, S. Jin Adrian Koh, S. Bauer, and Z. Suo, "Model of dissipative dielectric elastomers," *Journal of Applied Physics*, vol. 111, no. 3, p. 034102, 2012.

[212] C. Zhang, H. Chen, L. Liu, and D. Li, "Modelling and characterization of inflated dielectric elastomer actuators with tubular configuration," *Journal of Physics D: Applied Physics*, vol. 48, no. 24, p. 245502, 2015.

[213] J. Guo, M. Tailor, T. Bamber, M. Chamberlain, L. Justham, and M. Jackson, "Investigation of relationship between interfacial electroadhesive force and surface texture," *Journal of Physics D: Applied Physics*, vol. 49, no. 3, p. 035303, 2015.

[214] J. Guo, T. Bamber, M. Chamberlain, L. Justham, and M. Jackson, "Optimization and experimental verification of coplanar interdigital electroadhesives," *Journal of Physics D: Applied Physics*, vol. 49, no. 41, p. 415304, 2016.

[215] J. Guo, T. Bamber, J. Petzing, L. Justham, and M. Jackson, "Experimental study of relationship between interfacial electroadhesive force and applied voltage for different substrate materials," *Applied Physics Letters*, vol. 110, no. 5, p. 051602, 2017.

[216] V. Carneiro, J. Meireles, and H. Puga, "Auxetic materials A review," *Materials Science-Poland*, vol. 31, pp. 561–571, 10 2013.

[217] R. Pfeifer and J. Bongard, *How the body shapes the way we think: a new view of intelligence*. MIT press, 2006.

Appendix A

Kinematic Model of the Pellicle

This section presents additional details related to the kinematic model of the pellicle [69] which were omitted in the main text.

Cauchy-Green Deformation Tensor for Simple Shear

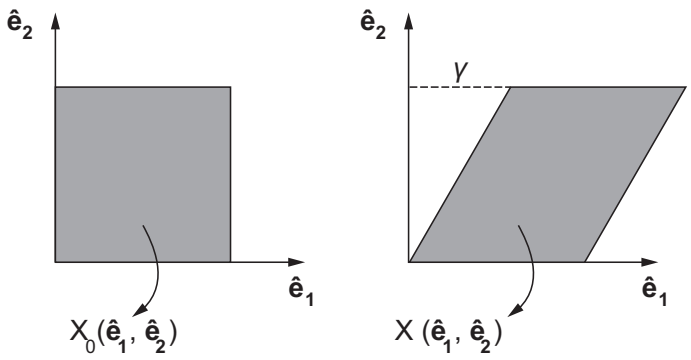

Figure A1: Illustration of simple shear.

Consider the case of a simple shear deformation as illustrated in fig. A1. Let us assume that the deformation happens in the $\hat{\mathbf{e_1}} - \hat{\mathbf{e_2}}$ plane along the $\hat{\mathbf{e_1}}$ direction (lines along $\hat{\mathbf{e_1}}$ do not change in length). The magnitude of shear is γ. Let $\mathbf{X}_0\left(\hat{\mathbf{e_1}}, \hat{\mathbf{e_2}}\right)$ represent the initial configuration and $\mathbf{X}\left(\hat{\mathbf{e_1}}, \hat{\mathbf{e_2}}\right)$ be the deformed configuration. The relation between these can be given as follows.

$$\mathbf{X}_0 = \begin{Bmatrix} x \\ y \\ z \end{Bmatrix} \quad , \quad \mathbf{X} = \begin{Bmatrix} x + \gamma y \\ y \\ z \end{Bmatrix}. \tag{1}$$

The deformation gradient can then be given as

$$\mathbf{F} = \frac{\partial \mathbf{X}}{\partial \mathbf{X}_0} = \begin{bmatrix} 1 & \gamma & 0 \\ 0 & 1 & 0 \\ 0 & 0 & 1 \end{bmatrix} = \begin{bmatrix} 1 & 0 & 0 \\ 0 & 1 & 0 \\ 0 & 0 & 1 \end{bmatrix} + \gamma \begin{bmatrix} 0 & 1 & 0 \\ 0 & 0 & 0 \\ 0 & 0 & 0 \end{bmatrix} = \mathrm{I} + \gamma \hat{\mathbf{e_1}} \otimes \hat{\mathbf{e_2}}. \tag{2}$$

In the case of the pellicle strips, shear happens in the $\mathbf{s_0} - \mathbf{m_0}$ plane and along $\mathbf{s_0}$ (fig. 5.2d). The deformation gradient can therefore be written as

$$\mathbf{F} = \mathrm{R}\left(\mathrm{I} + \gamma\left(\mathbf{s_0} \otimes \mathbf{m_0}\right)\right) = \mathrm{R}\left(\mathrm{I} + \gamma\left(\mathbf{s_0}\mathbf{m_0}^\top\right)\right), \tag{3}$$

where R is an undetermined rotation. This can be eliminated by computing the Cauchy-Green deformation tensor.

$$\begin{aligned}
\mathbf{C} &= \mathbf{F}^\top\mathbf{F} \\
&= \left[\mathrm{R}\left(\mathrm{I} + \gamma\left(\mathbf{s_0}\mathbf{m_0}^\top\right)\right)\right]^\top\left[\mathrm{R}\left(\mathrm{I} + \gamma\left(\mathbf{s_0}\mathbf{m_0}^\top\right)\right)\right] \\
&= \left(\mathrm{I} + \gamma\left(\mathbf{s_0}\mathbf{m_0}^\top\right)\right)^\top \mathrm{R}^\top\mathrm{R}\left(\mathrm{I} + \gamma\left(\mathbf{s_0}\mathbf{m_0}^\top\right)\right) \\
&= \left(\mathrm{I} + \gamma\mathbf{m_0}\mathbf{s_0}^\top\right)\left(\mathrm{I} + \gamma\mathbf{s_0}\mathbf{m_0}^\top\right) \\
&= \mathrm{I} + \gamma\mathbf{s_0}\mathbf{m_0}^\top + \gamma\mathbf{m_0}\mathbf{s_0}^\top + \gamma^2\mathbf{m_0}\mathbf{s_0}^\top\mathbf{s_0}\mathbf{m_0}^\top \\
&= I + \gamma\left(\mathbf{s_0}\mathbf{m_0}^\top + \mathbf{m_0}\mathbf{s_0}^\top\right) + \gamma^2\mathbf{m_0}\mathbf{m_0}^\top \\
&= \begin{bmatrix} 1 - \gamma\sin 2\alpha_0 + \gamma^2\cos\alpha_0 & -\gamma\cos 2\alpha_0 - \gamma^2\sin\alpha_0\cos\alpha_0 \\ -\gamma\cos 2\alpha_0 - \gamma^2\sin\alpha_0\cos\alpha_0 & 1 + \gamma\sin 2\alpha_0 + \gamma^2\sin^2\alpha_0 \end{bmatrix}.
\end{aligned} \tag{4}$$

Relation Between $r_0(\lambda)$ and $z_0(\lambda)$

The total surface area S is constant. By definition of λ, the relation between $r_0(\lambda)$ and $z_0(\lambda)$ is given as

$$\lambda S = 2\pi\int_0^\lambda \sqrt{r_{0_\lambda}^2(v) + z_{0_\lambda}^2(v)}\ r_0(v)dv. \tag{5}$$

Differentiate the above equation with respect to λ to obtain

$$z_{0_\lambda}(\lambda) = \sqrt{\left(\frac{S}{2\pi r_0(\lambda)}\right)^2 - r_{0_\lambda}(\lambda)}. \tag{6}$$

This expression can be integrated with respect to λ to obtain $z_0(\lambda)$.

Appendix B

Tiled Auxetic Cylinders

Based on work presented at the following peer reviewed venue.

> Simons MF, **Digumarti KM**, Conn AT, Rossiter J. Tiled Auxetic Cylinders for Soft Robots. 2019 *IEEE International Conference on Soft Robotics (RoboSoft)*. 2019 April 14 (pp. 62-67). IEEE.
>
> *Contribution statement: All the authors were involved in conceptualisation of design, planning of experiments and writing the final manuscript. Simons MF fabricated the structures. Simons MF and Digumarti KM performed the experiments, analysed the data and wrote the first draft. Simons MF and Digumarti KM are joint first authors.*

This section details the design, fabrication and experimental characterisation of auxetic structures which have a cylindrical shape. These are termed tiled auxetic cylinders (TACs) [91] and were introduced in section 2.5 as soft meta-materials capable of generating tunable mechanical response to elongation. The force required to stretch the structure in length and the corresponding change in diameter were experimentally determined. Comparisons between the four designs are made with respect to these properties.

Design and Fabrication

The four auxetic designs belong to a class of patterns called re-entrant structures. The first two designs (A and B in fig. B1) are re-entrant sinusoids [197] and the second two (C and D in fig. B1) are re-entrant hexagons [198].

Both the re-entrant sinusoid designs belong to the same family of isohedral tiling [199], which can be described as a pattern of square tiles (fig. B2a). In other words, these patterns are formed by laying out squares on a 2D grid and replacing the edges with sinusoidal curves. The two patterns in this study are effectively the same design, the difference being that in the latter the points of rotation have been enlarged, which makes it stiffer than the simple re-entrant sinusoid (point P in fig. B2b). This design is referred to as a modified re-entrant sinusoid. The smallest repeating unit in the pattern is a pair of adjacent tiles oriented perpendicular to each other (fig. B2a).

The hexagonal designs are referred to as such because the basic repeating unit is a hexagon, instead of a square as in the earlier two designs. In this case, the tiles next to

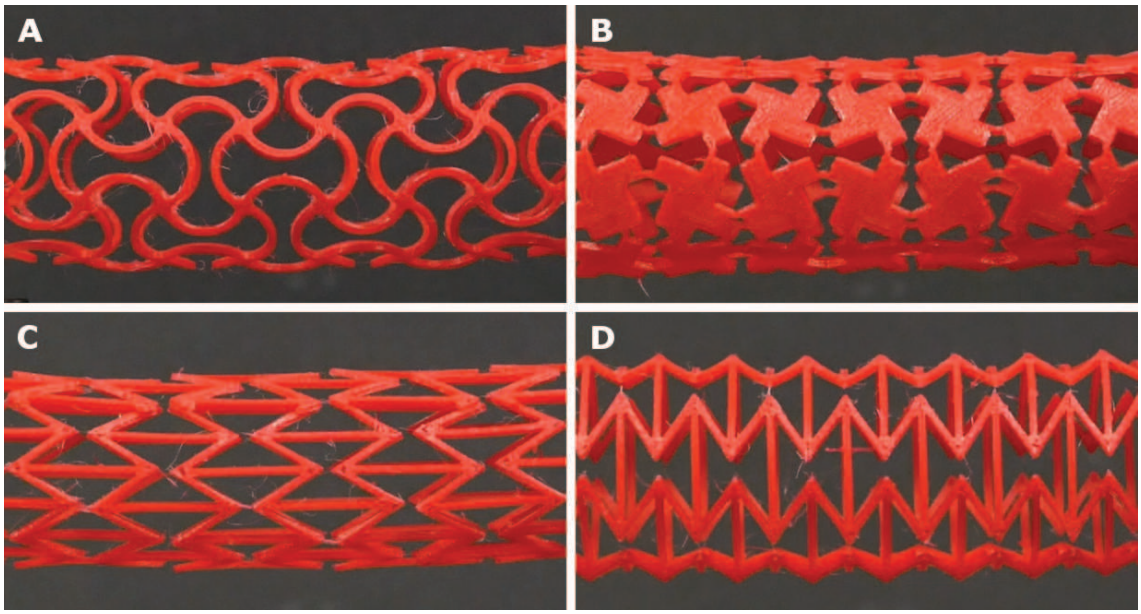

Figure B1: The four auxetic designs studied are (A) re-entrant sinusoid, (B) modified re-entrant sinusoid, (C) re-entrant hexagon oriented along the axis and (D) re-entrant hexagon oriented perpendicular to the axis.

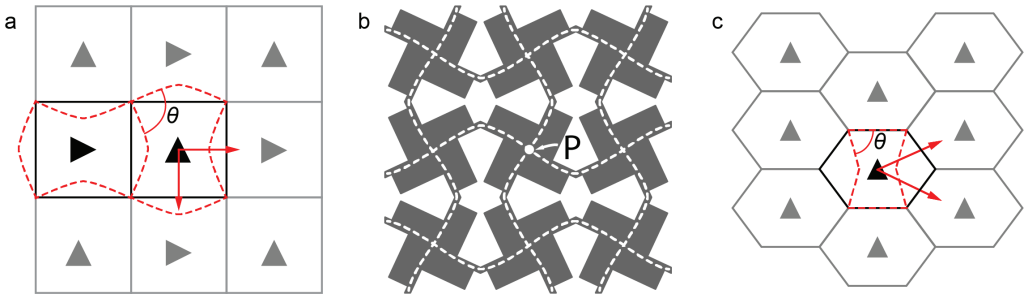

Figure B2: (a) Isohedral tiling pattern with square tiles. Triangles indicate orientation of tiles. Arrows indicate tiling directions. Dotted line shows a re-entrant sinusiod on the minimal repeating unit. (b) Re-entrant sinusoid (dotted line) overlaid on the modified re-entrant sinusoid (grey) showing that both the structures belong to the same isohedral tiling family. The point P that is common to four neighbouring tiles is the point of rotation. (c) Isohedral tiling pattern with hexagonal tiles. In this case, all the tiles have the same orientation. The re-entrant hexagon is shown with a dotted line. θ denotes the re-entrant angle. [91] © 2019 IEEE

each other are in the same orientation and not at 90° to each other (fig. B2c), which was the case in the sinusoidal patterns. The difference between the two hexagonal designs is the orientation of the pattern described in terms of the angle that the parallel rods of the patterns make with the longitudinal axis of the cylinder. In one case, the pattern is oriented along the axis of the cylinder (C in fig. B1) and in the other, it is oriented perpendicular to the axis (D in fig. B1).

These particular designs have been selected to illustrate the change in mechanical properties arising due to three key aspects of the design: the type of pattern used (A,B and C,D), the geometry for a given pattern (A, B) and the orientation of the pattern (C, D). Several other patterns such as arrowhead shapes [90], stars [92] and chiral geometries [88, 90, 92] exist but were not considered.

To fabricate the auxetic structures, the patterns were 3D printed on a flat surface. Thermoplastic polyurethane (TPU from rigid.ink, Youngs modulus = 15.5MPa [200], Poisson's ratio = 0.48 [201], Shore A Hardness: 94A) was used. The thickness of the sheet was 1mm. These sheets were then rolled up into a cylindrical configuration and bonded with cyanoacrylate adhesive (Loctite superglue). The flexible nature of the material facilitated the construction of the 3D structure from a 2D sheet. Loops were printed on the free ends of the structure to enable easy clamping that was required for the characterisation experiments.

Experimental Characterisation

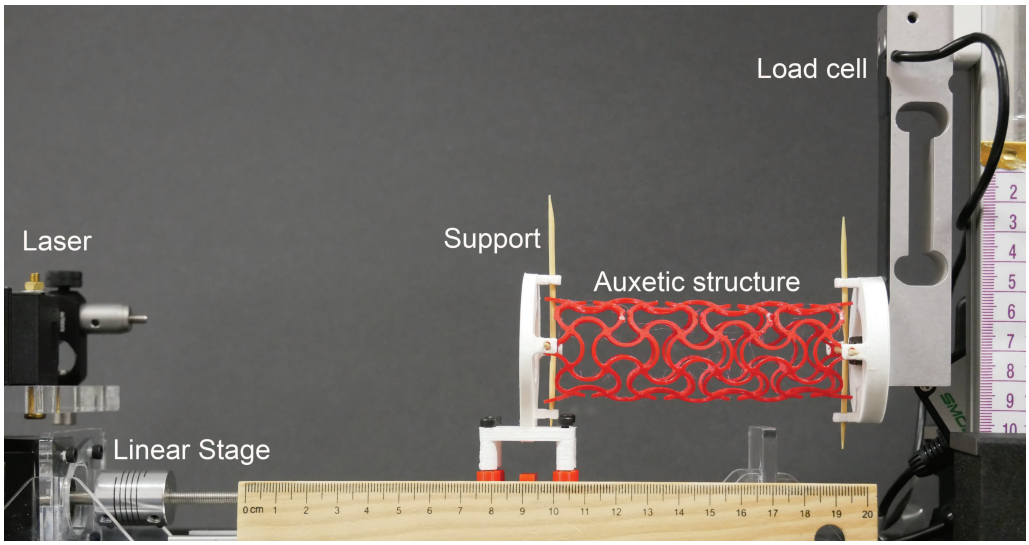

Figure B3: The experimental setup used to determine the relationship between elongation force and elongation in length of a cylindrical auxetic structure.

The TACs were characterised in terms of the relation between elongation force and length and the change in diameter with elongation. The structures were held in a linear stage with the longitudinal axis aligned in the direction of motion of the stage (fig. B3). One end of the cylinder was fixed to a load cell (Model no. 1022, Tedea-Huntleigh, max. load 5kg). The other end was attached to the movable carriage. As the carriage moved (at a constant rate of 0.45mm/s), an elongation in length was imposed on the structure. Care was taken to ensure that the diameter could change in an unconstrained manner. This was achieved using a pair of wooden dowels inserted into the loops at the ends of the structure. The use of the dowels constrained the rotation of the cylinder while allowing

the diameter to change.

A laser displacement sensor (LK-G512 and LKGD500, Keyence) was used to determine the position of the carriage. Both the elongation force and the displacement of the carriage were recorded using a data acquisition system (USB-6001, National Instruments) at a frequency of 1000Hz. The experiment was repeated 10 times for each design.

Each trial was recorded on video (DMC-G80, Panasonic) at a constant rate of 60fps. Individual frames from the video were then analysed in MATLAB using a computer vision program to extract the diameter of the complete structure (defined as the maximum span of a 2cm wide region in the middle of the structure) as it changed with its entire length.

Deformation of the Structure

A close up of the structure's deformation upon elongation is shown in fig. B4 for the four designs considered. In the case of the re-entrant sinusoids (A and B in fig. B4), the curved edges straightened out during elongation. This is immediately evident in the case of the second design by observing rotation of the square patches. In the third design, a three-dimensional buckling of the structure was observed. In the final design, curving of elements forming the re-entrant portion of the structure was seen.

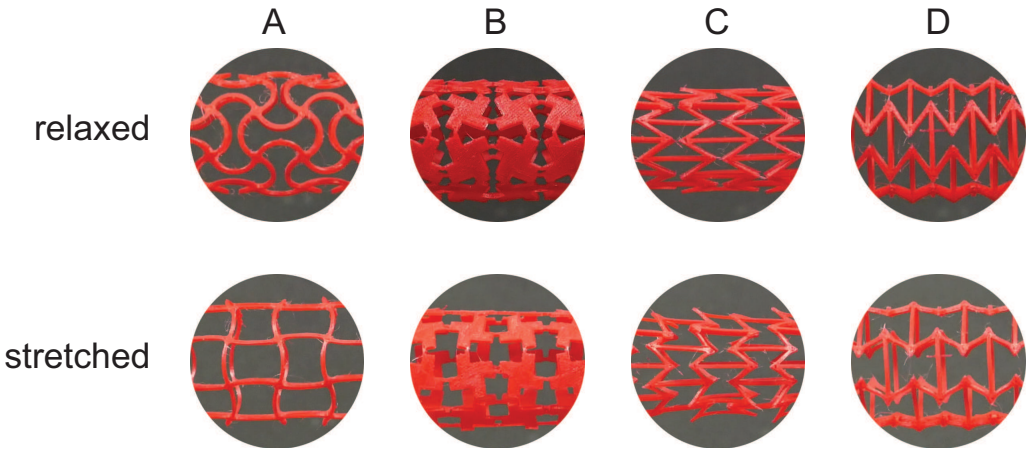

Figure B4: Configuration of the structure at rest (top) and after elongation (bottom) for the four designs considered: (A) re-entrant sinusoid, (B) modified re-entrant sinusoid, (C) re-entrant hexagon oriented along the axis and (D) re-entrant hexagon oriented perpendicular to the axis.

Force-Elongation Relationship

Figure B5 shows the relationship between elongation force and the elongation in length. This relation is a indication of the effective Young's modulus. In our results, we report elongation force instead of stress because of the limitation in determining the area of cross section, which changes as the structure elongates and the material stretches.

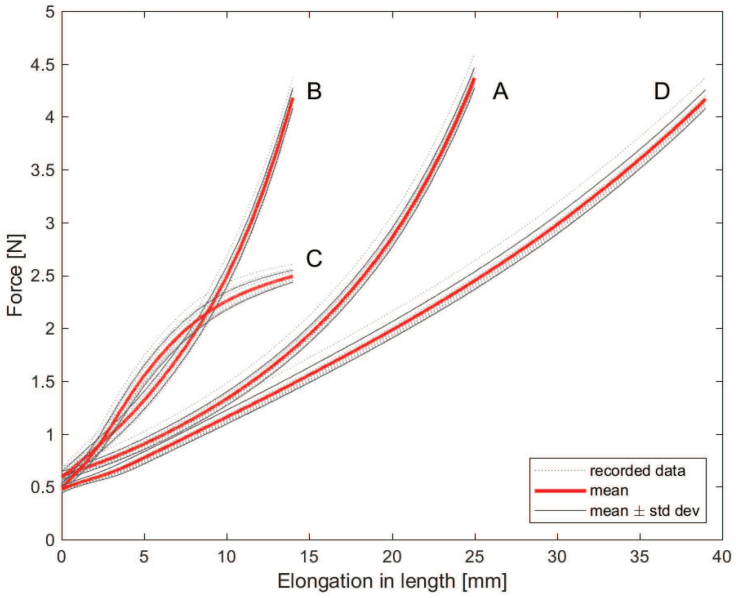

Figure B5: Relation between elongation force and elongation for the four auxetic designs considered: (A) re-entrant sinusoid, (B) modified re-entrant sinusoid, (C) re-entrant hexagon oriented along the axis and (D) re-entrant hexagon oriented perpendicular to the axis. The dotted lines indicate recorded data, the solid red line indicate the mean of 10 trials and the thin solid lines indicate one standard deviation away from the mean. [91]

The behaviour of the TACs showed some similarities as well as some differences. Both the sinusoidal designs exhibit stiffening upon elongation. The modified re-entrant sinusoid (B) shows more stiffening at a smaller elongation. This behaviour is expected since the points of rotation (P in fig. B2b) were designed to be stiffer as described in section 6.2. It may be deduced that structures with stiffness in the range between these two curves can be obtained by changing the amount of material at the points of rotation. The larger proportion of solid surface area in the modified re-entrant sinusiod (B) relative to (A), also highlights the potential for design control over relative areal porosity change during expansion. For example, a 10% extension in length generates a relative surface porosity increase of 12% in B and 5% in A.

The two re-entrant hexagonal structures (C and D in fig. B1), show very different behaviours even though they are the exact same structure. This is because of the orientation of the pattern on the structure. In the case of the pattern being oriented along the axis of the cylinder, an initial stiffening is observed followed by a softening of the structure. This could be attributed to the out of plane deformation (C in fig. B4 (bottom)) likely caused due to high stress concentration in the angular joints and the curving out of the structure to attain a minimal energy state. This is an interesting behaviour and can potentially be exploited for locomotion [202]. This is not observed in the other structures due to the nature of the design which provides a continuous path for force to transfer from one end to the other, thus preventing out of plane deformation. In the final case, the relation between force and elongation is approximately linear and closer to that of the sinusoids. A small degree of stiffening was observed at larger elongations. This is likely due to the deformation of the elements forming the re-entrant structure (inclined elements in D in fig. B4 (bottom)). The behaviour was similar in all the trials and the low standard deviation in data demonstrates that the behaviour is repeatable.

Interesting to note are the behavioural differences between the two tiling families. Elongation in structures A and B is due to the points of rotation (point P in fig. B2) where the re-entrant angle (θ in fig. B2) remains constant. Elongation of structures C and D however is due to a change in the re-entrant angle. There is scope for investigating this relationship between re-entrant angle and elongation of the structure in future work.

Diameter-Length Relationship

The relation between normalised change in diameter and normalised change in length was also determined. Figure B6 shows this relation in the four auxetic designs, which was found to be linear. The negative of the slope of the curves can be interpreted as an equivalent Poisson's ratio for the structures as it is describing a change in dimension perpendicular to that of extension (which is its definition for non-auxetic structures). These ratios are reported in table B1 and are comparable to those reported in [92]: -0.81 for the re-entrant sinusoid and -0.34 for the re-entrant hexagon when the orientation is perpendicular to the

axis. Elastomers, which are the predominant material used in soft robotics are considered to have a Poisson's ratio of approximately 0.5.

Both the sinusoidal designs (A and B) show similar behaviour as evidenced by the nearly overlapping curves in fig. B6. Their equivalent Poisson's ratio is close to -1 (table B1 A and B). The modified re-entrant sinusoid shows a smaller change in length and diameter, again due to its increased stiffness.

In the case of the re-entrant hexagons, the Poisson's ratios are very different. Pattern D demonstrates a large equivalent Poisson's ratio of approximately -2, approximately twice that of the re-entrant sinusoid structures. When the same structure is orientated at 90° (C), the equivalent Poisson's ratio is less than a quarter at -0.33.

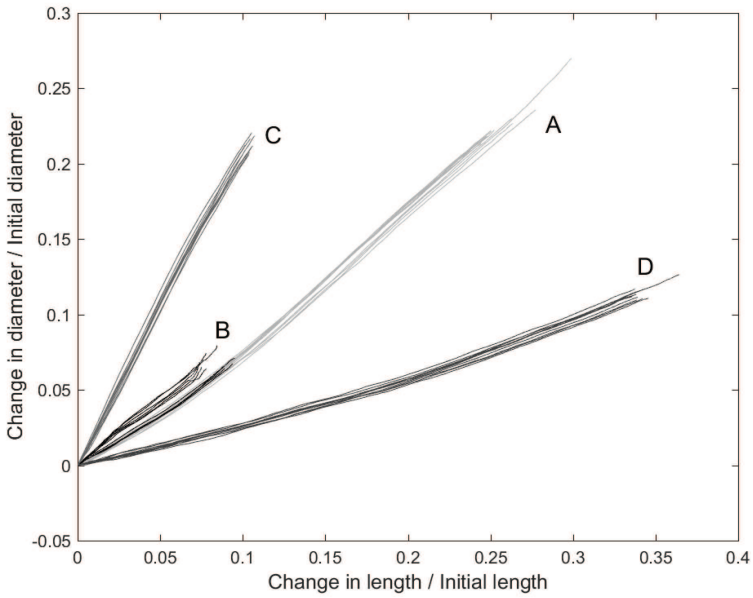

Figure B6: Relation between normalised change in diameter and normalised change in length for the four auxetic designs considered: (A) re-entrant sinusoid, (B) modified re-entrant sinusoid, (C) re-entrant hexagon oriented along the axis and (D) re-entrant hexagon oriented perpendicular to the axis. [91] © 2019 IEEE

Design	Equivalent Poisson's ratio
(A) Re-entrant sinusoid	-0.90 ± 0.01
(B) Modified re-entrant sinusoid	-0.76 ± 0.08
(C) Re-entrant hexagon ∥ axis	-2.09 ± 0.05
(D) Re-entrant hexagon ⊥ axis	-0.33 ± 0.01

Table B1: Equivalent Poisson's ratio for the four auxetic structures.

Comparison with other Actuators

The behaviour of the TACs can be compared to that of other classes of soft robotic structures. Here we revisit the illustration from section 4.4.3, comparing the conceptual relation between diameter and length for several common actuators: McKibben actuators, ideal balloon, standard bellows, hyperelastic bellows (HEB) and solid elastomers. This comparison is shown in fig. B7. The behaviour of the auxetic structure is linear and is similar to that of an ideal balloon. The slope of the curve can be tuned and various structures display varied magnitudes of steepness (fig. B6). Unlike in the case of the HEB, there is no region of decoupling between length and diameter. Both these dimensions increase or decrease simultaneously.

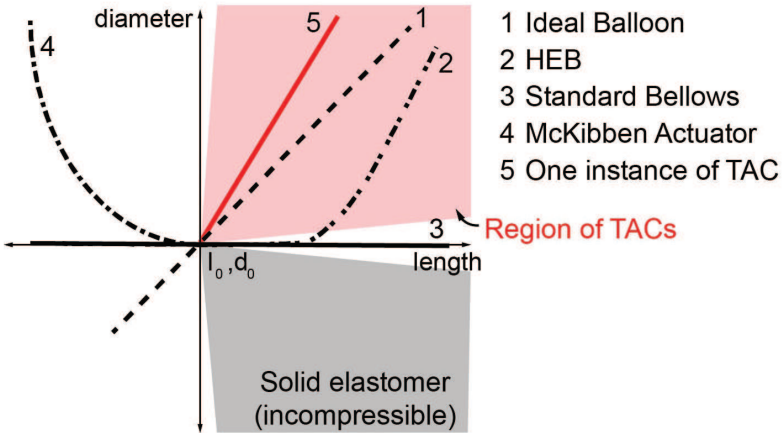

Figure B7: Comparison of TACs with various classes of structures showing the conceptual relation between diameter and length during actuation. All structures are assumed to have an initial length of l_o and diameter d_o. Adapted from [155].

Summary

In this work, we investigated TACs; a tiling based approach to the design of cylindrical auxetic structures. We focused on two particular designs, the re-entrant sinusoid and the re-entrant hexagon. We characterised the structures in terms of the elongation force and diameter as they change with elongation. Our analysis showed that a minor modification of the design within the same family of tiling can result in a significant difference in behaviour. In addition, we showed the emergence of variation in behaviour by simply altering the orientation of the pattern within the structure.

The tiling based approach is amenable to parametrisation This allows for tuning the design to achieve a desired mechanical response. Transition between multiple designs within the same structure (fig. B8) and the impact of this on mechanical properties is a possible study in future work. Regions with varying stiffness could potentially be created at specific locations on the structure leading to interesting and emergent macroscopic

behaviours. The rest configuration of the 3D printed structure affects its stiffness. The preference for a more contracted or more expanded configuration could be exploited in the design of a robot. This is another topic for investigation.

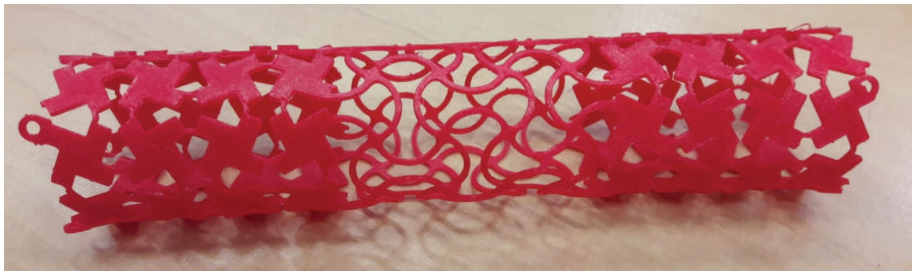

Figure B8: A version of the TAC with multiple auxetic patterns within the same structure.

Appendix C

Muscle-like Actuation in a Crawling Robot

Based on work presented at the following peer reviewed venue.

> **Digumarti KM**, Cao C, Conn AT, Rossiter J. Multi-directional crawling robot with soft actuators and electroadhesive grippers. 2018 *IEEE International Conference on Soft Robotics (RoboSoft)* 2018 Apr 24 (pp. 303-308). IEEE.
>
> *Contribution statement: All the authors were involved in planning of experiments and writing the final manuscript. Digumarti KM and Cao C conceptualised the design, fabricated the robot, performed the experiments, analysed the data and wrote the first draft. Digumarti KM and Cao C are joint first authors.*

The concept of a new muscle-like actuation mechanism for soft robots was introduced in chapter 2. This section details our work which implements the core concept in a crawling robot which uses a planar disk shaped design with DEAs arranged in multiple sectors. A major advantage of this configuration is the ability to move in many directions Generating relative motion is only one half of the solution to achieving locomotion. A method to generate anisotropic friction is necessary to cause a net displacement. Solutions ranging from bristles and pins to bio-inspired adhesives have been employed. A limitation of these is that the resulting motion is restricted to one direction only. The behaviour is also affected by surface properties such as roughness. In this work, we make use of electrostatic adhesion (EA) to achieve anisotropy in friction. This approach is similar to that of [115].

Turning the adhesion on and off is easy with EA and it uses the same input (electrostatic potential difference) as the DEA. This means that both the movement and the traction can be provided using the same set-up. Since the friction can be controlled on demand and be introduced in any direction, it greatly expands the orientations in which the robot can move. EA also works on a variety of surfaces with different electrical properties which enables the robot to operate in multiple environments. Orientation of the surface is also not an issue since the force of attraction makes sure that the robot adheres to it. The prototype of the robot using the multi-sector disk DEA in combination with EA feet is shown in fig. C1.

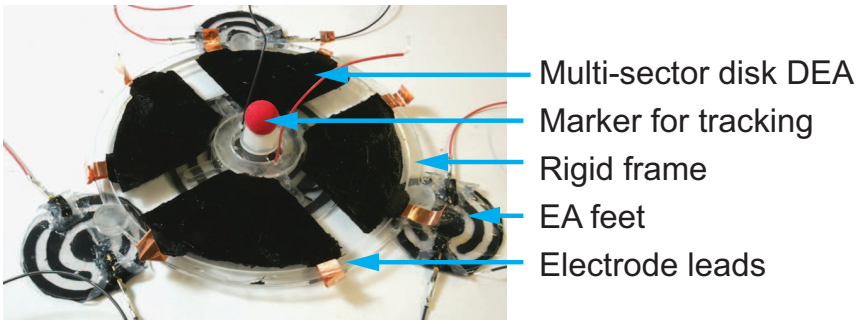

Figure C1: A prototype of the proposed crawling robot.

Figure C2: Actuation principle of the four sector disk DEA. Red regions are the actuated segments. The consequent movement of the rigid central disk is also shown. [118] © 2019 IEEE

Fabrication - Multi-sector Disk DEA

The multi-sector disk DEA consists of a membrane that is stretched between a small central disk and a larger ring shaped rigid frame. The membrane is free to move in the intervening space. This space is divided into multiple sectors each of which is actuated independently. When a potential difference is applied across the electrodes of one sector, the expansion in its area moves the central disk relative to the frame. By actuating different sectors, a two degree of freedom movement can be realised (fig. C2). This configuration of the DEA could be considered to be a planar implementation of [203], .

To fabricate the disk-shaped DEA, a single layer of elastomer (VHB 4905, 3M) was used. It was stretched equally in the two planar axes to 4 times its initial dimension. This pre-stretched membrane was then bonded to an acrylic ring of radius 50mm and a central disk of radius 15mm. The stretched membrane had a thickness of 31.25µm. The design used in this study divided the membrane region into four sectors, each taking up roughly a quarter of the space. Electrodes were painted on both sides of the membrane using carbon grease (MG Chemicals). Care was taken to ensure sufficient spacing between the electrodes to prevent an electrical short at the high actuation voltages. Each electrode pair actuates one of the four quadrants. To enable easy connection with cables supplying the actuation voltage, copper tape was affixed to the membrane (see fig. C1).

The DEA was characterised in terms of the maximum blocking force at different stroke lengths. The details of the experiments are presented in the appendix B. The DEA design presented here was able to exert a maximum force of 400mN at $E_0 = 100V/\mu m$ and a linear stroke of 4mm in the plane of actuation.

Fabrication - Electroadhesive Pads

A circular inter-digitated design of the electrodes was chosen for electroadhesive pads (fig. C3 as it produces force that is relatively symmetric in all planar directions as opposed to a rectangular pattern [204]. This symmetry is desirable when moving in multiple directions.

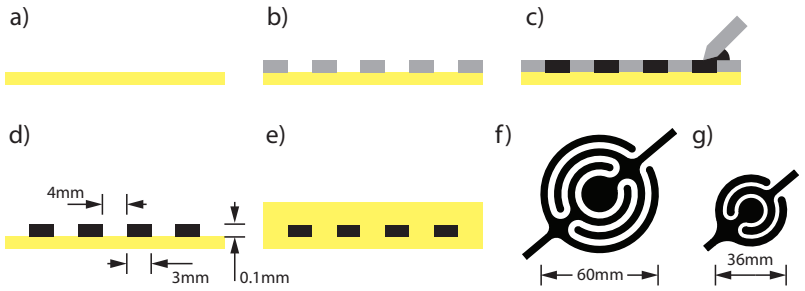

Figure C3: Stages of fabrication of electro-adhesive pad. (a) A thin layer of elastomer is spin coated on an acrylic surface. (b) A paper mask is laid on top of the first layer after it cures. (c) Conductive silicone is applied through the mask. (d) The mask is peeled off and the second layer is allowed to cure. (e) A final layer of elastomer is applied to enclose the electrodes. (f) The pattern used for the central foot. (g) The pattern used for the feet on the sides. [118] © 2019 IEEE

The EA pads were fabricated by casting layers of silicone (Ecoflex 00-30, Smooth-On). The process is similar to [205] but a mask is used to form the electrode region instead of engraved mould to enable quick changes in design. The order of constructing the layers is also reversed. First, a thin layer of silicone is deposited on an acrylic disk by spin coating at a speed of 50rpm for 10s followed by a speed of 1000rpm for 60s. The electrode layer, which is a mix of carbon black powder (Vulcan CXC72R, Cabot) and Ecoflex at a concentration of 5% by weight, is painted on top of this initial layer through the mask cut in the shape of the desired pattern. The electrode layer was left to cure. It was then encased in an insulating layer of silicone. Figure C3 shows the construction of the layers. A thin sheet of mylar (0.02mm) was affixed to the bottom of the pad to reduce tackiness of the surface. In total, four EA pads were fabricated. Three were affixed to the periphery of the disk and had a diameter of 36mm. One larger pad of diameter 60mm was fixed to the centre of the DEA membrane.

A cross section of the robot with its components is shown in fig. C4. The feet are adjusted in height such that the weight of the body is equally distributed between the central foot and the outer feet. A light-weight red ball was fixed to top surface of the membrane in the centre to aid in tracking the position of the robot. The entire robot weighs 20g.

The EA pads were characterised to determine their adhesion to surfaces of different materials. This was measured in terms of the shear force as a function of actuation voltage. A maximum shear force of 3N was observed on a wooden surface. The details of these

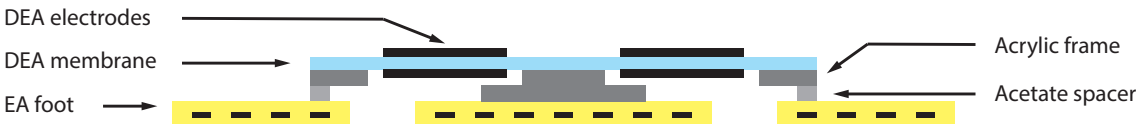

Figure C4: A sectional view of the robot showing its different parts. [118] © 2019 IEEE

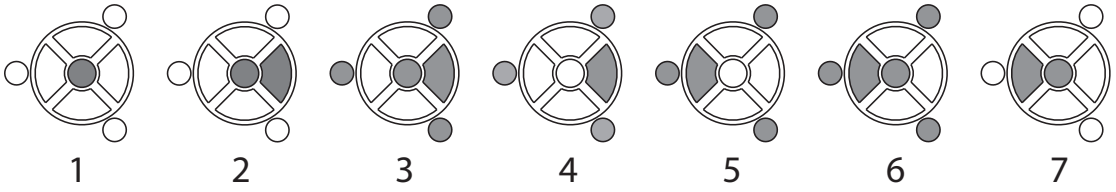

Figure C5: Stages of actuation of the robot. Shaded regions indicate the DEA sector and EA foot that is active in each stage. [118] © 2019 IEEE

experiments are presented in the appendix B.

Crawling Robot - Working Principle

To achieve walking motion, actuation is provided in a specific pattern. The different stages of actuation are shown in fig. 8. They can be described as follows.

- 1: Activate the central EA foot.
- 2: Actuate the front DEA in the direction of motion. The body moves forwards as the central foot is holding its position.
- 3: Activate the EA feet on the sides. Front DEA is still actuated.
- 4: Deactivate the central EA foot. Front DEA is still actuated. The body holds its displaced position.
- 5: Actuate the rear DEA in the direction of actuation. Front DEA is simultaneously discharged. As a result, the central foot moves forwards.
- 6: Activate the central EA foot. It now holds the displaced position. Rear DEA is still actuated.
- 7: Deactivate the EA feet on the sides. Rear DEA is still actuated.
- 8: Rear DEA is discharged. The body moves forwards slightly. One cycle is complete and the robot is back to stage 1.

To obtain the desired sequence of motion as described above, each actuator was controlled separately. The control structure is shown in fig. C6. Each DEA was independently energized and discharged by a pair of relays (Ki in fig. C6). These relays were opened and closed based on digital signals issued from a MATLAB script through an NI DAQ

(USB-6343). The high voltage required to activate the DEA was provided by means of an amplifier (EMCO F121). A bleeding resistor of 4M was used to safely discharge the DEA. In the case of the EA feet, two separate high voltage channels were used, one for the central foot and the other for the three feet combined. These channels were supplied from independent high voltage amplifiers (UltraVolt 5HVA23-BPI).

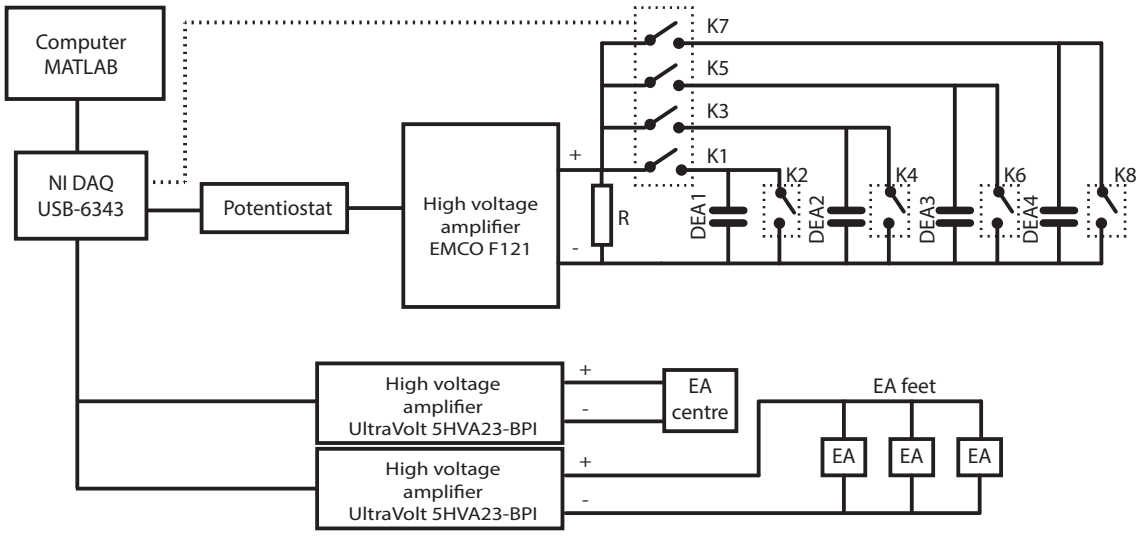

Figure C6: Schematic diagram of the controller of the robot. [118] © 2019 IEEE

A step function was used to charge and discharge each actuator. In case of the EA feet, it was found that a simple drop in applied voltage was not sufficient to make the pad release quickly from the surface it was in contact with. From practice, it was found that a decaying sinusoidal input enabled quicker release of the feet. This phenomenon of slow release has been studied and addressed in [206] where an integrated DEA is used to create an oscillation that forces the release.

Crawling Robot - Locomotion Experiments

Figure C7 shows a series of photographs of the robot as it takes five steps in one direction. The images were taken at the starting position, and after three and five cycles of movement. In this demonstration, one cycle 1.75s to complete. The voltage used for actuating DEA was 3.125kV, to activate the outer EA feet was 3kV each and for the central EA foot was 4kV. The motion of the robot in two directions is shown in fig. C8 where its position was tracked and analysed using a camera recording from above. In this arbitrary trajectory, the robot takes three consecutive steps in one direction (t0 to t3), followed by three steps in a perpendicular direction (t3 to t6). The change in direction is achieved by activating the pair of actuators that are in line with the desired motion. This shows that the robot can successfully move in two perpendicular directions. In theory, the robot can move in any direction on the plane through appropriate control of all four actuators.

The speed of the robot was controlled by changing the frequency of actuation. Figure

C9 shows a plot of the speed of the robot as a function of actuation frequency. There is a trade off between stroke length and frequency of actuation which affects the velocity of the robot. At lower frequencies, the actuators exhibit longer strokes but the robot moves slower because the stroke occurs fewer times in a given period of time. At higher frequencies the stride rate was found to increase until the response is saturated by viscoelastic damping, which is a well known characteristic of VHB 4905. The other issue with operating at higher frequencies was the slow release rate of the EA pads mentioned in the previous section. A maximum speed of 12mm/s was observed at an optimal frequency of 2.5Hz which equates to 0.1 body-lengths/s.

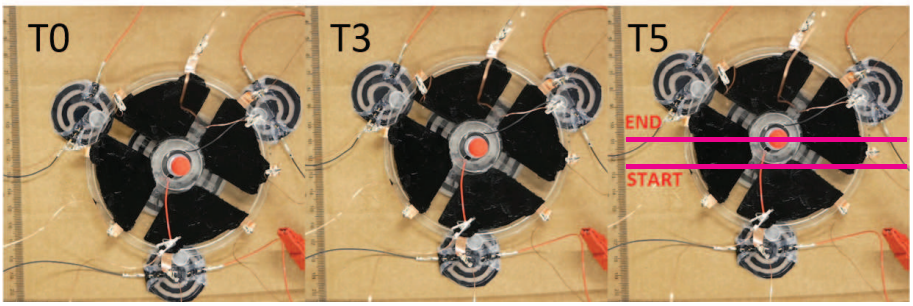

Figure C7: The robot in its starting position (T0), after three steps of movement (T3) and after five steps of movement (T5). Refer to accompanying video. [118] © 2019 IEEE

Modelling a Multi-sector Disk DEA

To quantify the blocking force and the stroke of the proposed model a simplified model was used along the lines of [208]. The design of the multi-sector disk shaped DEA is symmetric. It is therefore sufficient to look at the movement of one of the sectors. The model used here make three simplifying assumptions which are stated as follows.

- The circumferential deformation does not contribute to the stroke and force output.
- The circumferential stretch ratio is constant and is not affected by the actuation.
- The elastomer is incompressible.

The design is characterised by parameters defined using a circular coordinate system as depicted in fig. C10. Let $([r_{in},\ r_{out}], [-\theta_A,\ \theta_A])$ be the region of the actuated sector. r_{in} and r_{out} indicate the radial span of the actuator (i.e. the radius of the central disk and the radius of the outer ring respectively) and θ_A is the angular coordinate of the boundary of the active region. An electric field $E = V/T$ is applied across the electrodes of this section, where V is the applied voltage and T is the thickness of the membrane. Let $r_0 = r_{out} - r_{in}$ be the initial radius of the DEA. Under the assumption that the central disk moves by a distance d with respect to the outer ring, the radius at an arbitrary angle θ can be expressed as

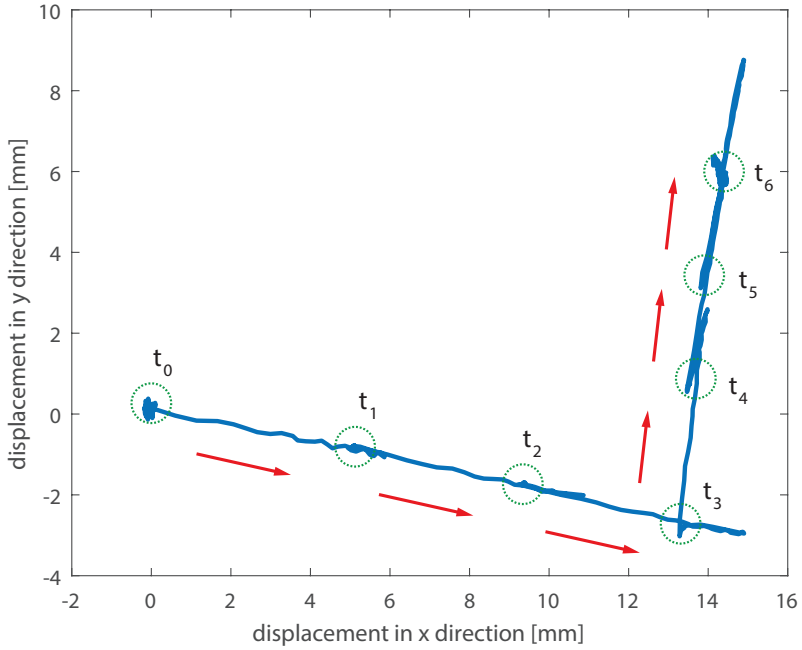

Figure C8: Position of the robot tracked using image processing. The robot takes three steps in one direction followed by three more steps in the perpendicular direction, demonstrating its two degrees of movement. [118] © 2019 IEEE

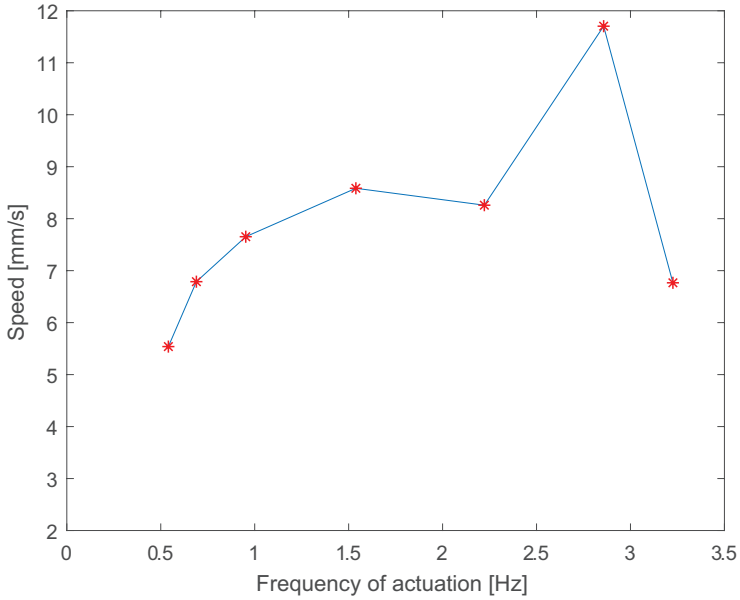

Figure C9: Speed of the robot at different actuation frequencies. Optimum speed of 12mm/s is reached at 2.5Hz. [118] © 2019 IEEE

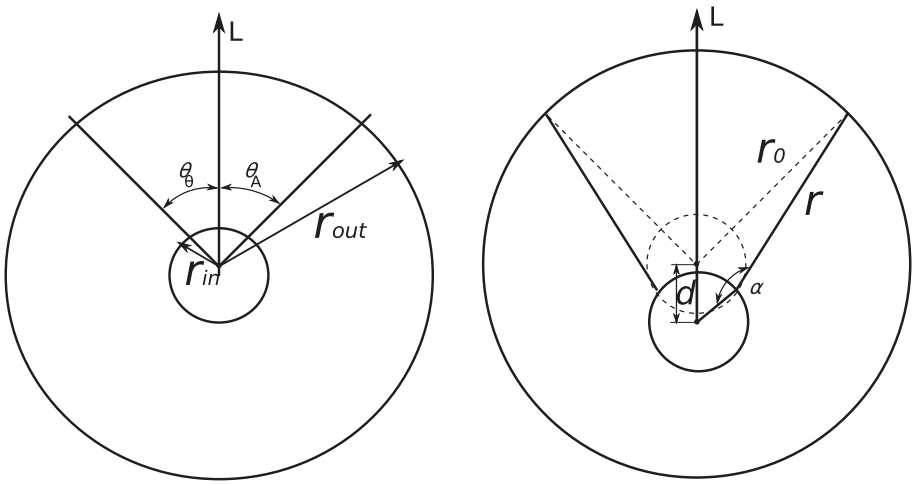

Figure C10: Illustration of the actuation principle in terms of circular coordinates. r_{in} is the radius of the inner rigid disk and r_{out} is the inner radius of the outer ring. d is the displacement of the central disk. (a) Un-actuated segment. (b) Actuated segment.

$$r(\theta) = \sqrt{r_0^2 + d^2 - 2r_0 d\cos(\pi - \theta)} \tag{7}$$

To characterise the radial stress in the material, the Gent nonlinear material model has been used [209]. It can be expressed as

$$\sigma_1 = \frac{\mu\left(\lambda_1^2 - \lambda_1^{-2}\lambda_2^{-2}\right)}{1 - \left(\lambda_1^2 + \lambda_2^2 + \lambda_1^{-2}\lambda_2^{-2} - 3\right)/J} - \epsilon_0\epsilon_r E^2 \tag{8}$$

where λ_1 is the radial stretch ratio, λ_2 is the circumferential stretch ratio, ϵ_0 and ϵ_r are the absolute and relative dielectric permittivity respectively, μ is the shear modulus and J is the material constant related to the limiting stretch. The values $\mu = 30$kPa and $J = 150$N/m2 have been found as best fits to the experimental data presented in the following section. These are in the range recommended in [210], [211] and [212].

To estimate the total force on the central disk due to actuation of one sector, the radial force due to an infinitesimal section (dF) at an angular coordinate θ can be integrated as follows

$$F = \int_{-\theta_A}^{\theta_A} dF(\theta, E = E_0)\cos(\alpha)\cos(\theta) + \int_{\theta_A}^{2\pi-\theta_A} dF(\theta, E = 0)\cos(\alpha)\cos(\theta) \tag{9}$$

where $dF(\theta, E) = \sigma_1(\theta, E)^\top r(\theta)\, d\theta$ and $\cos(\alpha) = \frac{r_0^2 + r^2 - d^2}{2rr_0}$

Experimental Measurement of DEA Blocking Force

An experiment was set-up to measure the blocking force for the DEA as a function of displacement, d. In other words, the aim is to measure the force required to stop the

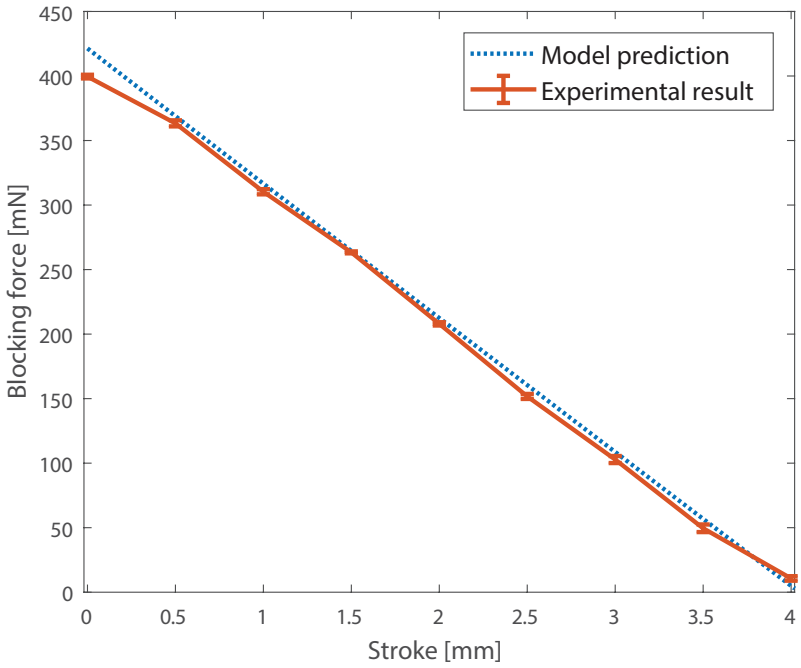

Figure C11: Blocking force of a single DEA at different stroke lengths.

central disk from moving. To do this, the frame of the DEA actuator was rigidly clamped to a test rig. A load cell was also fixed to the rig. The central disk was connected to the load cell by means of a string. As the disk moved, it pulled on the string, which recorded as a force on the load cell. Measurements were taken for strokes in the range of 0 to 4mm. Each set was repeated three times to avoid experimental error. All experiments were performed in a temperature controlled room maintained at 20°C.

Shown in fig. C11 is a comparison between the model and experimental results. The relationship between force and stroke is approximately linear. The DEA design in our study was able to exert a maximum force of 400mN at $E_0 = 100V/\mu m$ and a linear stroke of 4mm in the plane of actuation.

Shear Force due to EA

The force of attraction between two contacting surfaces in the presence of an electric field can be gives as [205]

$$F_N = \frac{1}{2}\epsilon_0\epsilon_r A\frac{V^2}{d^2}, \tag{10}$$

where A is the area of contact (of the EA pad) and V is the potential difference between the electrodes. This force acts normal to the surface. The critical shear force, F_S, defined as the peak force, acting along the surface, at which the pad separates from the surface it is adhering to, can be given in terms of the coefficient of friction between the surfaces of contact μ_f as

$$F_S = \mu_f F_N. \tag{11}$$

This suggests that the relation between applied voltage and the critical shear force is quadratic. However, in practice, several parameters have been determined to influence the magnitude of this force [213]. The problem of estimating this force is compounded if multiple electrode pairs are employed, such as the inter-digitated designs used in this work. Models to simulate and theoretically predict the force have been proposed but as reported in [214], there is inconsistency in the predictions. Therefore an experimental approach was followed in this work to determine the force.

The experiments were performed on an EA pad of diameter 60mm. The test substrates were made of cardboard, glass and finished wood. A lightweight nylon ring was affixed to the pad. It was then placed on the test substrate and connected to a load cell by means of a string. The load cell was mounted on a linear carriage that could be moved to pull the pad across the test surface.

First, the force of static friction was measured by sliding the pad on the test surface without it being activated. The peak force to initiate movement gives a measure of the static frictional force between the two surfaces. Then, the electric field between the electrodes was turned on to make the pad adhere to the surface. The pad was held stationary for 10s to eliminate dynamic effects of the electric field. The pad was then moved across the pad and the force required to move it was measured. By subtracting the force due to friction from this value, a measure of the shear force due to EA can be computed. Different actuation voltages were applied in the range of 2kV to 5kV and each trial was repeated 5 times. The critical shear force in each case is as shown in fig. C12.

It can be seen that there is a linear trend between the critical shear force and the activation voltage. This is similar to that presented in [115]. In the case where wood was used as the test surface, there was a larger variation in force between the trials. This could be due to to the non-uniformity in its composition as opposed to cardboard and glass which are more uniform. There are reports of higher shear resistance in the literature [215] which were obtained at higher activation voltages compared to the ones used in this study.

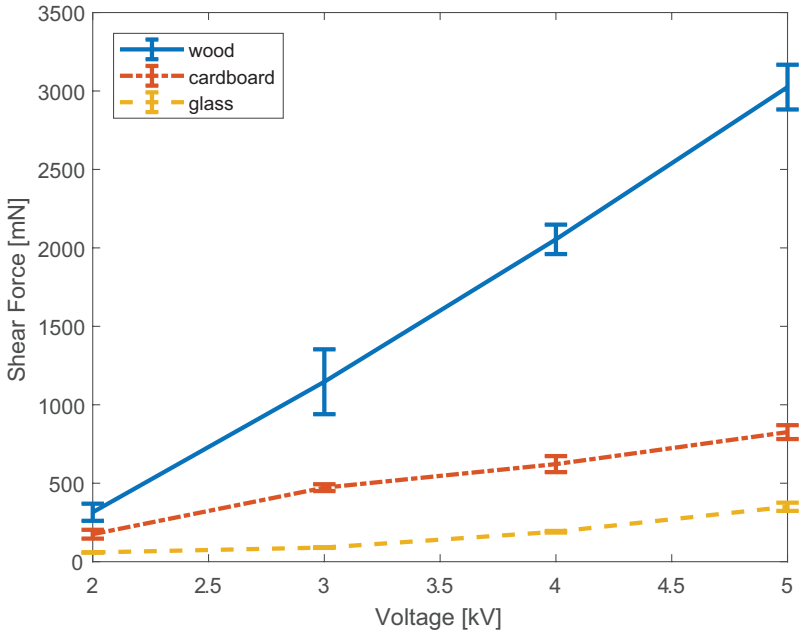

Figure C12: Shear force due to EA as a function of charging voltage on different surfaces. The EA pad has a circular geometry with an outer diameter of 60mm.